POLITECNICO
MILANO 1863

SCUOLA DI INGEGNERIA INDUSTRIALE
E DELL'INFORMAZIONE

# Comparison of different turbulence models for the numerical simulation of the flowfield around the DrivAer

Tesi di Laurea Magistrale in
Aeronautical Engineering -
Ingegneria Aeronautica

Author: **Giovanni Renda**

Student ID: 941713
Advisor: Prof. Paolo Schito
Co-advisors: Francesco Fabio Semeraro
Academic Year: 2021-2022

# Contents

# List of Figures

# List of Tables

# List of Abbreviations

| | |
|---|---|
| **AR** | **A**spect **R**atio |
| **DES** | **D**etached-**E**ddy **S**imulation |
| **DDES** | **D**elayed **D**etached-**E**ddy **S**imulation |
| **HPC** | **H**igh-**P**erformance **C**omputing |
| **IDDES** | **I**mproved **D**elayed **D**etached-**E**ddy **S**imulation |
| **ISCRA** | **I**talian **S**uper**C**omputing **R**esource **A**llocation |
| **KSKL** | **K** **S**quare-root-**K** **L** |
| **LES** | **L**arge-**E**ddy **S**imulation |
| **MSD** | **M**odeled-**S**tress **D**epletion |
| **RAS** | **R**eynolds **A**veraged **S**imulation |
| **RANS** | **R**eynolds **A**veraged **N**avier-**S**tokes |
| **TRRANS** | **T**urbulence-**R**esolving **R**eynolds **A**veraged **N**avier-**S**tokes |
| **URANS** | **U**nsteady **R**eynolds **A**veraged **N**avier-**S**tokes |
| **SA** | **S**palart-**A**llmaras |
| **SAS** | **S**cale-**A**daptive **S**imulation |
| **SST** | **S**hear-**S**tress **T**ransport |
| **WMLES** | **W**all-**M**odeled **L**arge-**E**ddy **S**imulation |

# List of Symbols

| Variable | Description | SI unit |
|---|---|---|
| $\widetilde{(.)}$ | Filtered part | [-] |
| $\bar{(.)}$ | Mean part | [-] |
| $(.)'$ | Fluctuating part | [-] |
| $a_1$ | $\kappa$-$\omega$ SST Model coefficient | [-] |
| $b_1$ | $\kappa$-$\omega$ SST Model coefficient | [-] |
| $C_\mu$ | Model coefficient | [-] |
| $\delta$ | Boundary Layer thickness | m |
| $\delta_{ij}$ | Kronecker delta | [-] |
| $d$ | Diameter | m |
| $\widetilde{d}_{DES}$ | DES length scale | m |
| $\widetilde{d}_{DDES}$ | DDES length scale | m |
| $D$ | Drag force | $\mathrm{kg\,m\,s^{-2}}$ |
| $\epsilon$ | Turbulent kinetic energy dissipation | $\mathrm{m^2\,s^{-3}}$ |
| $E$ | Total energy | $\mathrm{kg\,m^3\,s^{-1}}$ |
| $\phi$ | KSKL model variable | $\mathrm{m^2\,s^{-1}}$ |
| $f$ | Shedding frequency | $\mathrm{s^{-1}}$ |
| $f_{d1}$ | DDES delay shielding function | [-] |
| $f_{d2}$ | IDDES delay shielding function | [-] |
| $f_{v1}$ | SA model coefficient | [-] |
| $F_2$ | $\kappa$-$\omega$ SST Blending function | [-] |
| $i$ | Turbulence intensity | [-] |
| $\kappa$ | Turbulent kinetic energy | $\mathrm{m^2\,s^{-2}}$ |
| $l$ | Turbulent length scale | m |
| $\widetilde{L}$ | Reference length scale | m |
| $L$ | Integral length scale of turbulence | m |
| $L_m$ | Characteristic length scale of the mean flow | m |
| $Ma$ | Mach number | [-] |
| $\nu$ | Molecular viscosity | $\mathrm{m^2\,s^{-1}}$ |
| $\widetilde{\nu}$ | Modified fluid viscosity | $\mathrm{m^2\,s^{-1}}$ |
| $\nu_t$ | kinematic eddy viscosity | $\mathrm{m^2\,s^{-1}}$ |

| Variable | Description | SI unit |
|---|---|---|
| $\omega$ | Turbulent specific dissipation rate | $\mathrm{s}^{-1}$ |
| $p$ | Static pressure | Pa |
| $R$ | Reynolds stress tensor | [-] |
| $S_{ij}$ | Shear rate | $\mathrm{s}^{-1}$ |
| $t$ | Thickness | m |
| $\tau_{ij}$ | Viscous stresses | $\mathrm{kg\,s}^{-1}$ |
| $T$ | Temperature | K |
| $u$ | Velocity along the x-direction | $\mathrm{m\,s}^{-1}$ |
| $u_{ref}$ | Reference velocity | $\mathrm{m\,s}^{-1}$ |
| $v$ | Velocity along the y-direction | $\mathrm{m\,s}^{-1}$ |
| $w$ | Velocity along the z-direction | $\mathrm{m\,s}^{-1}$ |
| $y$ | Wall distance | m |

# Abstract

The DrivAer is a popular model used for aerodynamic research in the automotive field. Since 2012 the geometry has become a benchmark for wind tunnel testing and numerical simulations and during the last years has been updated by means of new components such as engine bay, suspensions, detailed underbody. This study aims to give a scientific approach for choosing the most appropriate turbulence model to simulate the flow around DrivAer. The choice of the turbulence model is dependent on various aspects such as the problem, the geometry, as well as the type of mesh.
The comparisons are performed not only among RANS codes, but also with modern hybrid RANS-LES, to highlight strong and weak points of each model and method. A preliminary analysis is performed for the flow around the cylinder to identify a smaller subset of models by running a smoother test case. In some cases it has been noticed that the $\kappa - \omega$ SST model is more sensitive to the initial conditions and mesh settings with respect to Spalart–Allmaras model, this leads to differences in the pressure distributions as well. The most suitable subset of models is used to simulate the flow around the vehicle. During this second part of the work, interesting insights of the flow-fields are presented along with a grid convergence of the results. Differences in predicting the flow separation between DDES and IDDES model are shown, but also on the aerodynamics forces, particularly the lift contribution resulted to be a quantity more sensitive to changes of turbulence models and simulation settings. Finally, a sensitivity analysis to the Courant number is performed. This is done by changing the time step and analyzing the influence on the numerical stability and on the aerodynamics forces, leading to lower down the overall computational cost of the simulations.

**Keywords:** DrivAer, turbulence modeling, aerodynamics, Courant number.

# Abstract in lingua italiana

Il DrivAer è un modello popolare utilizzato per la ricerca aerodinamica in ambito automobilistico. Dal 2012 la geometria è diventata un punto di riferimento per i test in galleria del vento e le simulazioni numeriche e negli ultimi anni è stata aggiornata con l'aggiunta di nuove componenti tra cui il vano motore, le sospensioni, il sottoscocca dettagliato. Questo studio mira a fornire un approccio scientifico per la scelta del modello di turbolenza più appropriato per simulare il flusso attorno al DrivAer. La scelta del modello di turbolenza dipende da vari aspetti tra cui il problema, la geometria e il tipo di mesh.
I confronti sono stati eseguiti non solo tra codici RANS, ma che con moderni codici ibridi RANS-LES, per evidenziare punti di forza e di debolezza di ciascun modello e metodo. Inizialmente è stata eseguita un'analisi preliminare per il flusso attorno al cilindro al fine di identificare un sottoinsieme più ristretto di modelli simulando un test case più fluido. In alcuni casi è stato notato che il modello $\kappa - \omega$ SST risulta più sensibile alle condizioni iniziali e alle impostazioni della mesh rispetto al modello Spalart–Allmaras, questo porta anche a differenze nelle distribuzioni di pressione. Il sottoinsieme di modelli più adeguato è stato quindi utilizzato per simulare il flusso intorno al veicolo. Durante questa seconda parte del lavoro, vengono presentati interessanti approfondimenti sui campi di flusso accompagnati da una convergenza di griglia dei risultati. Vengono mostrate differenze nel predirre la separazione del flusso tra i modelli DDES e IDDES, ma anche differenze sulle forze aerodinamiche, in particolare il contributo della portanza è risultato essere più sensibile ai cambiamenti dei modelli di turbolenza e alle impostazioni della simulazione. Infine, è stata eseguita un'analisi di sensitività al numero Courant. Questo è stato fatto modificando il passo temporale e analizzando l'influenza sulla stabilità numerica e sulle forze aerodinamiche, portando ad abbassare il costo computazionale complessivo delle simulazioni.

**Parole chiave:** DrivAer, modellazione della turbolenza, aerodinamica, numero di Courant.

# 1 | Introduction

## 1.1. The role of Aerodynamics in the automotive field

The aerodynamics is the study of motion of air acting on a generic body. In the context of the automotive industry, aerodynamics affects directly the car's performances, so the top speed, fuel economy, noise reduction, drivability, passenger's comfort.

From the interaction between air and vehicle's surfaces, forces are generated and they have to be maximized or minimized depending on the type of the vehicle. For the case of a car, the lift has to be maximized downwards, in this sense it is called also *downforce*, to improve the car stability and the wheel grip that is needed for any type of maneuver, weather conditions and other situations in which a vehicle might be in during its working life. The drag has to be kept as low as possible to improve the top speed and reduce the emissions.

Aerodynamics allows also to study the cooling systems related to the internal components such as engine, gears and brakes, and finally it allows to study the flow development inside the car itself, so eventually ventilating and air conditioning systems and their interactions with the passengers.

In general depending on the type of road vehicle and its associated shape, the flowfield changes and so the forces do, but three different categories of flows can be identified [1]:

1. The flow around the vehicle surfaces
2. The flow through the vehicle's body
3. The flow processes within the vehicle's machinery

Aerodynamics is just applied on the first two items, since it studies the forces generated on the vehicle by the interactions between flow and surfaces, whilst the third item is more related to the fluid dynamics through specific internal systems.

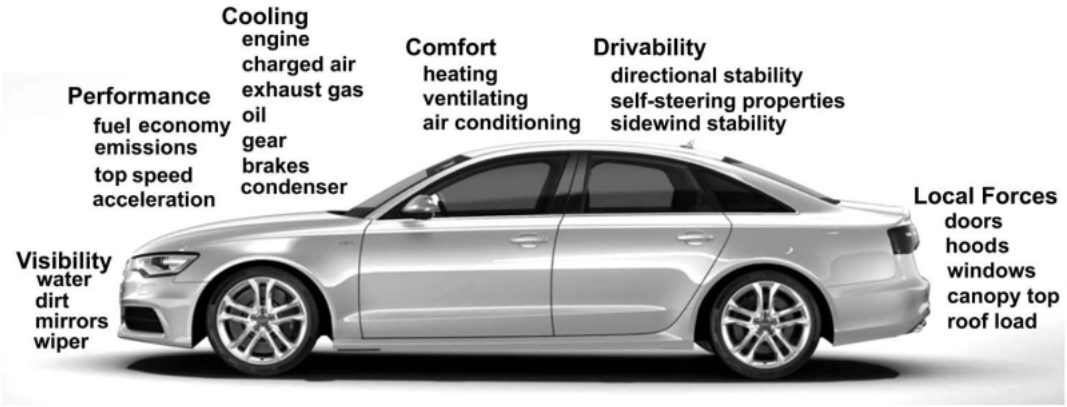


Figure 1.1: Aerodynamics applications for a car[1]

Specifically this study treats the flow around the DrivAer and the main matter involves the external flow on the entire body. This allows to focus more on differences among turbulence models on a large scale, but also some interesting considerations are made for smaller and important feature such as the mirrors and tyres.

However in the automotive field, the performances are also dependent on the companies aesthetic principles which could already introduce some limitations at the early stages of design. The role of the aerodynamics intended both in terms of wind tunnel testing and numerical applications, is then crucial for improving the vehicle's performance and match the market and company needs.

## 1.2. The state of art of the DrivAer's tests

Although the DrivAer has becomes widely used for research purpose, the reliability of wind tunnel test data remains still limited, particularly for full-scale experiments.

To elevate the fidelity of these tests, Ford carried out a campaign of experiments on a more advanced geometry inside the Pininfarina Wind Tunnel for which a comprehensive summary is given by the paper of Hupertz et al.[2]. Since 2017 the vehicle has been updated with a simplified engine bay which includes a cooling package and a powertrain with an attached exhaust system. This new car geometry allowed to highlight differences between the open and closed cooling configurations. Three different DrivAer configurations are available, namely the notchback, the fastback and the estate, but for the case in point the notchback one has been considered since results are presented for such configuration in this paper. The Pirinfarina Wind Tunnel consists of an open jet test section with an $11m^2$ nozzle. This facility is equipped by suction systems that allows to reduce the boundary layer generation, but also tangential blowing system to make the flow as uniform as possible during the working condition.

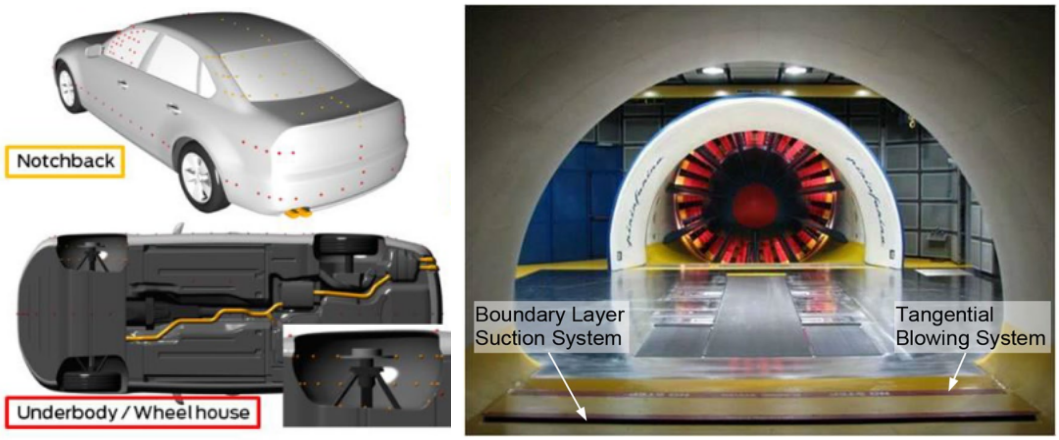


Figure 1.2: Detailed Notchback DrivAer(on the left) and Wind tunnel boundary layer control(on the right)[2]

The experiments have been performed at a Reynolds number of $11 \cdot 10^6$ and the measurements were taken by means of 295 pressure probes placed on the entire vehicle as shown in the Figure 1.2. Some others probes were placed in the car's and wheel's wakes with the aim of measuring flowfield distribution on entire planes. The results are thus presented by means of pressure distributions along the car and its underbody, but also aerodynamic coefficients, pressure and normalized velocity flowfields.

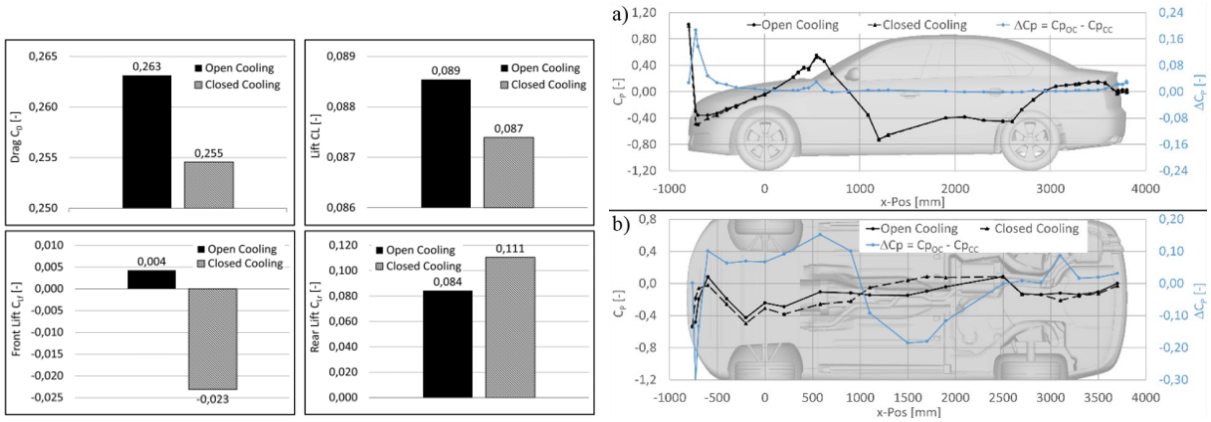


Figure 1.3: Surface and underbody pressure distributions(on the left) and aerodynamics forces(on the right) for the open and closed cooling configurations[2]

Closing the front grill results in a reduction of the aerodynamic drag of $\Delta C_D = 0.008$, whilst the overall effect on the lift contribution is marginal, since the difference on the front and rear of the vehicle is the same $\Delta C_{Lf} = \Delta C_{Lr} = 0.027$.
For what concerns the pressure difference, this is defined as the difference between the open and closed cooling cases and it is represented in Figure 1.3 with the blue line. The open cooling results in local pressure differences at the the leading edge of the hood and in the center part of the vehicle, even if smaller. On the underbody, the pressure distributions change in a more evident way at the leading-edge: the pressure is lower for the open cooling conditions due to the increase of momentum of the airflow underneath the vehicle, leading to lower down the pressure for the closed cooling case; at the rear of the DrivAer, the pressure differences becomes smaller.

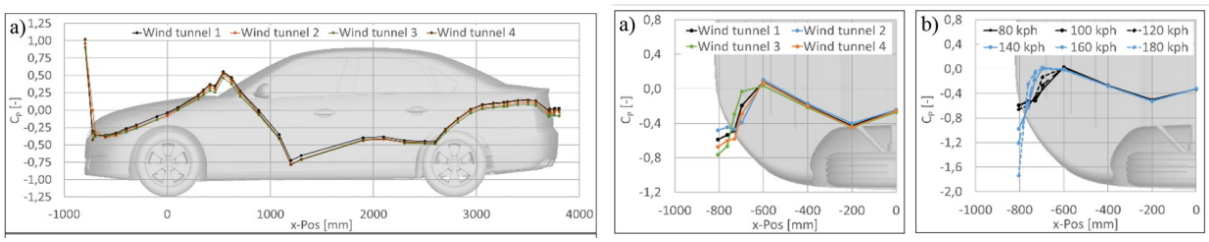


Figure 1.4: Surface pressure distributions in four wind tunnels(on the left) and at different velocities(on the right)[2]

The tests have been carried out in four different wind tunnel to test also the repeatability of the same experiments. As it can be noticed in Figure 1.4, the pressure difference at the center line location are smaller along the whole car, they are just more evident at the leading edge which resulted to be more sensitive to the experiments and also changes in the velocities. For the considerations made so far, this paper[2] represents one of the most

recent and relevant reference to be used for CFD correlation due to the high level of data reliability.

For what concerns the CFD side, during the last years new turbulence models are coming out with the aim of approximating better the flow behaviour. It has been proved that RANS cannot predict correctly the the flowfield for all the car configurations, since they underpredict the turbulence levels in the initial separated shear layer, leading to an over-prediction of the recirculation size. The hybrid RANS-LES methods(DES) resolve this problem with flowfields and aerodynamics forces more in agreement with experiments. In line with this, Hupertz and other 65 participants [3] shared their data coming from different CFD solvers, meshes and turbulence models. Comparing these results among each other, Hupertz was able to identify areas of *test variability* in which the results should be.

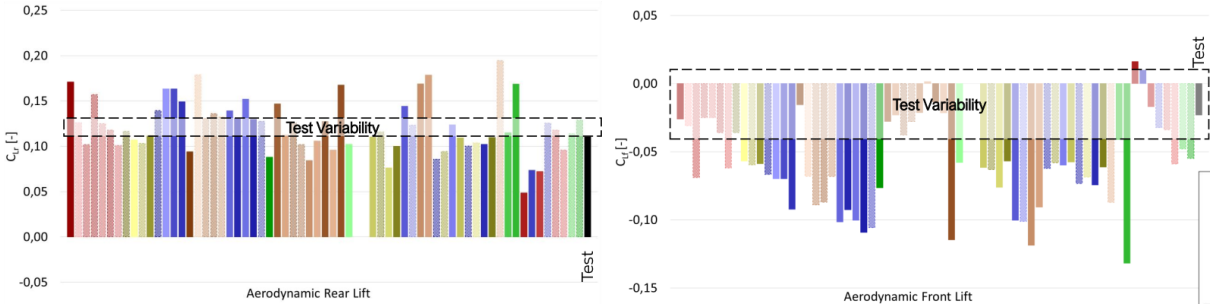


Figure 1.5: Front, Rear lift coefficients and test variability region [3]

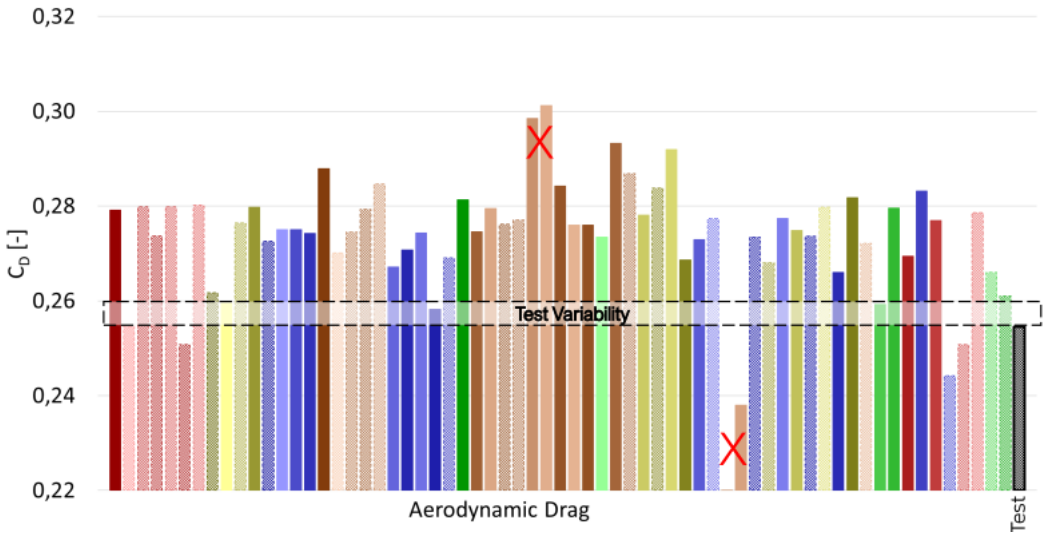


Figure 1.6: Drag coefficients and test variability region [3]

The red crosses in the Figures 1.5 and 1.6 are out of the average results either due to an

under- or over- estimation. For what concerns the aerodynamic lift, it is underestimated at the front of the vehicle, this can be due to the large errors inside the wheelhouse downstream the front wheel; whilst the overall drag coefficients result in overprediction, but closer to the experiments.

Taking advantage of the modern turbulence model, namely DDES and IDDES, Neil Ashton et al. in the paper[4] propose the numerical simulations around the DrivAer along with a grid convergence of the results. They simulated a different car condition with respect to Hupertz et al.[3], particularly the open-road configuration which is a real working condition, for instance a car proceeding at constant speed in a highway.

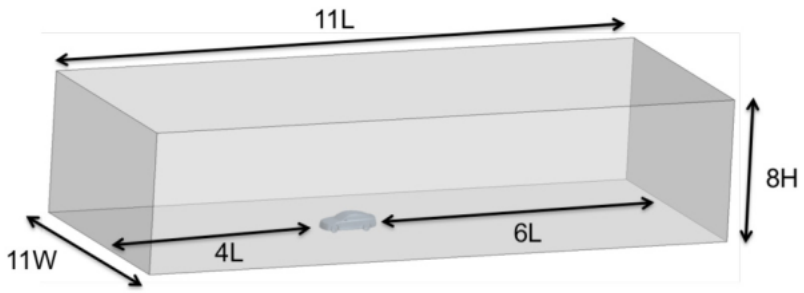


Figure 1.7: Computational domain used by Neil Ashton et al.[4]

The computational domain has been scaled with respect to the DrivAer geometry as shown in Figure 1.7, and the Reynolds number has been set to $4.87 \cdot 10^6$. The wheels are non-rotating and the underbody is smooth. Already with this simplified geometry, the number of cells is of $300 \cdot 10^6$ to create a fine mesh with $y^+ < 1$.

| Model | Estate | Fastback | Percentage Difference |
|---|---|---|---|
| Exp. | 0.296 | 0.254 | |
| Spalart Allmaras | 0.280 **(-5.4%)** | 0.260 **(+2.3%)** | 4.3% |
| Realizable $k$-$\varepsilon$ | 0.260 **(+12.1%)** | 0.244 **(-3.9%)** | 8.0% |
| $k$-$\omega$ SST | 0.275 **(+7.1%)** | 0.260 **(+2.3%)** | 4.7% |
| $k$-$\varepsilon$ B-EVM | 0.253 **(+14.5%)** | 0.2435 **(-4.1%)** | 5.2% |
| EB-RSM | 0.256 **(+14.5%)** | 0.2482 **(-2.3%)** | 8.4% |

| Model | Estate | Fastback | Error |
|---|---|---|---|
| Exp. | 0.296 | 0.254 | |
| SST IDDES (coarse-poly) | 0.310 **(+4.7%)** | 0.268 **(+5.5%)** | 5.1% |
| SST IDDES (medium) | 0.307 **(+3.7%)** | 0.2615 **(+3.0%)** | 3.3% |
| SST IDDES (fine) | 0.306 **(+3.0%)** | 0.259 **(+1.6%)** | 2.3% |
| SA IDDES (medium) | 0.313 **(+5.7%)** | n/a | 5.7% |
| SA-DDES (medium) | 0.3072 **(+3.8%)** | n/a | 3.8% |

Figure 1.8: Mean drag coefficients for different turbulence models and car configurations[4]

According to the literature, RANS simulations results to have larger errors with respect to the DES simulation also for the same turbulence models, however the mean drag coefficient could just give a informations about the overall forces acting on the car.
For this reason, the analysis is enriched with pressure distributions, visualizations and grid sensitivity.

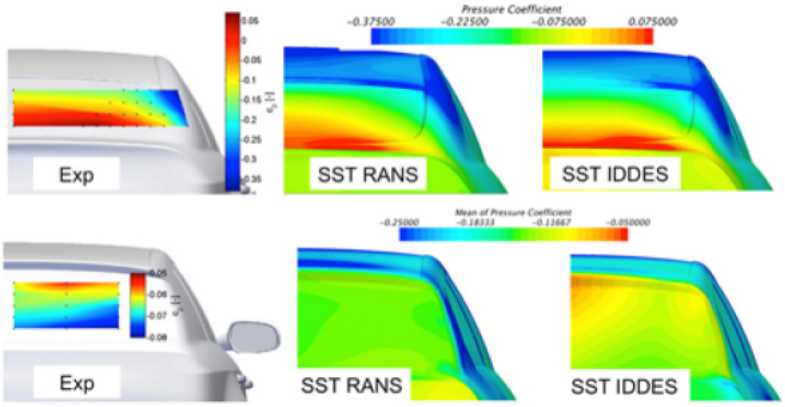


Figure 1.9: Mean Pressure Coefficient distributions for the Fastback (top) and Estate (bottom) vehicles[4]

In Figure 1.8 it is possible to notice that the recirculation area on the back of the vehicle is overpredicted by RANS, particularly for the estate configuration. This relies on the underprediction of the level of turbulent kinetic energy in the initial separated shear layer. The mesh results not to be feasible for the application of this work since there are some limitations of the computational power, however the size of the computational domain has been considered for simulating the open-road configuration.

## 1.3. About this study aims

The goal is to characterize the flow around the DrivAer by choosing the most appropriate turbulence models for this case.

What is missing in the literature is a systematic approach to a problem, but with a modern view: this study wants to give a scientific and, at the same time, general approach for fluid problems, all this is integrated with different and modern turbulence models that are compared among each other. In this sense, this study aims not to gave anything by chance.
First a large amount of turbulence models is identified and they are tested on a smoother test case, namely the flow around a cylinder. At least the same order of magnitude of the Reynolds number with respect to the DrivAer case($10^6$) is kept. The results are compared both in terms of dimensionless pressure coefficient distributions and overall aerodynamics coefficients. Further interesting visualizations are presented to identify the regions where LES and RAS modes are activated.
This step is necessary for several reasons: first it is useful to start always with a simpler geometry to understand how these models predict the flow and how they behave, then to test the settings that are used for the next investigations. Doing so, it is possible to identify a limited subset of turbulence models.
Once the most suitable models are found, they are applied for the numerical simulations of the DrivAer. The size of the computational domain is larger than that used for the cylinder: refinement regions are generated to cover zones where relevant turbulent phenomena occur such as the contact patch and the car's wake. Once the mesh passed all the checks, the turbulence models are tested. The validation is performed by means of aerodynamics coefficients and flowfield distributions: potential differences are highlighted both in terms of pressure and velocity, as well as with visualizations.
Finally, given the limited amount of computational power, it resulted interesting to perform a sensitivity analysis on the Courant Number to find a more convenient time step for this specific test case. This allowed to save computational power and time, by keeping a high reliability of the results. A similar work has been carried out by Ekman[5], but for different turbulence models and time steps, so it is different from what is present in literature so far.

# 2 | Aerodynamics and modeling

## 2.1. The flowfield around a car

Most of the upgrades that have been made over the years are related to the concept of the pillar. The pillar is typically an oblique or vertical support of the car's windows and the angles involved affect a lot the overall flow behaviour. The most important and studied are the $A$- and $C$- pillars which are qualitatively shown in the Figure 2.1.

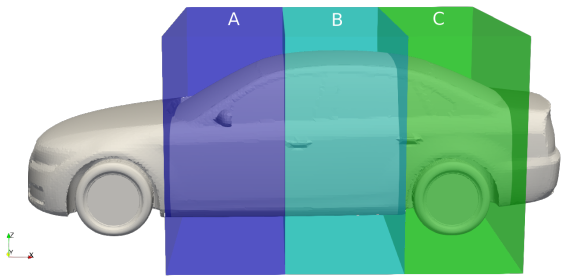


Figure 2.1: Qualitative car's pillars

Depending on the rear ends different type of vehicles (and so of flows) are identified:

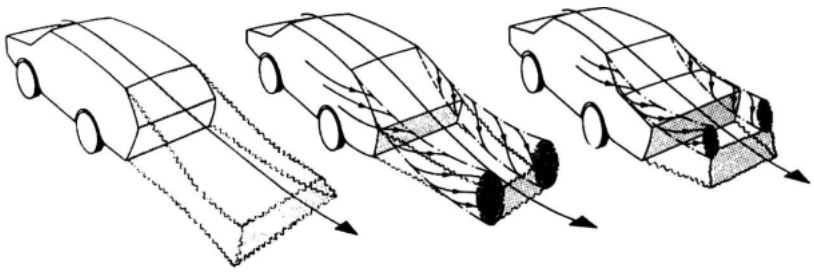

Figure 2.2: Schematic flow around a car: hatchback(on the left), fastback(in the middle), and notchback(on the right)[1]

It can be noticed that a pair of vortices (*horseshoe* vortex) are detached from the *C*- pillar and their magnitude is strictly related to the *slant angle* which is the slope of the C-pillar. In the case of a fastback car, increasing the slant angle induces more drag up to around 30° where the vortices disappear leading to a drop in the drag. The flowfield of a notch-back car is way more complex of a fastback car: the gap between the rear lights and the C-pillar induces lower recirculating vortices and these vortices, in turn, have less ability to pull down the flow on the back, leading to a larger wake with respect to the fastback configuration. This second model is chosen for all the simulations to detect eventually differences both in the wake and in the vicinity of the wheels.

Another important feature to put some emphasis on is the wheel which is responsible of about 25% of the total drag of a car. It is then worth to highlight briefly the steps that have been made during the last years.

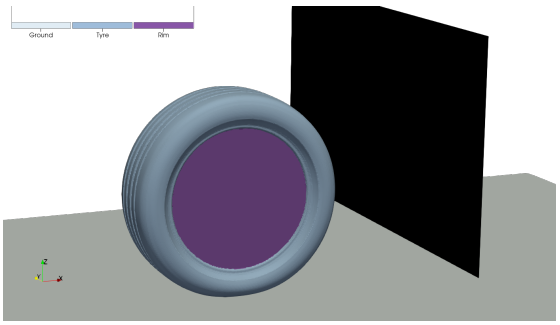


Figure 2.3: Wheel setup in blocks

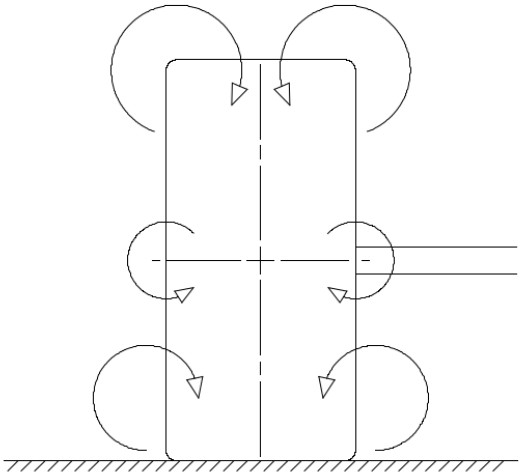

Figure 2.4: Simplified model[6]

Cogotti [7] and then Merker and Berneburg [8] presented a first simplified model[6] of the wheel seen as a streamlined body. The black plane in Figure 2.3 is representative of the view of the flow downstream the wheel for which a streamlined representation is given by Figure 2.4. The wheel is composed by non-deformable[1] tyre which is kept in position by a sting that, in turn, is parallel to the inlet flow and coincident with the rotational axis without introducing any additional forces. Three pairs of counter-rotating vortices are

[1]The deformed tyre is not axial-symmetric about its rotational. For instance in formula one cars the suspension affects the axis of wheel rotation of an angle with respect to the horizontal axis, so just sweeping the tyre profile about its rotational axis would generate a tyre that is not accurate over the conic direction.

identified: from the top to the bottom, they are respectively called *upper*, *hub* and *jetting* vortices. The most significant from an aerodynamic point of view are the last ones: in fact, the jetting vortices are strong vortices generated at the interface between wheel and ground(this is also called *contact patch*) and they are due to the strong viscous effects present there, therefore they are mostly responsible of drag, at least for such wheel configuration. The other two pairs are still trailing vortices, specifically the upper vortices are conventional vortices associated with the lifting of the body, whilst the hub vortices are generated by a combined effect of the wheel rotation and the incoming main flow. Some experimental investigation performed by Merker [8] were not able to find all of them: in fact, the left hub vortex has not been captured, this could be due to discrepancies between the wheel set ups which could have increased the vorticity of the right hub vortex and the jetting ones, suppressing the external one at the hub level. Furthermore the net downwash experienced in the wake due to the lifting of the wheel is not so evident, this could be still due to the entrainment of the flow in the wheel hub.

Although these results have been focused on a 2D analysis, a more general (3D) theory is needed to provide more informations about the flowfield, furthermore by putting the wheel inside the wheelhouse the flow structures change completely. To this end, Perry and Hornung [9] proposed the *Vortex Skeleton Method*: this theory exploits some visualization techniques, in order to detect the main low pressure regions affecting the wheel. This method shows a more detailed development of the flowfield than a standard streamlines plot. Although it is an approximated method, it works well for different car configuration by giving some insights of the flow separation. The vortex tubes are plotted along with the arrows which specify the directions of the rotation of the recirculating zones.

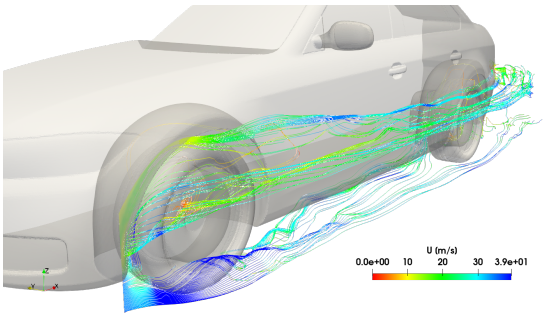


Figure 2.5: Streamlines around the wheel

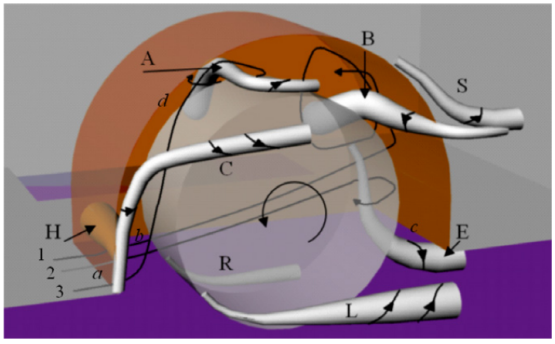


Figure 2.6: Vortex Skeleton theory[9]

In Figure 2.5 the streamlines give just information about the position of the vortex itself, whilst the vortex tube, in Figure 2.6, shows a much clear picture of its size and genesis. It

is interesting to describe better some of those structures since they have a strong impact on the whole flowfield in the wheelhouse:

- Vortex A is one of the greater structure and it is due to the unbalance of pressure distribution between the low and side regions of the wheel. This structures tends to be larger as the flow entering in the wheelhouse increases;
- Vortex B is due to deflection of the flow upwards after entering in Section 1 (Figure 2.6), in fact in absence of wheel axis, a recirculating area is created downstream and with the same sense of rotations of the wheel. This vortex could not be present for all the car geometries, since it could be both affected by both the geometry of the suspension and the vortex A;
- Vortex H is representative of the flow separation just after the leading edge and its sense of rotation coincides with the ones of the wheel. Its size increases with the gap between the wheel and the wheel arch [10];
- Vortex E is generated by the the interaction of the separated flow at the leading edge and the underbody flow: this vortex tube is obtained by the stretching of the separating bubble both downwards and towards the wake.

The vortices H and E are the most significant dynamic flow structures along with C, L, R and E; specifically the vortex E could be independent from the car configuration.

## 2.2. Governing equations

Understanding the flow behaviour around objects is the main subject of study of Aerodynamics which it takes advantage of the time dependent Navier-Stokes equations to compute pressure, skin-friction distributions and so aerodynamics loads. The classical and more general formulation of the Navier-Stokes equations is a non-closed system, but it can be rather simplified by assuming a Newtonian fluid for which the viscous stresses are linearly proportional to the local strain rate. Examples of fluids that behave as Newtonian ones can be either air or water. These two are already enough for this work and in general for most of the fluid dynamic applications in real life.
The systems of equations is thus:

$$\frac{\partial \rho}{\partial t} + \rho \frac{\partial u_i}{\partial x_j} = 0 \tag{2.1}$$

$$\rho \left( \frac{\partial u_i}{\partial t} + \frac{\partial u_i u_j}{\partial x_j} \right) = -\frac{\partial p}{\partial x_j} + \frac{\partial}{\partial x_j} \left( \mu \left( \frac{\partial u_i}{\partial x_j} + \frac{\partial u_j}{\partial x_i} \right) - \frac{2}{3} \mu \frac{\partial u_k}{\partial x_k} \delta_{ij} \right) + \rho f_b \tag{2.2}$$

$$\rho \left( \frac{\partial E}{\partial t} + \frac{\partial u_j E}{\partial x_j} \right) = -\frac{\partial p u_i}{\partial x_j} + \frac{\partial u_i \tau_{ij}}{\partial x_j} + \frac{\partial}{\partial x_j} \left( \kappa \frac{T}{x_j} \right) + P_E \tag{2.3}$$

where $u$ and $p$ are respectively the velocity and pressure fields, $f_b$ is the vector of the body forces, whilst $\tau_{ij} = \mu \left( \frac{\partial u_i}{\partial x_j} + \frac{\partial u_j}{\partial x_i} \right) - \frac{2}{3} \mu \frac{u_k}{x_k}$ according to the Newtonian fluid's assumption. These are five differential equations, namely one continuity equation (2.1), three momentum equations for each spatial direction (2.2) and finally one energy equation (2.3), whilst there are six unknowns which are density(1), pressure(1), temperature(1) and velocity(3). The system of equations become closed by adding the equation of state $p = p(\rho, T)$ which it relates pressure, density and temperature, therefore a solution might be achieved.
All the simulations are performed at relatively low velocities ($Ma < 0.3$) such that the compressible effects can be neglected ($\rho = constant$) and the equation are then further simplified, since there is not dependence from the derivatives of the density.

### 2.2.1. Subset of suitable equations

Eight different turbulence models implemented in OpenFOAM are tested:

- RANS family: $\text{RAS}_{SA}$, $\text{RAS}_{\kappa-\omega}$ SST, $\text{RAS}_{R\kappa-\epsilon}$;
- URANS family: $\text{SAS}_{\kappa-\omega SST}$;
- DES family: $\text{DDES}_{SA}$, $\text{DDES}_{\kappa-\omega SST}$; $\text{IDDES}_{SA}$, $\text{IDDES}_{\kappa-\omega SST}$.

Each turbulence model differently approximate the flow basing on the equation that are solved and a non-exhaustive description of the cited families is given in order to highlight the main characteristics.

### 2.2.2. RANS

This section wants to give a quick overview of the steps to be followed in order to achieve the URANS formulation; RANS are just URANS without the unsteady contribution. Starting from the Navier-Stokes equation in vectorial form:

$$\frac{\partial \rho}{\partial t} + \nabla \cdot (\rho \mathbf{u}) = \mathbf{0} \tag{2.4}$$

$$\rho \frac{\partial \mathbf{u}}{\partial t} + \rho \mathbf{u} \nabla \mathbf{u} = -\nabla p + \lambda \nabla (\nabla \cdot \mathbf{u}) + \mu [\nabla^2 \mathbf{u} + \nabla (\nabla \cdot \mathbf{u})^T] + \rho \mathbf{F}_b \tag{2.5}$$

For the case of incompressible flow:

$$\nabla \cdot \mathbf{u} = 0 \tag{2.6}$$

and for mono-atomic gas, the Stokes' relation is valid:

$$\lambda = -\frac{2}{3}\mu \tag{2.7}$$

By normalizing with respect to the density, the normalized incompressible Navier-Stokes equations are obtained:

$$\nabla \cdot \mathbf{u} = \mathbf{0} \tag{2.8}$$

$$\frac{\partial \mathbf{u}}{\partial t} + \mathbf{u} \nabla \mathbf{u} = -\frac{1}{\rho} \nabla p + \nu \nabla^2 \mathbf{u} + \mathbf{F}_b \tag{2.9}$$

At this stage, the so-called Reynolds decomposition is introduced both for the velocity and pressure:

$$u(x,t) = \overline{u}(x,t) + u'(x,t)$$

$$v(x,t) = \overline{v}(x,t) + v'(x,t)$$

$$w(x,t) = \overline{w}(x,t) + w'(x,t)$$

$$p(x,t) = \overline{p}(x,t) + p'(x,t)$$

This operation decomposes a vector field respectively into its mean and fluctuating parts, where by definition:

$$\overline{\mathbf{u}}(x,t) = \frac{1}{T}\int_{-\frac{T}{2}}^{\frac{T}{2}} \mathbf{u}(x,t)\,dt$$

$$\overline{\mathbf{u}}'(x,t) = 0$$

therefore the URANS equations are obtained:

$$\nabla \cdot \overline{\mathbf{u}} = \mathbf{0} \tag{2.10}$$

$$\frac{\partial \overline{\mathbf{u}}}{\partial t} + \nabla \cdot (\overline{\mathbf{u}} \cdot \overline{\mathbf{u}}) + \nabla \cdot (\overline{\mathbf{u}'\mathbf{u}'}) = -\frac{1}{\rho}\nabla \overline{p} + \nu \nabla^2 \overline{\mathbf{u}} + \mathbf{f}_b \tag{2.11}$$

The Reynolds stresses $\mathbf{R}$ are represented by the term $\mathbf{u}'\mathbf{u}'$ and they are viscous stresses associated with molecular diffusion due to turbulent motion. Recalling that the turbulent kinetic energy is defined as:

$$\kappa = \frac{1}{2}\overline{\mathbf{u}'\mathbf{u}'}$$

the tensor $\mathbf{R}$ can be decomposed into its isotropic and deviatoric (anisotropic) parts:

$$\mathbf{R} = \overline{\mathbf{u}'\mathbf{u}'} = \frac{2}{3}\kappa\delta_{ij} + \mathbf{a}_{ij}$$

$$\mathbf{a}_{ij} = \overline{\mathbf{u}'\mathbf{u}'} - \frac{2}{3}\kappa\delta_{ij}$$

The isotropic can be collected and added to the mean pressure, whereas the deviatoric part needs to be modeled. RAS provide two main ways to model the anisotropic part:

1. Reynolds stress tensor models that try to directly come up with relations for each component of the tensor (more recent and still less developed);
2. Eddy viscosity-based models that exploit the Boussinesq's hypothesis for which the Reynolds stresses are supposed to be proportional to the mean velocity gradient through a scalar quantity, i.e. the eddy viscosity (less recent and more used nowadays).

The Boussinesq's hypothesis reduces to:

$$\mathbf{a}_{ij} = \rho\nu_t\left(\frac{\partial \overline{\mathbf{u}}_i}{\partial x_j} + \frac{\partial \overline{\mathbf{u}}_j}{\partial x_i}\right) \tag{2.12}$$

This assumption is valid in cases where the gradient of the velocity is a dominant quantity such as wake, turbulent boundary layers or jets and it makes closed the system of

equations. The only remaining unknown is the turbulent viscosity which is defined in turn as:

$$\nu_t = u^* l^*$$

A variety of turbulence models are distinguished depending on how either the velocity and turbulent length scales or the turbulent viscosity itself are modeled: in general it can be added to the system "zero", one or two transport equations and then the models are respectively called zero-, one- or two- equations models. The transport equation for a generic quantity $Z$ is:

$$\frac{\partial Z}{\partial t} + U_i \frac{\partial Z}{\partial x_j} = \frac{1}{\sigma_Z} \frac{\partial}{\partial x_i} \left( (\nu + \nu_t) \frac{\partial Z}{\partial x_i} \right) + P_Z + \epsilon_Z \tag{2.13}$$

It is recalled in (2.13) just once since at least the form of the equation (and so the terms involved) is always the same, but the quantity considered (e.g. turbulent kinetic energy, turbulent dissipation rate and son on): the left-hand-side is the convective term, the first term of the right-hand-side is the redistribution or gradient diffusion term and finally production and dissipation associated with the quantity Z. All these terms are calibrated in a specific way for each model and they can be customized by means of some (model) constants for each specific problem.

### 2.2.3. DDES

Detached-eddy simulations are considered hybrid simulations since they use RAS close to the wall (boundary layer region) and LES far from it, in order to exploit the power of these two models achieving better solutions and also decreasing the computational cost of a LES model: in fact, LES usually has a computational cost of $\sim Re^2$, whilst RAS of $\sim Re^0$. It is then worth to recall briefly the way of how LES equations are obtained. First they do not consider “conceptual” flows as RAS do and they are based on a scale separation: the latter operation allows to compute the large structures and to model the small ones.
The procedure to build a LES code takes into account few steps that in some ways are similar to those already recalled for RANS in the Section 2.2.2:

1. consider the Navier-Stokes equations (2.4) (2.5);
2. to perform the decomposition in large and small scales motion, a filter operator is introduced which is thus defined:

$$\mathbf{u}(\mathbf{x}, t) = \widetilde{\mathbf{u}}(\mathbf{x}, t) + \mathbf{u}'(\mathbf{x}, t)$$

$$\widetilde{\mathbf{u}}(\mathbf{x},t) = \int\int\int \mathbf{G}(\mathbf{r},\mathbf{x})\mathbf{u}((\mathbf{x}-\mathbf{r}'),t)\,d\mathbf{r}$$

**G** is the low-pass (kernel) filter which it separates large from small scales basing on a cutoff wave number k chosen by the user. It is also important to notice that the quantity $u$ is, in turn, decomposed into its filtered and fluctuating parts.

3. the closure of the system is achieved by solving the filtered equation. To do so, the anisotropic component of the residual stresses has to be modeled (still similarly to RAS):

$$\tau_{ij}^r = \widetilde{u_i u_j} - \widetilde{u}_i\widetilde{u}_j$$

$$\tau_{ij}^a = \tau_{ij}^r - \frac{2}{3}\kappa^r\delta$$

$$\kappa^r = \frac{1}{2}\tau_{ii}^r$$

where the apices $()^r$ stands for residual and $()^a$ for anisotropic.

4. eventually the numerical solution of the filtered equation is obtained (DNS-like).

The difference with respect to RAS codes lies on the fact that $\widetilde{u'} \neq 0$, whereas $\overline{u'} = 0$. So far DES seems to resolve many problems arisen from RAS and LES singularly, so why the need of implementing DDES? Actually not all the problems are solved by DES, in fact the zones where the code switches from RAS to LES is the most critical and it needs to be investigated more specifically. This area is also termed *grey region* and it could be problematic in case of thick boundary layer and shallow separations: for a specific mesh could happen that the grid spacing parallel to the wall could be smaller than the boundary layer thickness itself which it would yield to a length scale fine enough for LES, leading to a premature and non-physical separation of the flow. For the case of DES with the SA [11] turbulence model, the length-scale $\widetilde{d}_{DES}$ is defined in order control the eddy viscosity:

$$\widetilde{d}_{DES} \equiv min(y, C_{DES}\Delta) \tag{2.14}$$

where $C_{DES}$ is a model constant usually of the order of 1 and $\Delta \equiv max(\Delta x, \Delta y, \Delta z)$ is the chosen grid spacing. Depending on the latter either RAS mode for $\widetilde{d} = y$ or LES mode for $\widetilde{d} = C_{DES}\Delta$ are activated, whilst the *grey area* is exactly between. Therefore the grid resolution is a crucial choice for an optimal switching from one to the other model: e.g. when the grid convergence wants to be proved, the grid density could lead to switch to LES mode already in the boundary layer usually due to the DES limiter $\widetilde{d} = C_{DES}\Delta$, reducing, in turn, the eddy viscosity and finally the resolved Reynolds stresses, since there is not a corresponding balance by resolved turbulent content. This phenomenon was termed

by Spalart as modeled-stress depletion(MSD) and it is due to the grid spacing. Some turbulence models "avoid" this issue by operating just in RANS mode, but behaving as LES in case of homogeneous turbulence, such as SAS and TRRANS models. A primitive solution for DES is to disable the $C_{DES}$ limiter just in regions where an attached boundary layer is expected, in order not to introduce non-physical separations, but thinking on a 3D simulation this could be difficult to be set and time-consuming. The idea behind DDES is instead to *delay* a little the use of RANS mode for a thicker boundary layer thanks to another definition for the length-scale:

$$\widetilde{d}_{DDES} \equiv y - f_{d1} max(0, y - C_{DES}\Delta) \tag{2.15}$$

$$when\ f_{d1} = 0(RANS) \quad \widetilde{d}_{DDES} \equiv y \tag{2.16}$$

$$when\ f_{d1} = 1(LES) \quad \widetilde{d}_{DDES} \equiv min(y, C_{DES}\Delta) \tag{2.17}$$

This new length scale behaves as a limiter when its value is somehow far from $C_{DES}$, i.e. when either $y << C_{DES}\Delta$ or $y >> C_{DES}\Delta$ (2.16), whilst is equal to $y$ when it is close to the value $C_{DES}\Delta$ (2.17).

$$f_{d1} \equiv 1 - tanh([8r_d]^3) \tag{2.18}$$

$$r_d \equiv \frac{\nu_t + \nu}{\sqrt{\frac{\partial u_i}{\partial x_j}\frac{\partial u_j}{\partial x_i}}\kappa^2 y^2} \tag{2.19}$$

The $f_{d1}$ parameter is designed *ad hoc* to assume the expected values depending on the considered point is either inside or outside the boundary layer, so the code automatically can switch from one mode to the other one: for instance, for massive flow separation $f_{d1}$ increases at most($f_{d1} = 1$) and LES mode is switched on. At the same time $r_d$ is slightly modified from the standard SA implementation to be applied to any eddy-viscosity-based models.

### 2.2.4. IDDES

The non-physical separation of the flow mentioned during the section 2.2.3 actually goes under the name of grid-induced separation(GIS), because it is due to a sudden mesh refinement nearby the *grey regions*. For the sake of clarity, the MSD phenomenon is instead referred to an underestimate of the eddy-viscosity without a corresponding balance by resolved turbulent content, passing from RANS to LES. Therefore GIS is a consequence of MSD and both are due to problems with the grid refinements. The GIS' issue is the

the basis of the IDDES formulation. This kind of problem can usually happen for the case of wall-bounded flows where the flow instabilities are such little developed that they would require many boundary layers thicknesses to reconstruct a sufficient LES turbulent spectrum content which it balances the RAS turbulent content reduction. DDES shield RANS from LES nearby the wall boundary layers, in order not to have the transition from one model to the other one inside the boundary layer. Another possible improvement is proposed with IDDES: they combine WMLES in the near-wall region and DDES. WMLES are fully LES models, so they do not use no-slip boundary conditions as RANS do. A special treatment of the inner region of turbulent boundary layers is achieved by means of both an algebraic and ordinary differential equations [12] and sometime a good candidate could be a separate auxiliary RANS solution that covers only the distance between the wall and the wall-model location [13]. The IDDES shielding function $f_{d2}$ is somehow similar to the DDES one (2.18):

$$f_{d2} = 1 - tanh\left[C_{dt1} \cdot r_d^{C_{dt2}}\right] \tag{2.20}$$

The coefficients $C_{dt1}$ and $C_{dt2}$ are usually and respectively taken equal to 3 and 8 as for DDES, actually it has been proved that there is some degree of freedom for $C_{dt2}$, in fact for the case of a plane channel [14] if it was set to 20, it could match well the experimental data at least when DDES is coupled with the SST turbulence model. For what concerns the car test case, Ekman[5] modified the constant $C_{dt1}$ to a value of 20 and 40 to delay the separation for the case of the $IDDES_{\kappa-\omega SST}$ model achieving more reliable results.

## 2.3. Turbulence models

Nowadays there is not universal definition of turbulence, but it is common thought to define it as the chaotic change in space and time of the velocity and pressure of a flow. Turbulence is present in all phenomena involving fluids and depending on the way it is treated, different turbulent models are distinguished.

### 2.3.1. SA model

Spalart–Allmaras is a one-equation model and it relies on a transport equation(2.13) for the modified turbulent viscosity $\widetilde{\nu}$. This equation has been created from scratch to build a not-expansive model from a computational point of view and it gives reasonable results in terms of mean flow, in fact it works well for instance for transonic flows over airfoils

and boundary layer separation. The turbulent viscosity is reconstructed as follows:

$$\nu_t = \widetilde{\nu} f_{v1}$$

$$f_{v1} = f(\chi)$$

$$\chi = \frac{\widetilde{\nu}}{\nu}$$

Is is worth to underline that $\nu$ is a fluid property and it is used to found the eddy viscosity which it cannot be considered a fluid property, rather it can be a flow property. The initial value of $\widetilde{\nu}$ has to be set in the $0/$ dictionary and it has been found starting from some initial condition of the $\kappa - \epsilon$ model:

$$\kappa = \frac{3}{2}(i|u_{ref}|)^2 \tag{2.21}$$

$$\epsilon = \frac{C_\mu^{0.75}\kappa^{1.5}}{\widetilde{L}} \tag{2.22}$$

Finally the $\widetilde{\nu}$ is thus initialized:

$$l = C_\mu \frac{\kappa^{1.5}}{\epsilon} \tag{2.23}$$

$$\widetilde{\nu} = \sqrt{\frac{3}{2}}(u_{ref} i l) \tag{2.24}$$

So the numerical values change depending on the investigated case. This type of model is widely used for real applications nowadays with a good agreement with experiments.

### 2.3.2. $\kappa$ - $\epsilon$ model

This is a two-equations-model and it relies on two transport equations, one for the turbulent kinematic energy and the other one for the turbulent kinematic energy dissipation. The eddy viscosity is found by means of this recurrent formulation:

$$\nu_t = C_\mu \frac{\kappa^2}{\epsilon} \tag{2.25}$$

and the initial values are computed accordingly to the formulas (2.21) and (2.22). The value of the coefficient $C_\mu$ is assumed to be constant and equal to 0.09 for such model. However, this model has some limitations due to the definition of the turbulent kinetic energy which is a quantity that is not defined at the wall, so it can be either used for solving just the flow far from the wall or it can be improved as it is going to be shown in the next section. In general, it is a good practice to create a mesh with high values of $y^+$,

i.e. greater of 30-50(at least), to solve the flow at a "sufficient" distance from the wall.

### 2.3.3. R$\kappa$ - $\epsilon$ model

The realizable $\kappa$ - $\epsilon$ is still a two-equation model which exploits the definition of eddy viscosity presented in (2.25), but with a different definition of $C_\mu$ which it is not considered constant anymore:

$$C_\mu = \frac{1}{A_0 + A_S U * \frac{\kappa}{\epsilon}} \tag{2.26}$$

This coefficient is now assumed to be inversely proportional to the ratio between the turbulent kinetic energy and the turbulent dissipation rate by means of two constants $A_0$ and $A_S$ , where $A_0$ is calibrated depending on the type of flow and its value can be found tabulated, whilst $A_S$ is related to the mean strain rate. This model is an improvement of the standard $\kappa$ - $\epsilon$ since it calibrates the eddy viscosity content basing also on the velocity. It works fine for different types of flows such as rotating homogeneous shear flows, massive flow separation and it has been proved to match well also with experimental data [15].

### 2.3.4. $\kappa$ - $\omega$ model

This is a two-equations model and in addition to the equations for the turbulent kinematic energy, there is a transport equation for the turbulence specific dissipation rate which is defined as $\omega = \frac{\epsilon}{\kappa}$. The initial value to be set in the 0/ dictionary is:

$$\omega = \frac{\kappa^{0.5}}{{C_\mu}^{0.25}\widetilde{L}} \tag{2.27}$$

Then the eddy viscosity is computed:

$$\nu_t = \frac{\kappa}{\omega} \tag{2.28}$$

It is well-known that this model works better close to the wall and it could encounter stability problem far from it, nevertheless its formulation is exploited for combined models.

### 2.3.5. $\kappa$ - $\omega$ SST model

The Shear Stress Transport $\kappa$ - $\omega$ embeds two different models: the $\kappa$ - $\omega$ close to the wall, specifically in the inner viscous sub-layer, and the $\kappa$ - $\epsilon$ far from it, in this way it results to be a more efficient method from a computational point of view, as well as in terms of results. It switches also to the $\kappa$ - $\epsilon$ for the inlet flow where the $\kappa$ - $\omega$ is highly

sensitive to the inlet conditions. In this case the eddy viscosity is reconstructed as:

$$\nu_t = a_1 \frac{\kappa}{max[a_1\omega, b_1 F_2 S]} \tag{2.29}$$

where $S$ is computed from the shear rate:

$$S = \sqrt{2 S_{ij} S_{ij}}$$

$$S_{ij} = \frac{1}{2}\left(\frac{\partial u_i}{\partial x_j} + \frac{\partial u_j}{\partial x_i}\right)$$

This model works well for separating flows and, although it generates a lot of turbulence in critical regions (e.g. stagnation points or strong velocity gradients), it represents an improvement of both reference models [16].

### 2.3.6. SAS $\kappa$ - $\omega$ SST model

This model relies on the URANS formulation presented in the equations (2.4) and (2.5). Nowadays the URANS "concept" can be interpreted in different ways depending on how the turbulent structures are intended to be solved. In this chapter two different concepts are proposed, specifically a classical and a more modern view, the latter is closer to the SAS models. About first school of thought, one could think about URANS as simulations that are not capable of reconstructing the turbulent spectrum since they averages out all the turbulent fluctuations by resolving just the very low frequencies far from the turbulent fluctuations [17]. More recent studies have proved that SAS are in some ways *advanced* URANS in the sense that they can produce a more complete turbulent spectrum by exploiting a specific formulation proposed by Rotta. This formulation is based on two transport equations(two-equations-model), one for the turbulent kinetic energy and the other one is an exact transport equation for the $\kappa L$ variable, in fact it is termed $\kappa - \kappa L$ model. This formulation relies on a large-scale equation for the turbulence, so it needs of a modeling for each term of the turbulent stresses. Furthermore third derivative of the velocity is present in the $\kappa L$ equation which it is a distinguish factor of the source term. The latter could be problematic, specifically in case of in-homogeneous flow, where it is better to consider the second velocity derivative because it allows to reconstruct the velocity in the logarithmic layer. SAS is able to operate in Scale-Resolving mode, also balancing automatically the resolved and modelled parts of the turbulent spectrum. The $\kappa - \kappa L$ model is then further modelled in order to get to the KSKL one-equation-model, which is more compact and as much valid as the standard one. This final formulation is achieved by writing one transport equation for the $\phi = \sqrt{\kappa} L$ variable. For completeness

the equations for $L$ and $L_{vk}$ are reported to identify the differences [2] :

$$\kappa L = \frac{3}{16} \int_{-\infty}^{\infty} \mathbf{R}_{ii}(\mathbf{x}, r_y) dr_y \tag{2.30}$$

$$L_{vk} = \kappa \left| \frac{\partial U/\partial y}{\partial^2 U/\partial y^2} \right| \tag{2.31}$$

Such definition of $L_{vk}$ ensures a positive contribution inside the $\phi$-equation and it is the generalization of the boundary layer in case of three dimensional flows. The definition (2.30) returns $\kappa y$ in the logarithmic layer, it also means that the size of the large turbulent eddies increases linearly with the wall distance. The model is so termed Scale-Adaptive Simulation, because it behaves by adjusting to the resolved scales: in fact, it returns the length-scale of the mean flow independently from the layer thickness, whilst the standard SST model gives a length-scale proportional to the layer thickness.

[2] $\mathbf{R}_{ij}$ is two-point correlation tensor and $\mathbf{R}_{ii}$ is computed as the sum of the diagonal terms of $\mathbf{R}_{ij}$ measured at the location $\mathbf{x}$ by means of two probes displaced of $r_y$. $\mathbf{R}_{ij}$ has a maximum at $r_y = 0$ and it decays as the distance between the two probes becomes larger.

## 2.4. Tools used for this investigation

The software used for all the simulations is OpenFOAM® v2012 which is an open-source and free CFD software. The simulations have been launched on Galileo 100 which is one of the new infrastructure available in CINECA[18]. It counts of 528 computing nodes each 2 x CPU Intel CascadeLake 8260, with 24 cores each, 2.4 GHz, 384GB RAM.
The data have been extracted and visualized by means of ParaView which is an open-source, data analysis and visualization application and finally the post-process has been performed with Matlab R2021a, a language and numeric computing environment developed by MathWorks.

# 3 | Turbulent flow around the cylinder

## 3.1. Summary

The following chapter presents the study of the flow around a cylinder. This type of analysis is commonly used for aerodynamics purposes and it is intended to focus more on the methodology that needs to be used for the next steps.
First the literature has been analyzed and interesting insights, as well as strong and weak point of the experiments, are presented. The mesh is thus generated accordingly with a specific focus on the wake where some refinement regions are generated. Then the goal is to implement the turbulence models, both RAS and DES, and test them. To perform the validation, the mean pressure distributions along the surface are plotted along with the James' experiments[19], showing the local pressure differences where the CFD data deviates more from the test, spotting their locations in terms of angles. Finally, the analysis is enriched with some other interesting considerations about the aerodynamics forces and the separation angle. During the solving process differences of RAS and LES regions are identified by means of the *DDES model regions* utility and possible causes are highlighted by means of eddy viscosity visualizations.

## 3.2. Case study

The flow characteristics around a cylinder are completely different with respect to those on the car, however a similar flow regime is chosen at least to match the one of the following studies, so the first thing to be set is the Reynolds number which in this case is $Re = 3.6 \cdot 10^6$. This is not the only reason behind this choice, there have been several attempts at lower Reynolds number, keeping the same order of magnitude ($10^6$), but at those Reynolds the flow regime is mostly uncertain, because of a transition from laminar to turbulent boundary layers which it is not completely ended. Moreover the so-called *drag crisis* region occurs and measurements at this condition are uncertain and affected by the flow regime. So a larger Reynolds number is chosen in order to avoid any of these errors. The problem is unsteady and it can be outlined as follows:

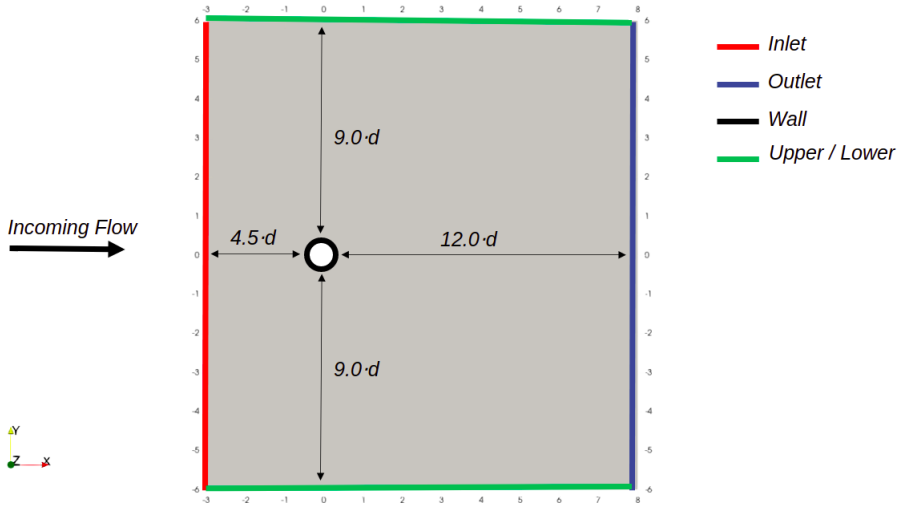


Figure 3.1: Problem setup: cylinder in a uniform flow

For the sake of simplicity, a 2D problem is presented in figure 3.1 to highlight the geometry and the inlet/outlet conditions. The model validation is performed at the center line plane(2D) of the cylinder, but OpenFoam works always with 3D meshes so a 3D mesh is needed. Particularly, the thickness along the third spacial direction is of 5m. More details concerning the problem dimensions are given in the following chapters, whilst the initial conditions are set depending on the turbulence models as mentioned in the Chapter 2.

Nevertheless, the velocity and the pressure have always the same values and they are set as follows:

| | **Inlet** | **Outlet** | **Upper / Lower** | **Wall** |
|---|---|---|---|---|
| **u** [$\mathrm{m\,s^{-1}}$] | 85.5 | *inletOutlet* | *Symmetry* | *fixedValue* |
| **p** [Pa] | *zeroGradient* | 0 | *Symmetry* | *zeroGradient* |

The velocity field is uniform and its value comes out of the Reynolds number scaled on the diameter, similarly the pressure at the outlet is considered to be uniformly 0 Pa. The *zeroGradient* is imposed for the pressure at the inlet and at the wall, this means that the turbulent profile is completely developed and there are not gradients at the inlet portion of the domain, in other words it is considered a *free-stream* condition. The value of *inletOutlet* is given by the inlet value of the velocity vector field, it has to be specified in OpenFOAM, and it behaves similarly to the *zeroGradient* boundary conditions, but if some backward flow are detected, it switches to a *fixedValue*, so it is a mixed boundary condition. On the upper and lower planes, as well as on the front and back ones, the *symmetry* boundary condition is imposed to focus on what happens on the wake and simulates what happens during the experiments. Finally, the no-slip boundary condition is imposed on the cylinder surface by means of either a *fixedValue* boundary condition or *wall-functions* when necessary.

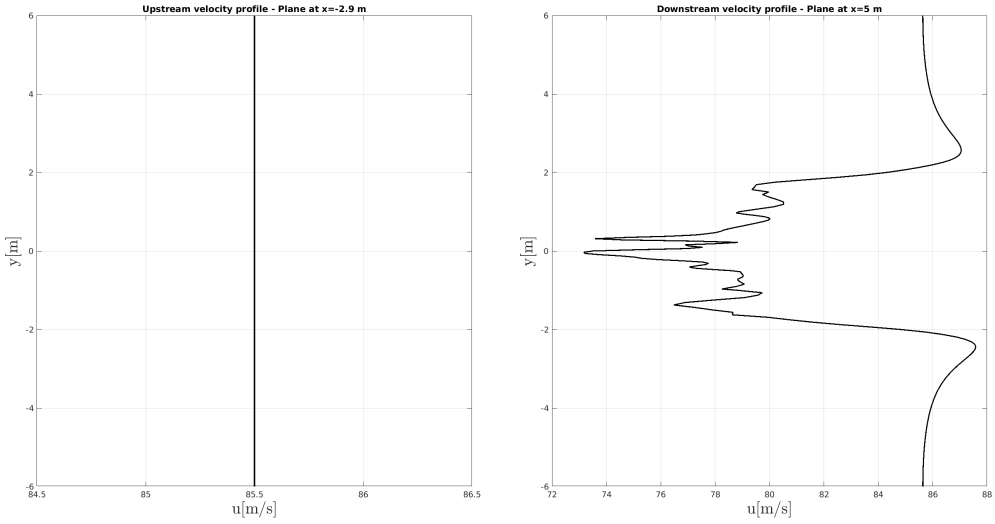


Figure 3.2: Velocity profiles at the inlet(on the left) and at the outlet(on the right)

At an intersection plane placed at $x = -3m$, it corresponds an inlet velocity profile which has to be the constant value specified in the initial condition, i.e. $u_\infty = 85.5\mathrm{m\,s^{-1}}$, whilst

downstream the cylinder, namely at $x = 5m$, it is evident the behaviour of the velocity field which is affected by the presence of the body and it changes its nature becoming unstable and generating a low pressure region. The downstream velocity profile is representative of a turbulent flow: it exhibits a lot of fluctuations and it has a recirculating area in correspondence of the wake. The flow regime is rather affected by the initial conditions and the Reynolds number is a representative parameter to identify the type of (theoretical) flow behaviour. By changing this number a variety of flow regimes can be identified for the case of a cylinder.

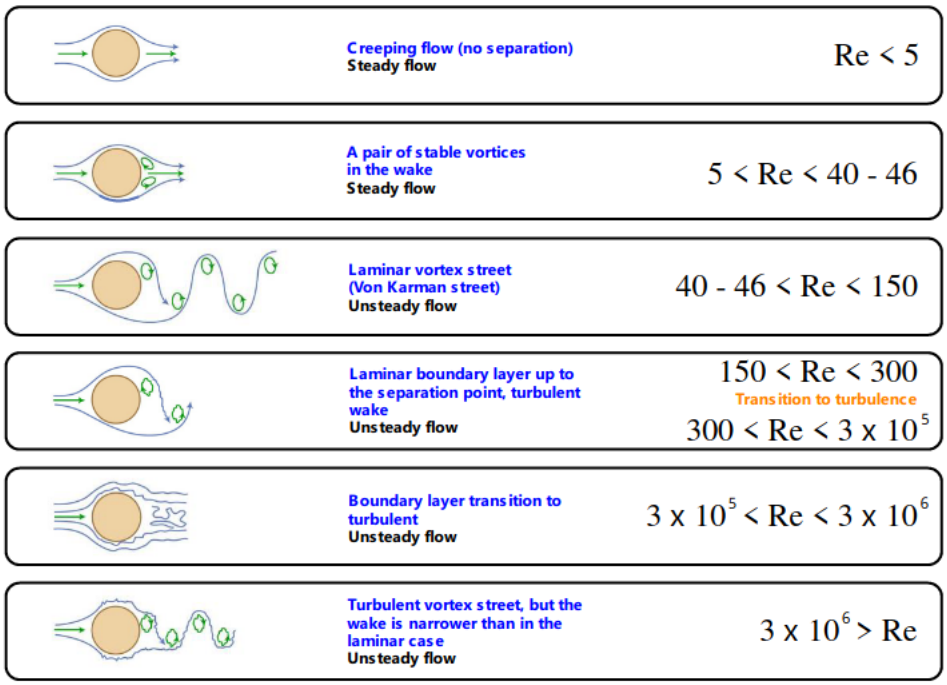


Figure 3.3: Flow regimes of the cylinder[20]

At very low Reynolds ($Re << 1$) the flow upstream and downstream is almost symmetrical with respect to the cylinder, but the body affects the flow and the free-stream velocity is recovered at large distance which is somehow proportional to several cylinder diameters. This symmetrical behaviour disappears more and more as the Reynolds increases. When $5 < Re < 40$, the fluid particle which is moving around the cylinder reaches the rear point of symmetry and then it moves far away from it: at these Reynolds two small recirculating zones are obtained downstream and "attached" to the body, this region, the wake, becomes larger with the Reynolds. Going beyond the limit of $Re = 40$, instabilities arise spontaneously due to the problem setup. Firstly, the instabilities show in the wake, then, as $Re = 100$ is reached, the instabilities becomes larger: for $Re < 150$ eddies are

shed from the cylinder with a periodic frequency and the so-called *von Kármán vortex street* is generated. The vortices on opposite sides rotate with opposite directions and they identify regions of locally high vorticity, once they are detached, they move longitudinally far away from the body with a velocity that is smaller than the free-stream one. At $150 < Re < 300$ the transition towards turbulence occurs along the wake regions which implies the existence of irregular and rapid changes of the pressure and velocity fluctuations over time and space. Then the vortex street becomes fully turbulent and this behaviour is recognizable up to $Re = 3 \cdot 10^5$. When $3 \cdot 10^5 < Re < 3.5 \cdot 10^6$ another instability phenomenon occurs, this time it involves the boundary layer. Previously at $Re < 3.5 \cdot 10^5$ the separation was laminar, whilst now a more complex phenomenon occurs: the fluid that is moving close to the wall, it moves for a while far from it and then it reattaches to the wall. This *turbulent reattachment* is a quick phenomenon both in space and time such that the separation point is just a little delayed downstream along the cylinder. This transition could be also asymmetrical between the two sides of the cylinder and (in general) some changes could be identified in the flow-field during the tests.
Only at very low Reynolds numbers the problem can be studied analytically, whilst for high Reynolds the flow is studied either experimentally or numerically, for this specific work a numerical approach has been chosen.

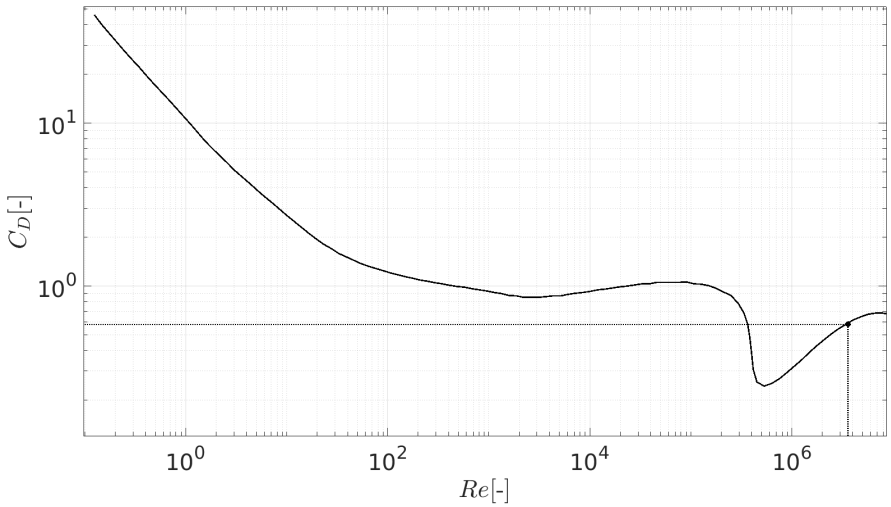


Figure 3.4: Experimental drag variation with Reynolds number for a smooth cylinder[21]

Figure 3.4 shows the behaviour of the drag at various of Reynolds numbers: due to the transition to turbulence flow, highly irregular phenomena occur, the drag does not follow the same trend identified so far and the so-called *drag crisis region* can be identified. Finally, for $Re > 3.5 \cdot 10^6$ the boundary layer is fully turbulent. At these critical Reynolds the wake is thinner than before and a sort of re-establishment of the vortex street is

obtained. So this is the expected flow-field of these simulations.
Momentum is removed from the fluid due to the interaction between fluid and obstacle, specifically the flow must be slowed down in the wake region (Figure 3.1). The drag is shown in non-dimensional terms, namely with the drag coefficient:

$$C_D = \frac{D}{\frac{1}{2}\rho u_\infty^2 A}$$

The reference area used for such case is $A = d \cdot t$, where for the thickness is meant the length in the third spacial direction or *z-direction*. At low Reynolds is possible to see a trend defined rather approximately as $C_D \propto \frac{1}{Re}$, then there is a rather small decreasing rate up to $Re = 10^5$ and here a decreases of a factor 3 is recorded in the drag crisis region: this drop is quite fast such that the drag decreases even if the flow is speeding up, finally at higher Reynolds the drag drop is recovered and a sort of (turbulent) vortex street is generated.
Another important parameter to be monitored is the Strouhal number. This non-dimensional quantity gives an estimation of the shedding frequency which is made dimensionless with the ratio of the diameter over the free-stream velocity:

$$St = \frac{fd}{u_\infty}$$

It is dependent on the Reynolds number and so on the flow regime and its trend can be somehow similar to the drag coefficient.

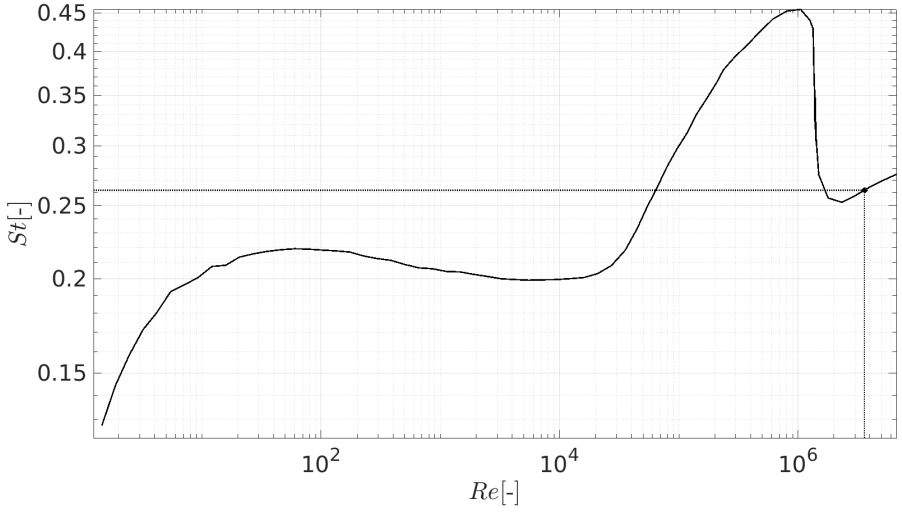


Figure 3.5: Experimental Strouhal variation with Reynolds number for a smooth cylinder[21]

The Strouhal number increases with the Reynolds number and in the drag region crisis a maximum is reached. Then there is a drop and the trend is closer to the one before to the crisis region and finally a recovery. So higher Reynolds means also higher Strouhal number which, in turn, generates higher frequency: results at higher Reynolds are affected by higher oscillations. Experimentally, it has been observed that the vortex street is somehow re-obtained at these high Reynolds with much more fluctuations and with a smaller wake, so it is important to highlight that a similar behaviour can be recognized at different ranges of Reynolds.

### 3.2.1. Literature review

Although the flow around a cylinder is commonly studied in laboratories and a lot of literature could be found to perform the validation, in this case due to the high Reynolds used for the simulations just three articles deal with this kind of experiments, probably because it is difficult to set an experiment and take measurements and the results can be affected by any form of irregularities during the executions of the experiments. One of the most important reference on the matter is represented by the Achenbach's experiments [22], however this reference is lacking different points.

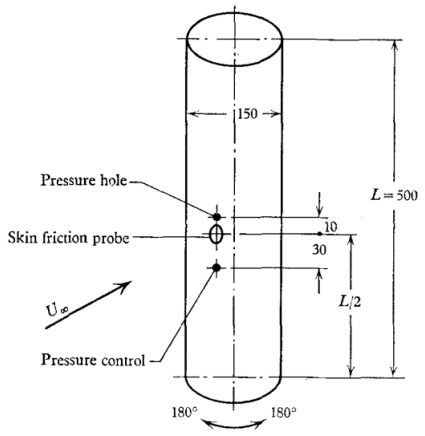


Figure 3.6: Achenbach's experiments set up [22]

Achenbach performed his experiments in a wind tunnel test with a test section 500x900$mm^2$ and the fluid was air. Different cylinders with various AR (from 3 to 10) were used to validate the experiments. In Figure 3.6 are highlighted the probes positions, specifically a skin-friction probe is located at half of the cylinder and a pressure hole in the vicinity of the middle plane. The cylinder can be rotated around its longitudinal axis in order to measure the pressure distribution along the cylinder surface. Another important thing to be noticed is that the cylinder goes from wall to wall in the test section and the board effects are neglected since it can be somehow considered a 2D experiment, in fact the pressure distribution are just measured a certain location along the longitudinal axis. The latter point is a common feature present also in the other two references, i.e. James' [19] and Shewe's [23] experiments. The most important deficit in this reference is that the surface roughness is not specified, so it is not recommended to use this data and find a reasonable match for other studies. In fact, the surface roughness becomes an important parameters which affects a lot the aerodynamics forces: the rougher the surface, the higher the wall-shear stresses, particularly the skin-friction coefficient is higher at low Reynolds, then it tends to decrease up to a limit. Furthermore during the post-processing of those

experiments there were not considered blockage corrections in order not to contaminate results by other theories. The blockage ratio is defined as:

$$\frac{A_{cylinder}}{A_{TestSection}} \cdot 100\%$$

where these areas have to be intended either as frontal areas or wet areas (where the flow is impinging). In these experiments it was of $\approx 17\%$ which is quite a high value, in fact the blockage effects can be considered negligible just below $\approx 5\%$. Eventually all these potential source of errors lead to an overestimate of the drag coefficient with respect to other references.
Second and most important reference used for the validation of such study are the experiments conducted by James [19] in 1980.

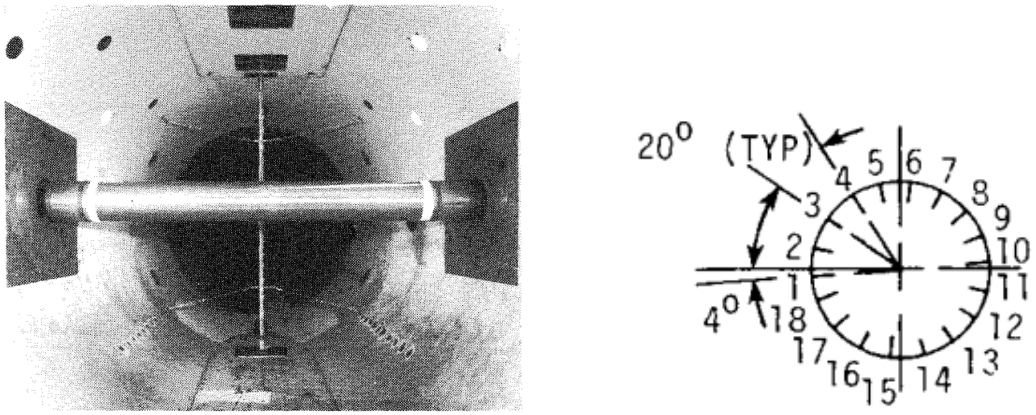


(a) NASA Ames 12-ft pressure wind tunnel downstream view

(b) Static pressure ports placed at the middle section

Figure 3.7: James's experiments set up [19]

The test section is almost cylindrical and the fluid is air. Different cylinders with AR from 5 to 10 were considered. The cylinders were mounted on flanges spanning horizontally the wind tunnel as shown in figure 3.7. To measure the pressure along the cylinder surface, 18 static pressure ports are place on the surface spaced equally by 20°. The blockage ratio in this case is much lower $\approx 2.5\%$, so eventually blockage effects did not affect too much the results. The surface roughness is specified and scaled with respect to the diameter, so it was $\frac{\kappa}{D} = 3.6 \cdot 10^{-6} cm/cm$.
Third reference used for the validation are represented by the experiments performed by Schewe at al. [23] in 1983. Although these experiments did not measure the pressure distribution along the cylinder which is the core point used for the validation, it is more recent with respect to the James' one and it is more focused on the force measurements,

so it is used for the comparison of the aerodynamics forces. The test section of the wind tunnel had the dimensions of 600x600$mm^2$ and only one cylinder were tested with an AR of 10.

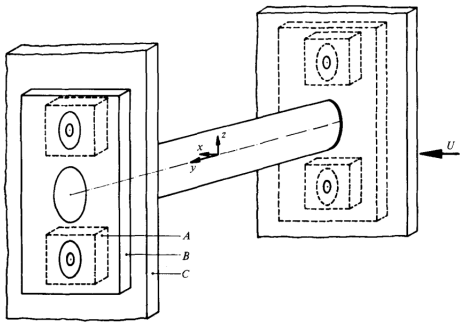


Figure 3.8: Schewe's experiments set up [23]

The cylinder goes from wall to wall and the forces measurements are taken by means of a 3-component piezoelectric force-measuring elements designed *ad hoc* and placed at the wall-location. No blockage corrections were considered even if the blockage ratio is lower than the Achenbach's one, in this case it is $\approx 10\%$.

### 3.2.2. Reference solution

The core reference to be used for the validation is the static pressure coefficient distribution given by James in [19].

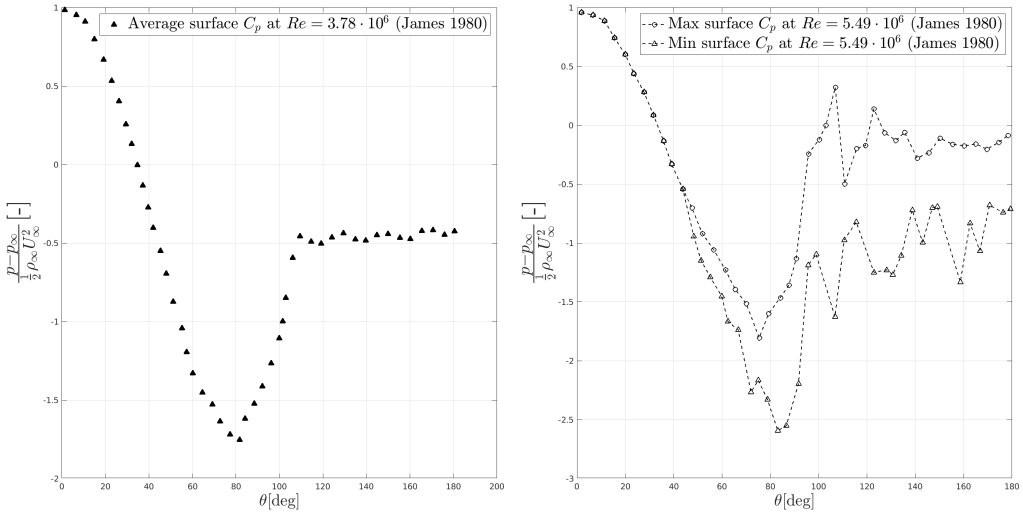


Figure 3.9: Reference static pressure distributions [19]

The plane used in the simulation will be the same of the experiments, so the centerline one. The validation is performed with the average surface static pressure coefficient distribution from 0° to 180°, whilst in Figure 3.9 are plotted also the maximum and minimum surface static pressure coefficient distribution at a different Reynolds at each port location which should give a qualitative range where the data coming from the simulation has to lie. To sum up all the references presented, the experimental drag coefficient is plotted against the Reynolds number:

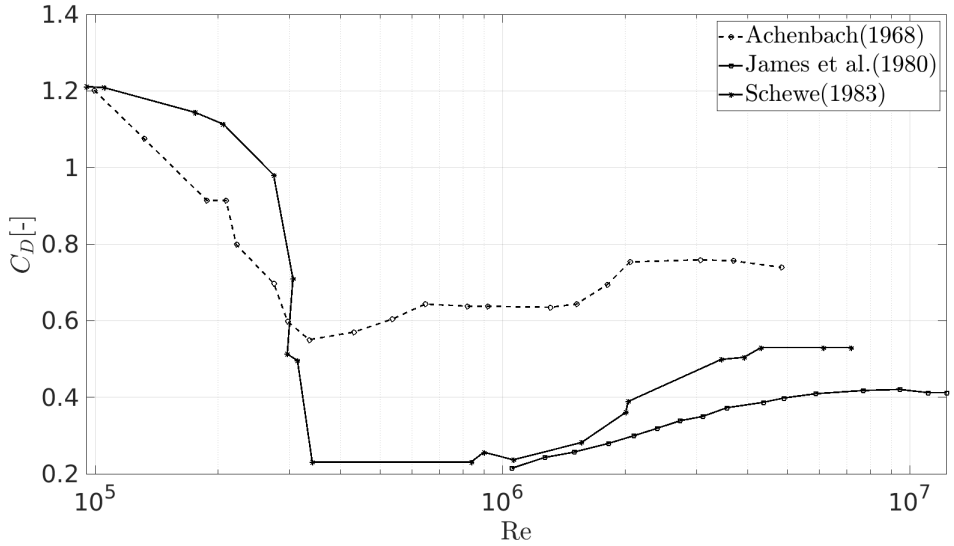


Figure 3.10: Drag coefficient at various Reynolds number for the three references

It is possible to notice that in a range close to $Re \approx 10^6$ the drag crisis occurs for all the experiments. Here the measurements are more uncertain and it is a critical regime in terms of flow since it is a transitional process. As the Reynolds increases the drag tends asymptotically to some limit, where the numerical simulations are performed. The main parameters of all the references at $Re = 3.6 \cdot 10^6$ are collected in the following table:

| | **Achenbach(1963)** | **James(1980)** | **Schewe(1983)** |
|---|---|---|---|
| $C_D[-]$ | 0.75 | 0.35 | 0.49 |
| $\theta[°]$ | 115 | 106 | / |
| $St[-]$ | $0.03 - 0.29$ | 0.2 | 0.2 |
| $AR[-]$ | $3 - 6$ | $5 - 7$ | 10 |
| $\kappa/D[cm/cm]$ | / | $3.0 \cdot 10^{-6}$ | / |

Table 3.1: References values of the experiments

One can notice that the drag recorded during the Achenbach's experiments is much higher than the others, this can be due to the high blockage effect, but eventually to the surface roughness which is not specified, as well. The drag coefficients found by James and Schewe are much similar and lower than Achenbach's one, first because the blockage factor is much lower in James' experiments, but also because it is specified the surface roughness normalized with respect to the diameter and it has quite a low value. Schewe et al. did not give a precise value of the surface roughness, but he states that *"[...]The surface of the cylinder was painstakingly finished and finally polished."*[23], so the accuracy of the results should not be affected too much by it.
The separation angle, $\theta$, is an important indicator of how the flow is developing around the cylinder: the way how it is computed is based entirely on the wall shear stress distribution, in particular when the shear stresses change the sign, the separation occurs, in other words when the gradient of the velocity is zero. By monitoring this parameter it is possible to validate the model not only by looking at the static pressure coefficient distribution, but also in terms of skin-friction coefficient distribution and together this two indicators contribute to the overall drag generated on the body.
The Strouhal numbers have not low values, this goes with the fact that at critical Reynolds values, the measurements are affected by a lot of fluctuations. After a comparison with the pressure distribution, the separation angle is analyzed and finally, the range of values of the drag given by both James and Schewe is considered.

## 3.3. Methodology

The goal is now to solve the problem numerically. The cylinder is inserted inside a block where the case mesh is generated. To solve the flow around the body, the pimpleFoam solver available in OpenFOAM is used. This allows to solve incompressible and transient problems and it requires always at least three entries in the *0* folder which are the velocity, pressure and the eddy viscosity, then depending on the specific turbulence models, other entries need to be added inside this directory (e.g. for the RAS $\kappa - \omega$ SST model, the turbulent kinetic energy and the turbulent specific dissipation rate need to be initialized). The turbulence model, as well as the case mesh, are specified inside the *constant* folder. For all the simulations the *number of outer correctors* is 5, so this is the maximum value for which the momentum and pressure equations are iteratively solved up to convergence, whilst the number of correctors is 2, which means that up to twice the pressure equation can be solved during each outer iteration. The tolerances for all the equations (momentum, pressure or other specific equations) are set to $1 \cdot 10^{-6}$ , moreover to have a more accurate initialization, the associated potential flow problem is solved before the real case. These specifications are all inside the system/fvSolution file.

### 3.3.1. Computational model

The computational domain is generated starting from the cylinder. Once the dimensions are set, it is included inside a block, created with BlockMesh. The dimensions of the block fit with those of the cylinder in a way that the blockage factor is similar to the one used during James' experiments.

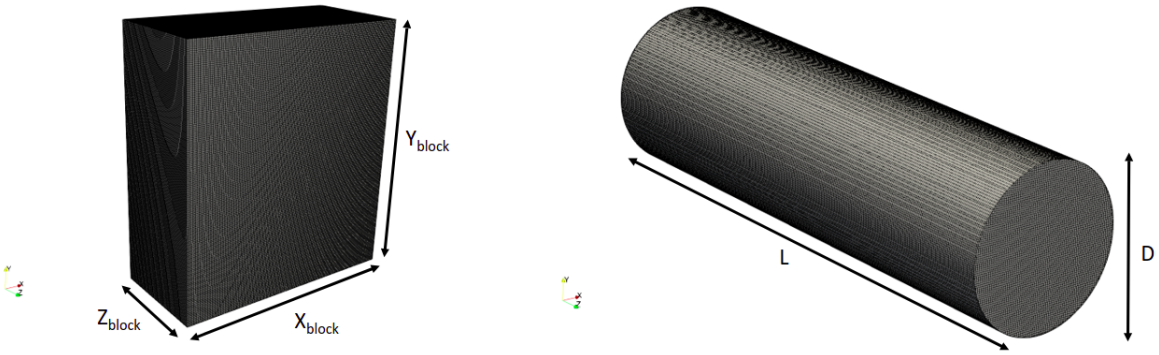


Figure 3.11: BlockMesh and cylinder mesh

The AR in BlockMesh is the ratio of the number of cells along a specific spacial direction and its relative length (e.g. $X_{block}$, $Y_{block}$ and $Z_{block}$ defined in Figure 3.11). To generate correctly the mesh, i.e. the boundary layer mesh and the refinements regions, the utility snappyHexMesh requires at least the AR to be equal to 1 (at least or lower). This condition is fulfilled for each of the three spacial directions. On the other hand, the AR of the cylinder is defined as the ratio of the length and the diameter and for this case is 3.33.

| | **Value[m]** | **Number of blocks[-]** |
|---|---|---|
| $\mathbf{X}_{block}$ | 11 | 11 |
| $\mathbf{Y}_{block}$ | 12 | 12 |
| $\mathbf{Z}_{block}$ | 5 | 5 |
| **D** | 0.67 | / |
| **L** | 2.23 | / |

Table 3.2: Mesh settings of the cylinder test case

Considering that the flow is moving from the left to the right, so towards the positive x-direction, the cylinder is located 3 meters far from the inlet to focus on what happens

downstream, in the wake. The blockage factor in this case is $\approx 2.5\%$ which is very close to the one used by James, whereas the AR of the cylinder, defined as $AR = \frac{L}{D} = 3.33$, is a compromise between the mesh and the experiments. Achenbach explains that as the AR increases the board effects tends to decreases, so ideally for a cylinder with an infinite length the board effects are negligible, in particular for $AR > 3.0$ these effects should not be recognizable. However, James during his experiments used a cylinder with a greater AR, but from a computational point of view increasing the AR means increasing the mesh size as well, and so the computational cost. For those reason the AR is chosen to be 3.33 in order to both avoid wall effects and not to have a number of cells which is too high.

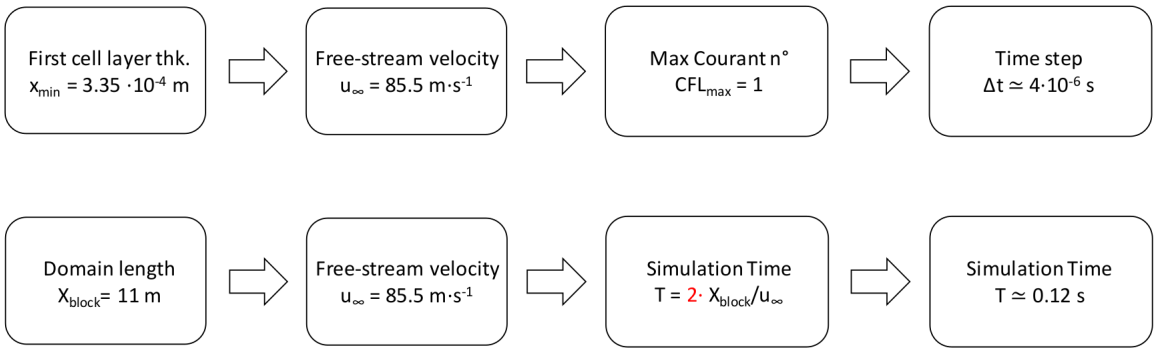


Figure 3.12: Simulation settings of the cylinder test case

The stability of the simulations is imposed by ensuring the CFL condition for which the Courant number, $CFL = \frac{u_\infty \cdot \Delta t}{x_{min}}$, has to be lower than 1, where the $x_{min}$ is the minimum cell size and so it is the first cell boundary layer thickness. In the Figure 3.12, the time step is found to be $\Delta t = 4 \cdot 10^{-6}$s, whereas the total simulation time is given by *twice* the time the inlet flow takes to reach the outlet and it turns out to be $T = 0.12$s. These settings are kept the same for all the turbulence models.

### 3.3.2. Mesh generation and description

The mesh is hexa-dominant and it is modeled by mans of four refinement regions which have the aim to focus on the wake and what happens in the far downstream region.

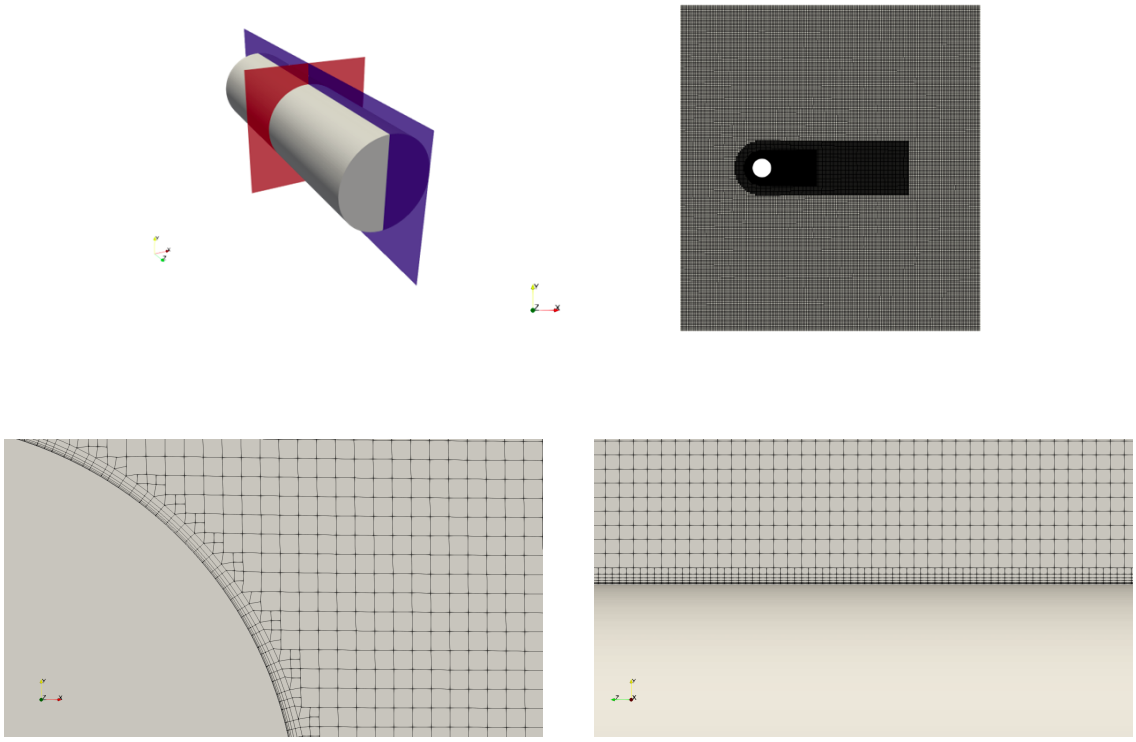

(a) XY plane(red plane) (b) YZ plane(blue plane)

Figure 3.13: Boundary Layer mesh of the cylinder

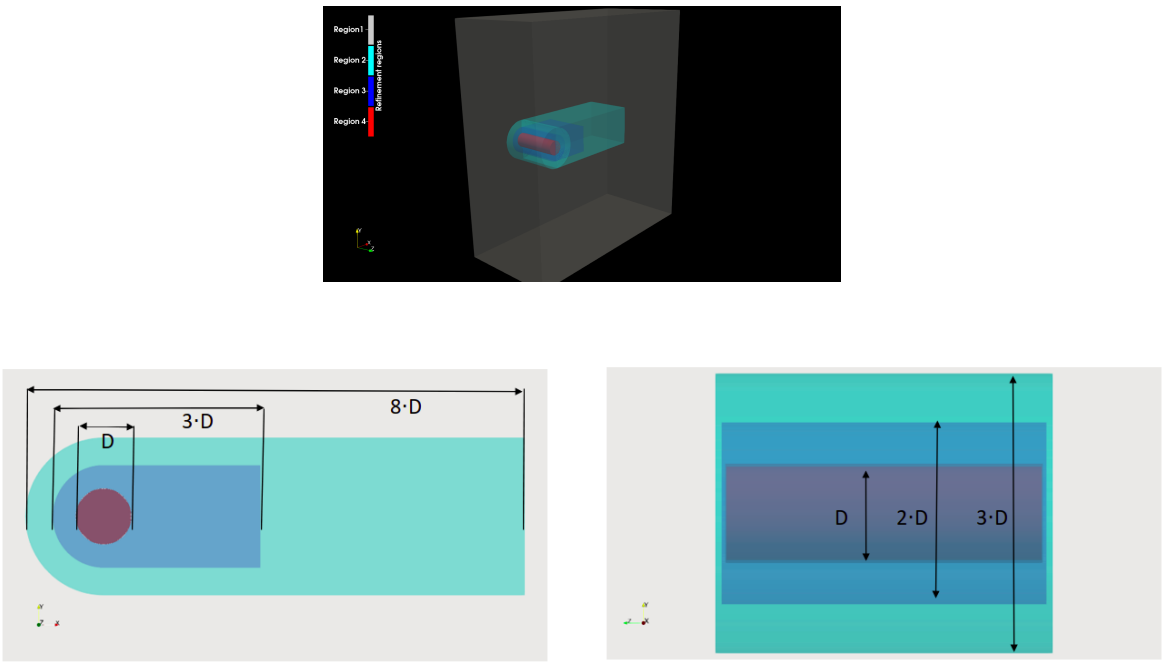


(a) XY plane(red plane) (b) YZ plane(blue plane)

Figure 3.14: Refinements regions of the cylinder

The general hypothesis behind the full mesh generation is that the same mesh is used for all the families of equations (RAS and DES) and for the tested turbulence models. It is known in literature that different models behaves differently and this is strongly related to the mesh. However, it is necessary to exploit this assumption to have a reasonable comparison.

| | |
|---|---|
| **Boundary Layer thickness $\delta$ [m]** | $\approx 1.2 \cdot 10^{-2}$ |
| **First cell layer thickness $x_{min}$[m]** | $3.35 \cdot 10^{-4}$ |
| **Last cell layer thickness [m]** | $4.40 \cdot 10^{-3}$ |
| **Expansion Ratio [-]** | 1.53 |
| **Number of layers [-]** | 7 |

A first estimation of the boundary layer thickness is given by the following formula used for a flat plate in case of a turbulent flow [24]:

$$\delta = 0.37 \cdot x \cdot {Re_x}^{-\frac{1}{5}}$$

where $x$ is representative of how much the flow is travelling over the body, in other words it is a reference length which in this case is the diameter, $d$, and $Re_x$ is the Reynolds based on the diameter. Then the value of the first cell layer thickness is chosen by exploiting the open-source utility $y^+$ *calculator* [25] which gives an estimate of the $x_{min}$ for a desired $y^+$. The desired $y^+$ is set to be inside the log-law region, but this depends on the velocity so it changes along the surface, moreover in the vicinity of the stagnation point the flow is slowed down, so the $y^+$ tends to be very low. For this reason, the averaged $y^+$ is considered which in this case is between 30 and 40 depending on the turbulence model, whereas the maximum $y^+$ is below 100, so inside the logarithmic region. The last layer thickness is set such that its dimension is close to that of the first refinement regions, namely Region 4. The AR passing from the first to last cell layer thickness increases from 0.043 to 0.563 (about ten times), thanks to combination between the expansion ratio and the number of layers. In figure 3.13 it is possible to notice the boundary layer growth: the last cell layer has dimensions quite similar to the first refinement region, both in longitudinal and traversal directions.

Four different refinement regions are identified in Figure 3.14 with the aim of having more resolution in the wake to capture turbulent phenomena. The red *Region 4* covers all the body and it it has the highest level of refinement, then moving outwards the mesh becomes coarser.

| **Region** | **1** | **2** | **3** | **4** |
|---|---|---|---|---|
| $\mathbf{X}_{block}$ **[m]** | $16.41 \cdot d$ | $8.00 \cdot d$ | $3.00 \cdot d$ | $0.53 \cdot d$ |
| $\mathbf{Y}_{block}$**[m]** | $17.91 \cdot d$ | $2.98 \cdot d$ | $1.94 \cdot d$ | $0.53 \cdot d$ |
| $\mathbf{Z}_{block}$**[m]** | $7.46 \cdot d$ | $3.57 \cdot d$ | $3.46 \cdot d$ | $3.35 \cdot d$ |
| **Refinement Level** | 4 | 5 | 6 | 7 |
| $\Delta$**s[m]** | $6.250 \cdot 10^{-2}$ | $3.125 \cdot 10^{-2}$ | $1.562 \cdot 10^{-2}$ | $7.812 \cdot 10^{-3}$ |

Table 3.3: Refinement Regions settings of the cylinder

The red *Region 4* has a size cell of $7.8215 \cdot 10^{-3}m$ which means it is very close to the last cell layer thickness $4.40 \cdot 10^{-3}m$ at least in order of magnitude, this makes sense from a numerical point of view to have a gradual refinement among consecutive layers. The mesh becomes coarser as it moves towards the far-field domain, reaching a maximum size of cell of $6.250 \cdot 10^{-2}m$ where the level of refinement is 4. The total number of cells is $5.76 \cdot 10^{6}$ which is quite a large number for relative simple geometry such as this one, however it is worth to recall that it is a 3D mesh. Moreover the gap between the gray *Region 1* and the light blue *Region 2* is generated to study if three-dimensional effects are recognizable at this Reynolds and for this AR. The *checkMesh* OpenFoam utility is executed to check if any problems arise from the mesh generation process. This check went well with the following parameters:

| | |
|---|---|
| **Maximum Non-orthogonality** | 59.60° |
| **Average Non-orthogonality** | 3.790° |
| **Maximum skewness** | 2.022 |
| **Maximum aspect ratio** | 23.00 |

Table 3.4: CheckMesh output

The Maximum Non-orthogonality is lower than 70 and this should be enough to stay inside a safe zone during the solving process. Similarly, the max skewness is much lower than 4, higher values may impair quality (accuracy) of the results and finally, the highest aspect

ratio cells is not a critical value so eventually the stability and the solver convergence should not be affected.

### 3.3.3. Numerical schemes

The schemes used for all the turbulence models are mostly second order accurate to achieve a better agreement with the reference solution at the expenses of the stability. The problem is unsteady and the second order implicit *backward* scheme is used for discretizing the time derivatives. For the gradients the *Gauss linear* is used, as well as for the divergence schemes, but for the the *advection velocity*[1] term, i.e. $div(\phi, U)$, where a *linearUpwind* is used. This scheme requires the discretization of the velocity gradient to be specified and it is upwind-biased, so it could act as a first order scheme in regions of high gradients to avoid numerical instabilities, otherwise it behaves mainly as a second order one. As interpolation schemes the default *linear* scheme is set to interpolate values from cell centers to face centers. For the Laplacian terms the recommended *Gauss linear corrected* scheme is used. Finally, as surface normal gradient schemes and wall distance calculation methods are respectively set to be *corrected* and *meshWave*. The specific divergence schemes for all the turbulence models are set to be always the second order accurate, i.e. for $div(\phi, \widetilde{\nu})$, $div(\phi, \kappa)$, $div(\phi, \omega)$ and $div(\phi, \epsilon)$.

[1] $\phi$ stands for the volumetric flux of velocity on the cell faces

## 3.4. Results

Once the simulations are performed, the first thing to be checked is the flow-field: a visualization of both streamlines and velocity distribution at the center-line location is proposed.

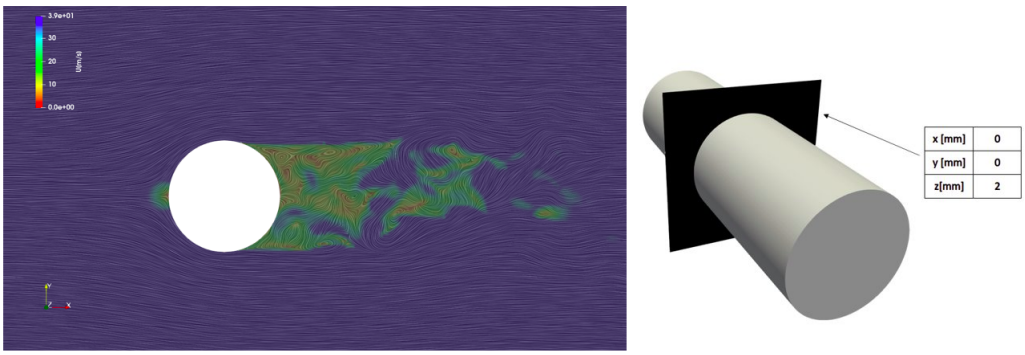


Figure 3.15: Streamlines visualization combined with the velocity field

This visualization is taken at a plane that cuts the cylinder into two equal halves. All the measurements and flow quantities are evaluated at this location so from this point of view is a 2D simulation even if the mesh is 3D. This is done to replicate the way the measures were taken during the experiment and so to perform a reasonable model validation.
In Figure 3.15, the impinging flow generates a small low pressure region upstream the cylinder, then the fluid particles are accelerated and slowed down up to the separation point, where the gradient of velocity is zero. At this location a recirculating region is generated and part of the pressure is recovered in the wake. The wake is characterized by different vortices, some of them are present at several diameters far from the cylinder and the regime is fully turbulent as expected for this problem at this Reynolds.

### 3.4.1. Model validation: $C_p$ distributions, $C_D$ and $\theta$

The static pressure coefficient values are the core of the following model validation. The $C_p$ are plotted with the experimental one, against the angle $\theta$ which is considered positive clockwise and it goes from 0° to 180°. The $C_p$ is averaged from 0.08 s to 0.12 s since the convergence is reached.

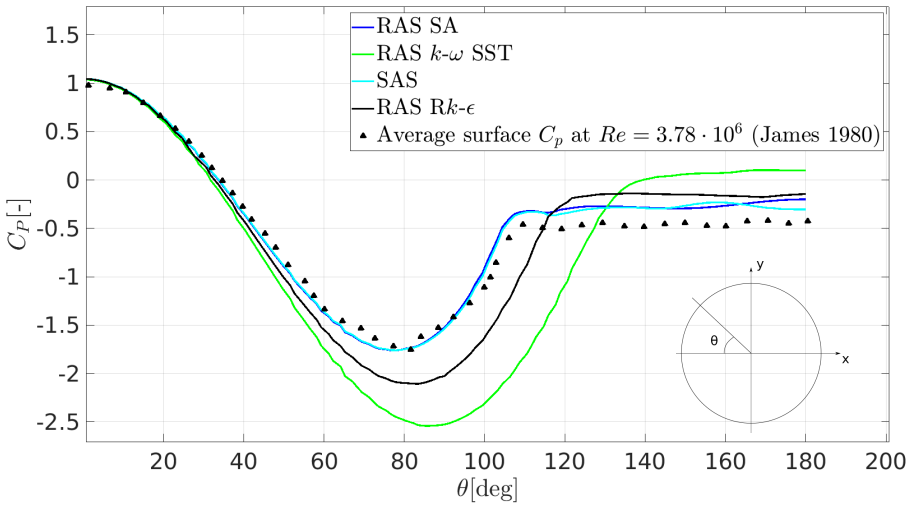


Figure 3.16: Evolution of the $C_p$ on the surface of the cylinder for different RAS

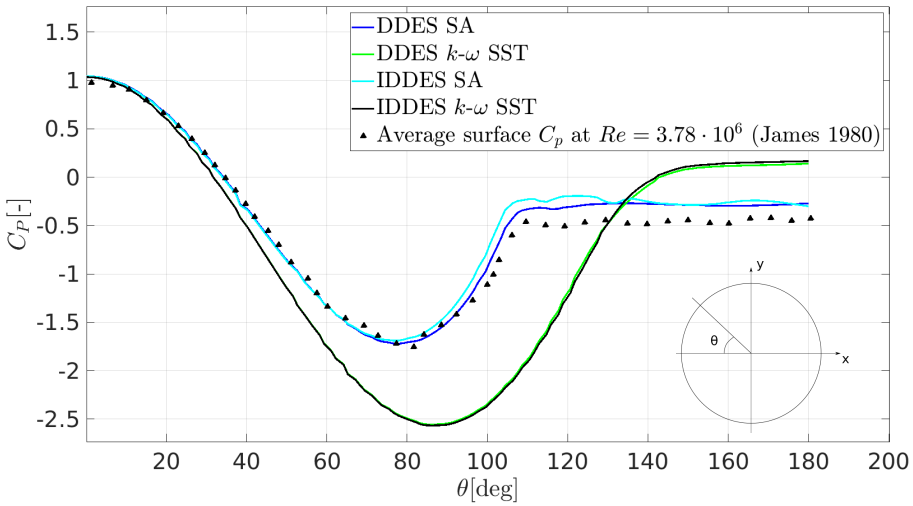


Figure 3.17: Evolution of the $C_p$ on the surface of the cylinder for different DDES

It is possible to notice that the SA and SAS models better agree with the experiments: the pressure is 1 at the stagnation point, the it decreases in the accelerated flow region reaching a value lower than -1.5 and then it is recovered again in the wake where it

becomes almost constant and its value is a bit overestimated. For what concerns the $\kappa - SST$ and $\kappa - \epsilon$ models there are some problems: the minima are underestimated and the pressure in the wake is clearly overestimated, so further investigations are needed on those turbulence models. Similarly, the DDES follows the same trends of RAS: the SA models confirm to follow the very same experimental distribution with improvements, since the pressure in the wake is closer to the experimental data, whilst the $\kappa - SST$ once again are far from the experiments.

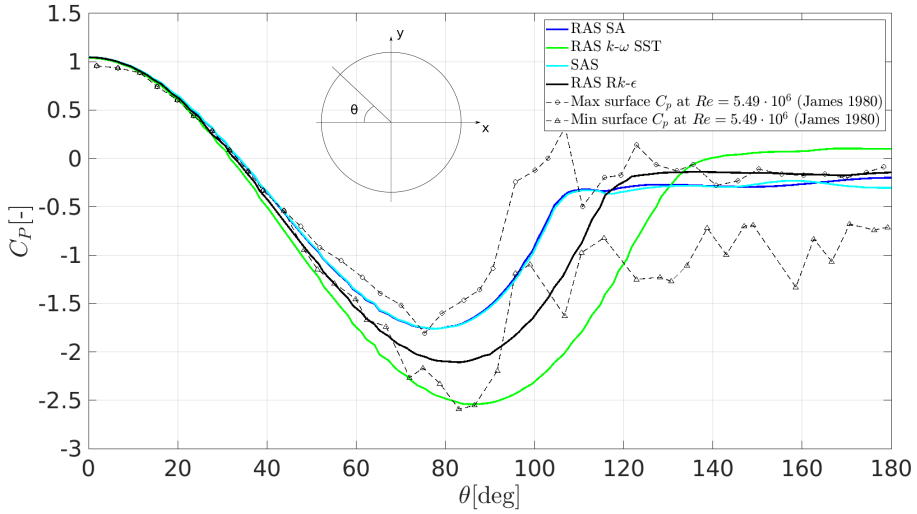


Figure 3.18: Comparison of the $C_p$ on the surface of the cylinder models with the experimental $C_p$ minima and maxima for different RAS

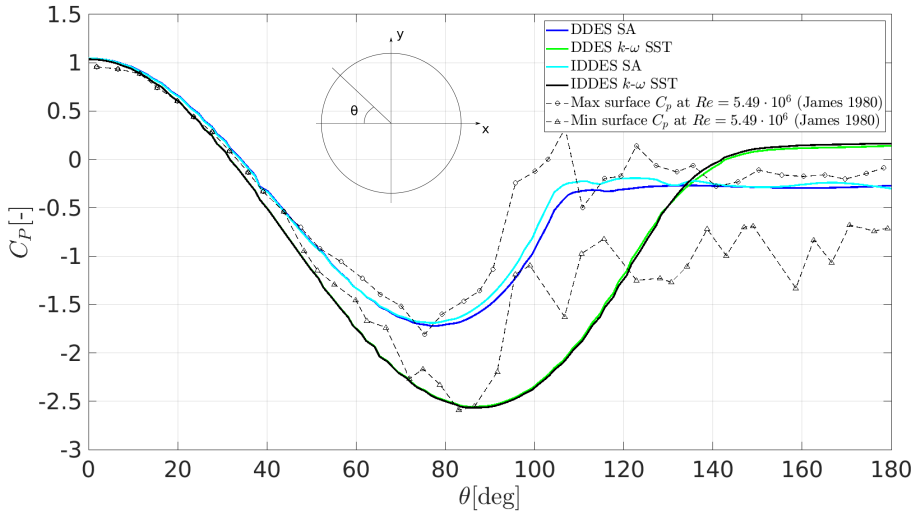


Figure 3.19: Comparison of the $C_p$ on the surface of the cylinder models with the experimental $C_p$ minima and maxima for different DDES

Another interesting analysis involves the instantaneous minima and maxima $C_p$ measured during the James' experiments[19]. The values are available at a Reynolds greater than the one considered for the simulation, however it gives a qualitative range inside which the data coming from the simulations should be. The SA models both for RAS and DDES formulation are still inside the proposed range, whilst the $\kappa - \epsilon$ is at the range limit and the $\kappa - \omega$ is even outside this range. Finally, a more detailed study on the causes of this errors is strictly necessary.
At this point, the validation is enriched with the drag coefficient and the wall shear stress distributions in terms of separation angle. It is worth to recall that drag should be inside a experimental range that goes from 0.35 to 0.49, so the values should be around 0.40, whereas the $\theta_{exp.} \approx 106.0°$.

| **Turbulence Models** | **C$_D$[-]** | $\theta$ [°] |
|---|---|---|
| **RAS**$_{SA}$ | 0.3873 | 107.51 |
| **RAS**$_{\kappa-\omega SST}$ | 0.2506 | 134.00 |
| **SAS**$_{\kappa-\omega SST}$ | 0.4037 | 107.50 |
| **RAS**$_{R\kappa-\epsilon}$ | 0.2938 | 117.70 |
| **DDES**$_{SA}$ | 0.4081 | 107.50 |
| **DDES**$_{\kappa-\omega SST}$ | 0.2359 | 142.60 |
| **IDDES**$_{SA}$ | 0.4204 | 106.34 |
| **IDDES**$_{\kappa-\omega SST}$ | 0.2254 | 135.90 |

Table 3.5: Mean drag coefficient and separation angle

The drag coefficients estimated by the $SA$ and $SAS$ are all inside the proposed experimental range, whilst the separation angle $\theta$ is closer to experimental one, in particular for the $DDES_{SA}$ and $IDDES_{SA}$ models. The $\kappa - \omega SST$ and $R\kappa - \epsilon$ models are still far from the experiments both in terms of drag and separation angle, so there is something wrong inside these simulations that needs further investigations. Passing from DDES to IDDES, for the same turbulence model, the separation angle increases, this is already a signal of premature separation for IDDES.

### 3.4.2. Convergence and stability

The solution is studied also in terms of numerical stability: the residuals of pressure and velocities are plotted in time, as well as the convergence of the forces is analyzed.

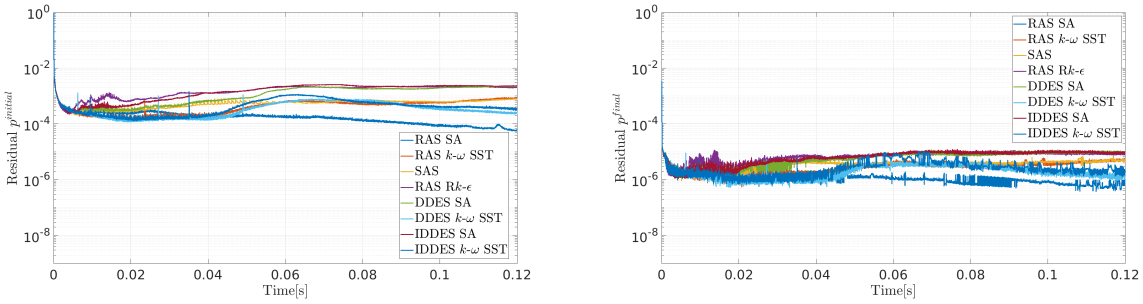


Figure 3.20: Residuals of pressure vs.Time

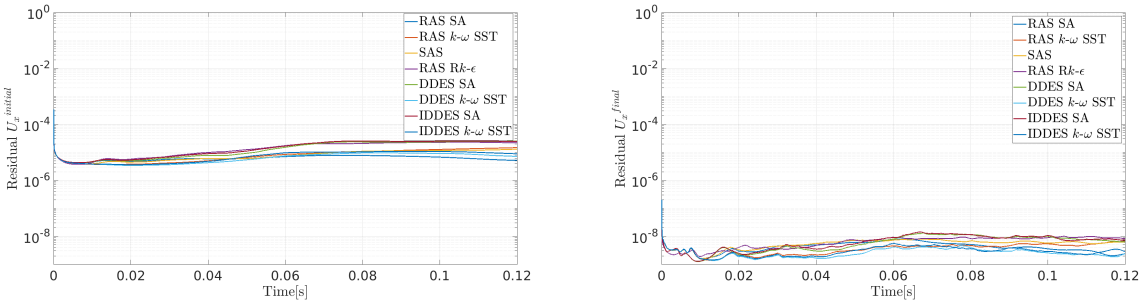


Figure 3.21: Residuals of $u_x$ vs. Time

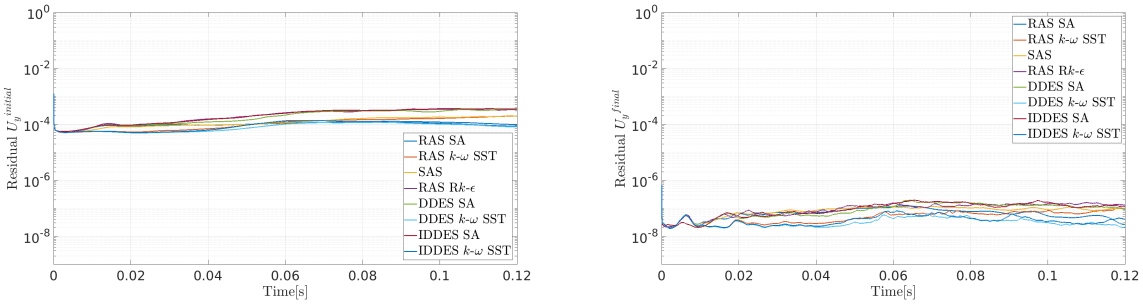


Figure 3.22: Residuals of $u_y$ vs. Time

All the residuals, initial and final, from pressure (Figure 3.20) to velocity (Figures 3.21 and 3.22) are decreasing of several orders of magnitude, from $10^{-2}$ up to $10^{-9}$, this means that at least from a numerical point of view the equations are converging. This is also confirmed by the output .log file where the convergence at each time step is reached always within three or four outer iterations, but at the very beginning of the simulations where five iterations are needed. This is an important point since it confirms that the number of outer corrector allows to achieve the imposed tolerance.

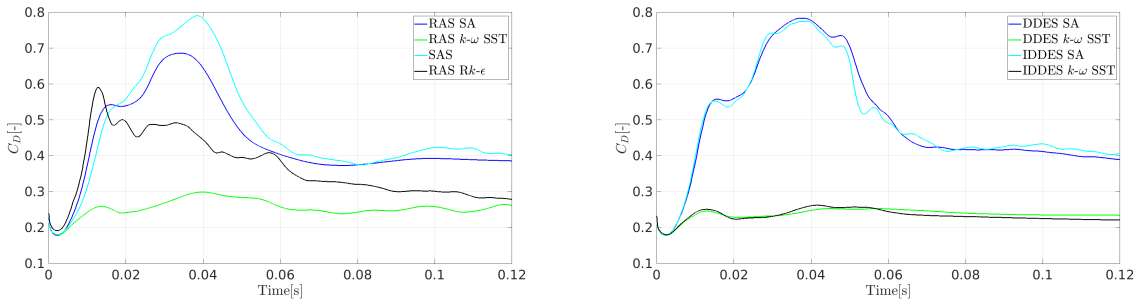


Figure 3.23: Drag coefficient vs. Time for different RAS and DES models

In Figure 3.23, the drag oscillations reduce after half of the simulation time and the time average is considered to be valid after 0.08 seconds. Finally, it is necessary to recall that at this critical Reynolds, a sort of re-establishment of vortex street could occur even if with much more oscillations for obvious reasons, so this could be eventually the reason behind the fact that the drag is not perfectly constant at convergence. The averaged Courant number is always below 0.2(<1) for all the simulations.

### 3.4.3. Eddy viscosity visualizations

To analyze if the model is properly solving the RAS and LES regions, the *DES model region* OpenFoam utility is exploited.

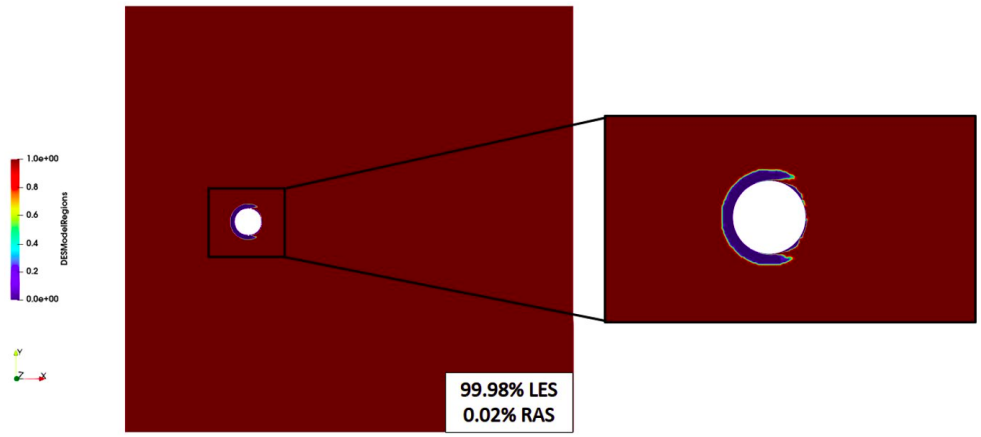


Figure 3.24: DES Regions: $\text{DDES}_{SA}$

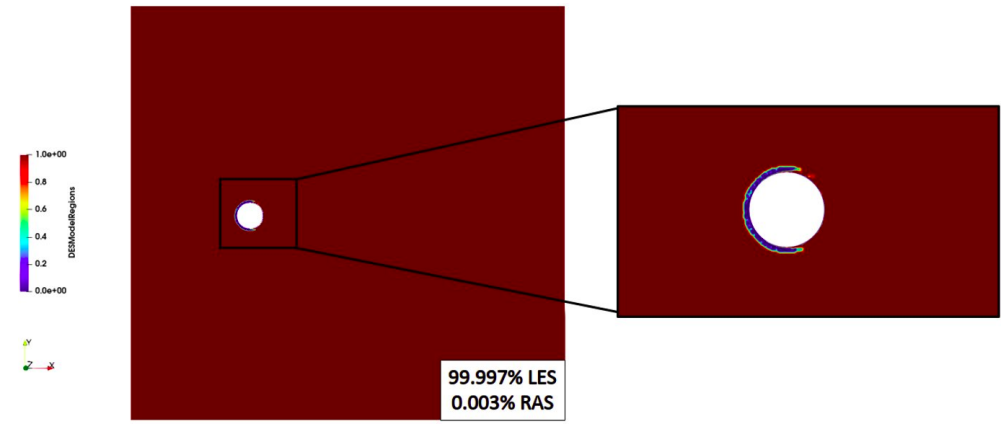


Figure 3.25: DES Regions: IDDES$_{SA}$

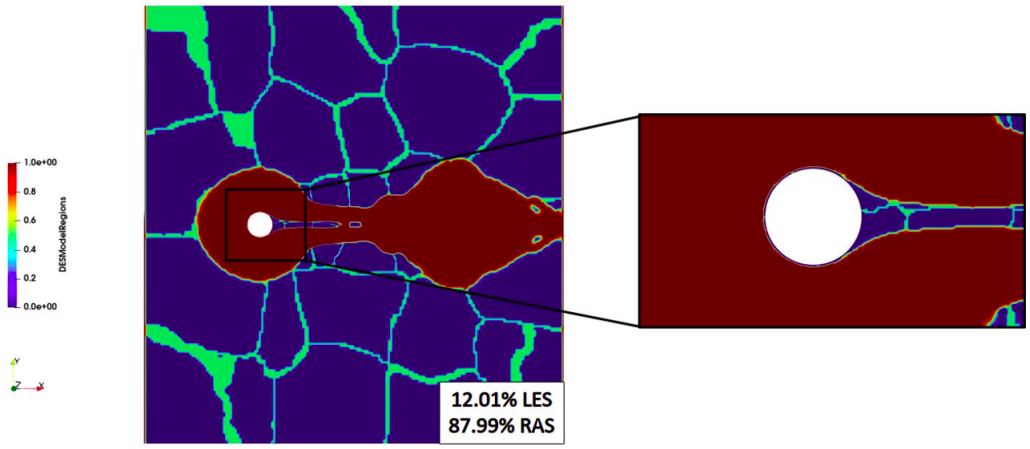


Figure 3.26: DES Regions: DDES$_{\kappa-\omega SST}$

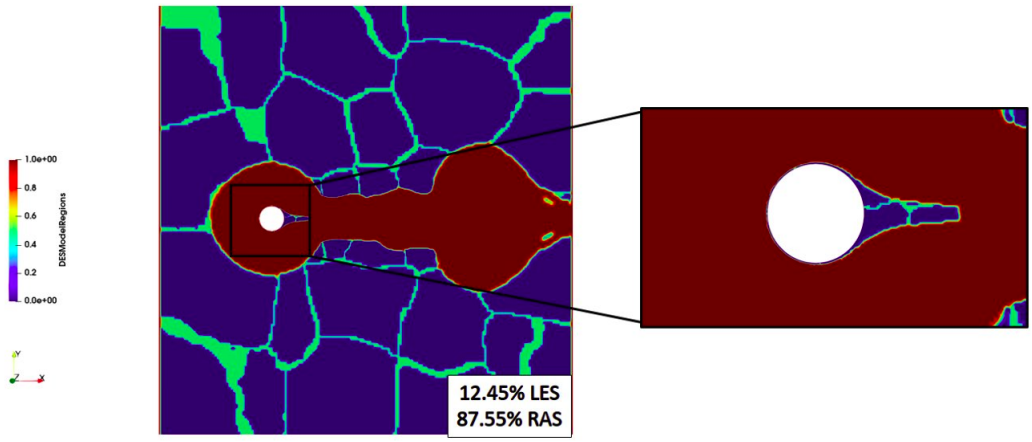


Figure 3.27: DES Regions: IDDES$_{\kappa-\omega SST}$

It can be noticed that LES are activated correctly for the SA models both in DDES (Figure 3.24) and IDDES (Figure 3.25), in fact RANS are just present close to the wall,

respectively the 0.02% and the 0.003% of the flow is solved with RANS, then far from the flow is fully solved by means of a LES. This behaviour is typical of a DES formulation and it should be applicable to all the turbulence models. However, this is not valid in the $\kappa - \omega SST$ models for such study: RAS are activated both in the wake and far away from the cylinder with a prevalence of them ($\approx 87\%$) with respect to LES; this could be potentially one of the errors in the solution. So it is important to study how the blending functions works and what are the main and governing quantities that could affect the flowfield. The switch in the gray region is governed by different flow quantities, the eddy viscosity $\nu_t$ is one of them and the blending function depends linearly from it. Eventually a wrong $\nu_t$ distribution could lead to errors in the solution.

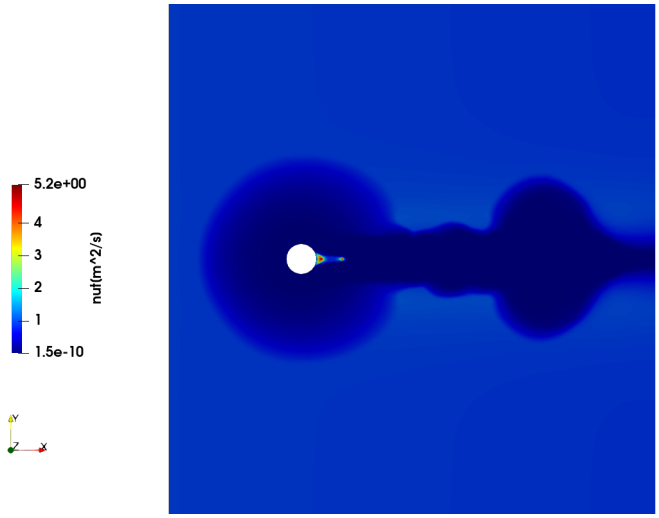


Figure 3.28: $\nu_t$ distribution for IDDES$_{\kappa-\omega SST}$

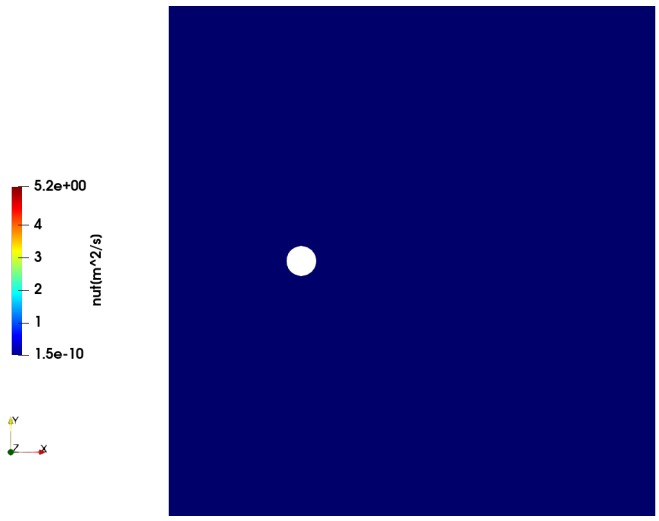


Figure 3.29: $\nu_t$ distribution for IDDES$_{SA}$

The expected distribution of the eddy viscosity should the one represented in Figure 3.29:

its value should be low everywhere, in particular in the farfield domain where the flow is not affected significantly by the body. Nevertheless, the $\nu_t$ varies a lot among all the models: looking at Figure 3.28, it is possible to notice a region close to the cylinder where the eddy viscosity is low, then it increases again reaching much higher values. By comparing these regions with the previous ones where the DES regions are shown, it is possible to notice that they are very similar, so the problem could be blamed to the $\nu_t$. The reasons behind this *non-physical* behaviour could be many: the far-field mesh could be too coarse for such a problem where the $\epsilon$-*cells* are solved and this could lead to an overestimation of the eddy viscosity, furthermore for a reasonable comparison the same mesh is used among all the turbulence models and from RAS to DES, this could generate mesh more appropriate for a case rather than another one. In fact, the mesh is chosen in order to have a $y^+$ inside the log-law region, this is a strong assumption that admits in advance an error in the velocity profile reconstruction, moreover in literature is known that $\kappa - \omega SST$ models works better inside the viscous sub-layer where the $y^+$ is lower than 1. An over-estimate of the eddy viscosity leads to an overestimate of the wall shear stress and so also of the forces acting on the cylinder. A finer mesh resolution could be required for $\kappa - \omega SST$.

## 3.5. The new subset of turbulence models

The turbulence models that resulted to be more appropriate for such problem are the DDES$_{SA}$ and IDDES$_{SA}$: they gave results more in agreement with the experiments both in terms of the evolution of the pressure along the surface and aerodynamics forces. The other tested methods, particularly the $\kappa - \omega$ SST, fail to solve the flow around the cylinder: the pressure distributions are far from the reference mean values, but also out of the range of instantaneous minima and maxima identified during the James' experiments[19]. The analysis is thus focused on the causes of these problems which could be the incorrect activation of the blending function in the computational domain. This could relies on the overestimation of the eddy viscosity which, in turn, it could be due to the type of mesh. The resolutions could not be fine enough to solve turbulent flow downstream the cylinder, especially in the wake. For those models, LES are activated just in the regions close to the cylinder, but then RAS are used for most of the domain, this could generate errors during the solving process and so in the results.
Finally, this new subset of turbulence models are used for the numerical simulations of the DrivAer. However, in literature it is known that the $\kappa - \omega SST$ model could works fine for such purpose, so along with DDES$_{SA}$ and IDDES$_{SA}$, the IDDES$_{\kappa-\omega SST}$ is going to be tested.

# 4 | Turbulent flow around the DrivAer

## 4.1. Summary

The new subset of turbulence models is tested on the DrivAer automotive body. The outlook of this investigation is to highlight the main characteristics of the turbulence models and how they affect the flowfield around the car. To do so, the models are compared first with experiments to validate the work and then among each others. The comparisons are performed from different points of view: from aerodynamics coefficients to pressure and velocity visualizations. Different planes are used for the visualizations purposes to focus more on the wake of the car and of the wheels. Three meshes are also generated to prove that results are grid-independent. At the end, some interesting flow visualizations are proposed to show strong and weak points of each model and to point out how much the turbulence modeling approximation is affecting the flow.

## 4.2. Case study

This investigation is intended to study a car model at constant speed. The Reynolds number is $11 \cdot 10^6$, the problem is three-dimensional and it is qualitatively represented by the following:

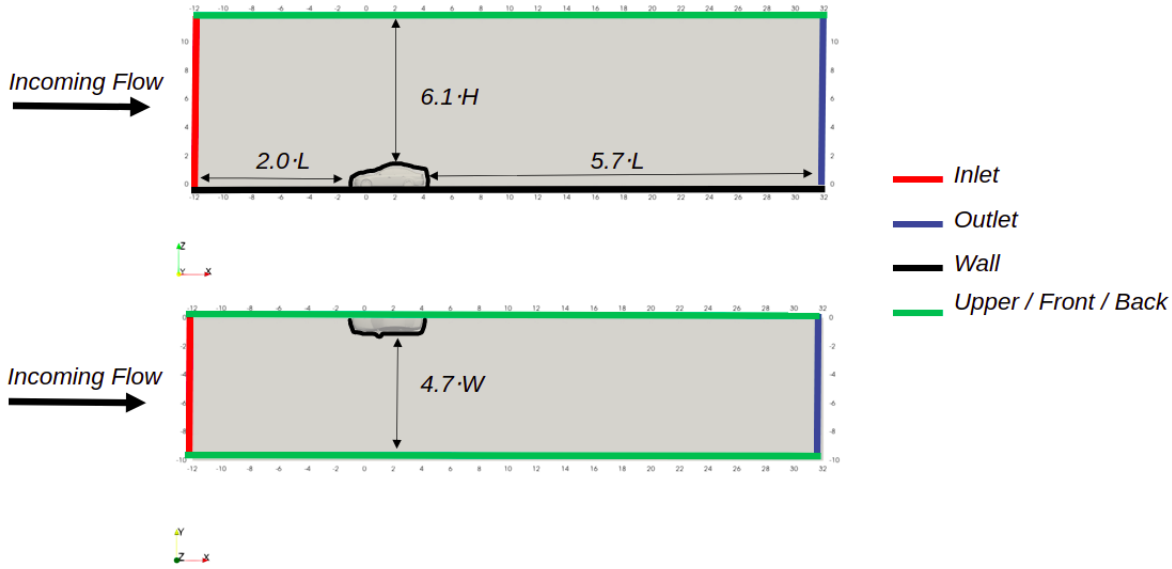


Figure 4.1: Problem setup: DrivAer car in a uniform flow

| | Inlet | Outlet | Upper / Front / Back | Wall |
|---|---|---|---|---|
| **u** [$\mathrm{m\,s^{-1}}$] | 38.89 | *inletOutlet* | *symmetry* | *fixedValue* |
| **p** [Pa] | *zeroGradient* | 0 | *symmetry* | *zeroGradient* |

Table 4.1: Velocity and pressure boundary conditions for the DrivAer

For computational limits, the car has a smooth underbody and it is just studied the flow over the body, so the cooling systems as well as the flow through inner portion of the vehicle are not taken into account, the rim are fully closed and the tyres have four longitudinal groves. The simulations are performed for an *open-road* case, since not so much informations about the wind tunnel testing are known in the papers used for the model validation. This working condition is actually a real working situations for a car that proceeds forward at a fixed velocity in a highway.
This DrivAer model has not suspensions and brakes, and the tyres and the rims are decoupled in order to generate a more appropriate mesh in those critical regions. The

specific boundary conditions are very similar to what already mentioned for the cylinder test case, the difference, beside the geometry, is one of the planes, i.e. the black one represented in Figure 4.1 that is considered as a wall, since it is representative of the street.

### 4.2.1. Literature Review

During the last years, a lot of experiments and numerical validations have been performed for the DrivAer car and more recently new advanced features are added to the standard vehicle, such as a detailed underbody, engine bay, gear box, pipes and cooling systems. Three main references have been considered and all of them are crucial to achieve reliable simulations as well as the model validation itself.
One of the most recent references is the one of Hupertz et al. [2]. He considered a detailed geometry which is represented by the following figures:

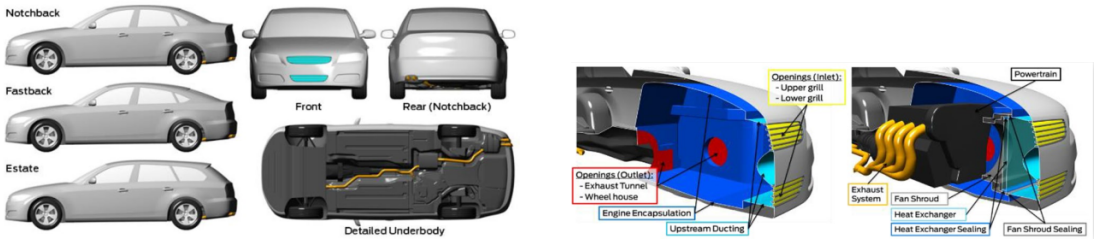


(a) Exterior geometry (b) Under-hood of the Open Cooling car

Figure 4.2: Detailed Ford DrivAer geometry [2]

He studied different car geometry and configurations, in particular the open and closed cooling cases. The model is tested inside the Pinrinfarina Wind tunnel which has an open test section and boundary layer and tangential velocity suctions systems to make the inlet flow as much uniform as possible. The experiments are performed at $Re \approx 11{\cdot}10^6$. The car is equipped by 295 probes distributed uniformly along the vehicle surface to measure the pressure distributions. The wheels are not rotating. Aerodynamics forces are available, as well as flow field measurements at three different cross-sections in the vicinity of the model. Even more interesting results have been presented during the Ford workshop [3] at which Burkhard Hupertz and other 65 participants contribute with their own data. During that presentation a big amount of data has been shown and shared with a large variety of solvers, software, meshes and turbulence methods. In this sense, the seminar[3] and the specific paper [2] are used for both validate the model and present results in a clear and complete way: from aerodynamic coefficient to pressure distributions involving various car features (underbody and hood leading edges, underbody and upperbody center-line

distributions, C-pillars and wake velocity profile at different cross sectional planes) and, finally, the flowfield visualizations (mirrors, windows, pillars, wheel's wakes distributions). The second paper by Wieser et al. [26] is used to understand which type of comparisons have to be made for the flow visualizations.

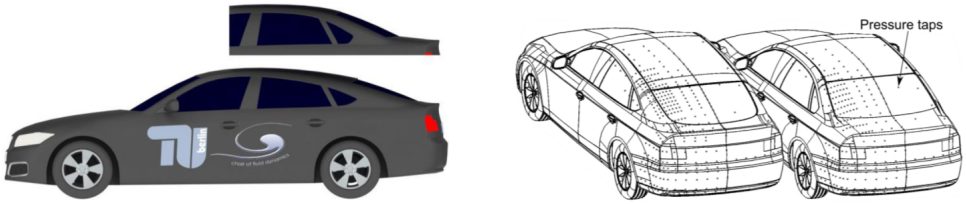


(a) Notchback (top) and fastback (bottom)

(b) Pressure taps distributions

Figure 4.3: DrivAer geometries used for Wieser's experiments [26]

The experiments have been performed at $Re = 3.2 \cdot 10^6$ with a 25%-scaled model. The car is tested inside the closed-loop wind tunnel at the Institute of Fluid Dynamics and Technical Acoustics at the "Technische Universität Berlin" with a close test section. Two different configurations are tested, i.e. the notchback and the fastback ones. The DrivAer model is very similar to the one used for this study: it has a smooth underbody with non-rotating wheels, the tyres have four longitudinal groves with a five spoke-rim mounted on it. The car lies on a turning splitting plate which can be rotated to change the yaw angle and study specific side wind conditions. An internal six component force balance is located in the inner DrivAer-model and connects the mounting strut and the inner DrivAer-mounting plate to measure the aerodynamics attitude of the vehicle. Furthermore the car is equipped by 211 pressure taps as it is shown in Figure 4.3.

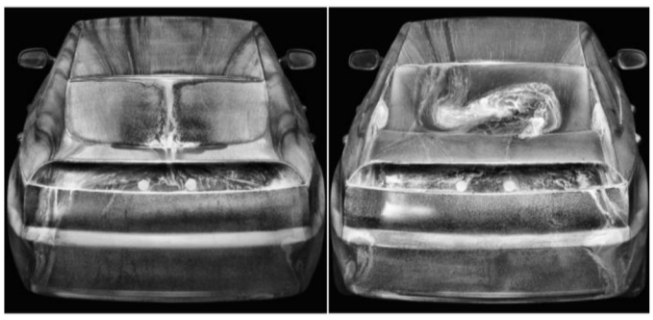

Figure 4.4: Paint visualizations[26]: fastback(one the left) and notchback(on the right)

Beside the pressure visualizations and the availability of the aerodynamics coefficients, some other interesting paint visualizations are presented: these types of visualizations are performed by means of an oil-based white paint mixed with petroleum which are

deposited on the notchback and fastback bodies where the separation occurs; once the wind tunnel is turned on, the flow moves the paint and the surface traces are recorded with a reflex camera which allows to identify the main vortices over the car. It can be noticed in Figure 4.4 that the flow is symmetrical for the fastback configuration, but it is not on the notchback body. This is a strange behaviour since the car configurations are symmetrical with respect to the center-line plane. The notchback car experiences a massive asymmetrical recirculating bubble even if this specific visualization is performed at zero yaw angle: it is a strange behaviour which could rely on the different C-pillar design. This second reference was considered as reference for the model validation since the geometry was very similar to the one used for the simulations, however the Reynolds involved is lower than the one used by Hupertz.
The third and last paper is by Ashton and Revell [4] in which the authors try to have a similar approach to the one presented in this thesis but with different turbulence models and with a fastback car configuration.

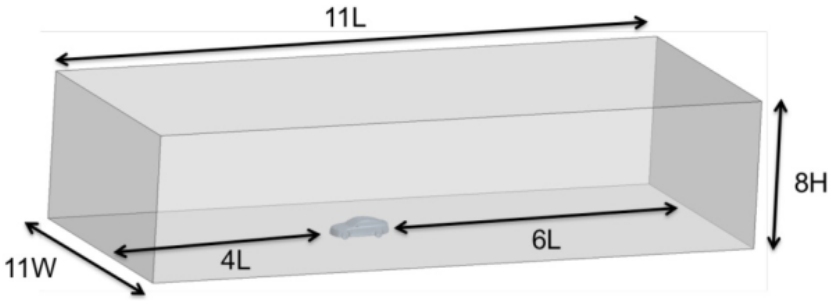


Figure 4.5: Neil's computational domain [4]

This is a reference paper at least for building the computational domain: in fact, a similar domain size is used by considering all the dimensions normalized with respect to the car dimensions as shown in Figure 4.5. They tested RAS and DES turbulence models, performing also grid convergences for few simulations. In this sense, the required computational resources is very high: they exploited different meshes from $18 \cdot 10^6$ up to $300 \cdot 10^6$ cells. During this work, the same computational domain is used and similarly the grid convergence is proposed with some DES models and achieving good results, as well.

### 4.2.2. Reference solution

The model validation is performed first by means of the lift and drag coefficients for which experimental values are given by Hupertz et al. [2]:

| | **Tests (2021)** |
|---|---|
| $C_D[-]$ | 0.255 |
| $C_L[-]$ | 0.087 |

Table 4.2: References values of the DrivAer's experiments

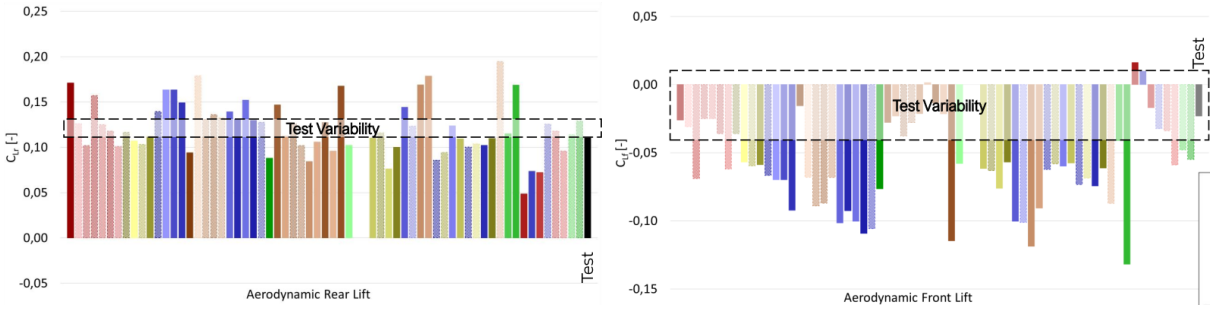


Figure 4.6: Front, Rear lift coefficients and test variability region [3]

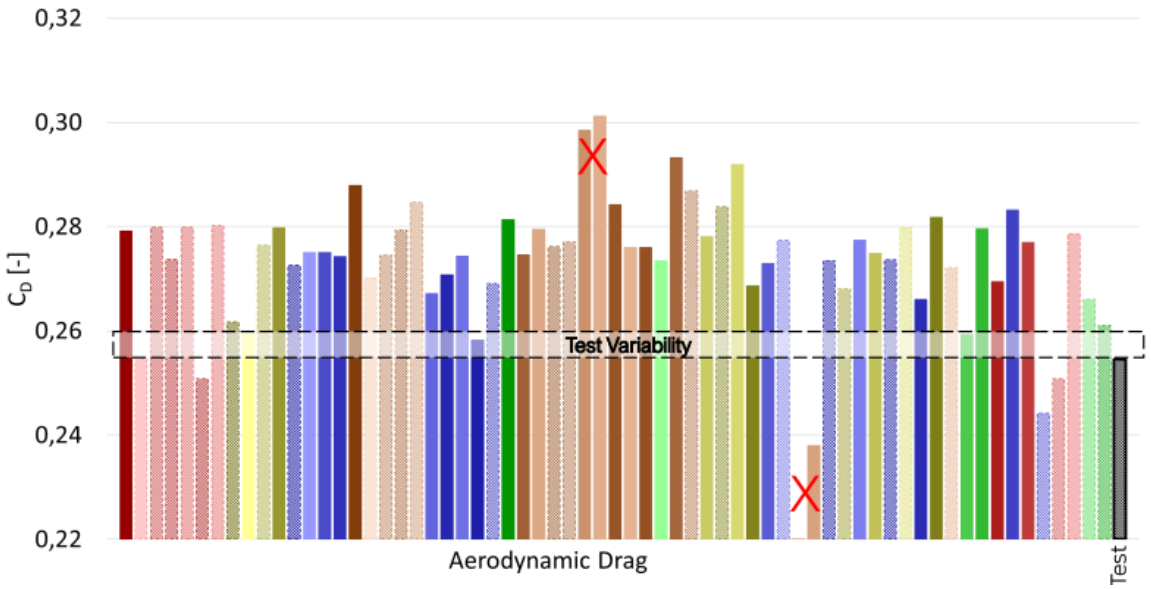


Figure 4.7: Drag coefficients and test variability region [3]

Along with the experiments, different numerical simulations have been performed [3] and they highlighted some deviations with respect to the wind tunnel tests. For this reason,

the results of this study are first compared with the experiments, but also with the trends identified by the CFD data shown in the Figures 4.6 and 4.7.

## 4.3. Methodology

The solver pimpleFoam is used and it allows to solve incompressible and transient problems. The tested turbulence models are the DDES$_{SA}$, IDDES$_{SA}$ and the IDDES$_{\kappa-\omega SST}$, so the relative entries for the turbulent kinetic energy and the modified eddy viscosity have to be specified in the *0/* directory.
The same equations settings are used, in particular, the number of outer correctors is 3, so this is the maximum value for which the momentum and pressure equations are iteratively solved, whilst the number of correctors is 2, which means that up to twice the pressure equation can be solved during each outer iteration. The tolerances for all the equations (momentum, pressure or other specific equations) are set to $1 \cdot 10^{-6}$ , moreover the associated potential flow problem is solved before the real case to have better values for the problem initialization. During the first iterations, the pressure and the velocity oscillate a lot, so an under-relaxation factor is applied on the first outer iterations of 0.7 for the pressure and the momentum equations, however on the last outer iteration, no under-relaxation factors are considered.
The simulations make use of wall functions for computational limits, so the condition of ${y^+}_{average} > 30$ is fulfilled over all the surfaces.

### 4.3.1. Computational model

Before going through the mesh specifications, it is necessary to specify that the symmetry is exploited for limited computational resources, so the studied case is on *half* of the actual domain, in this sense just half of the car is considered ed the same goes for the internal mesh of the blockMesh which is created accordingly.

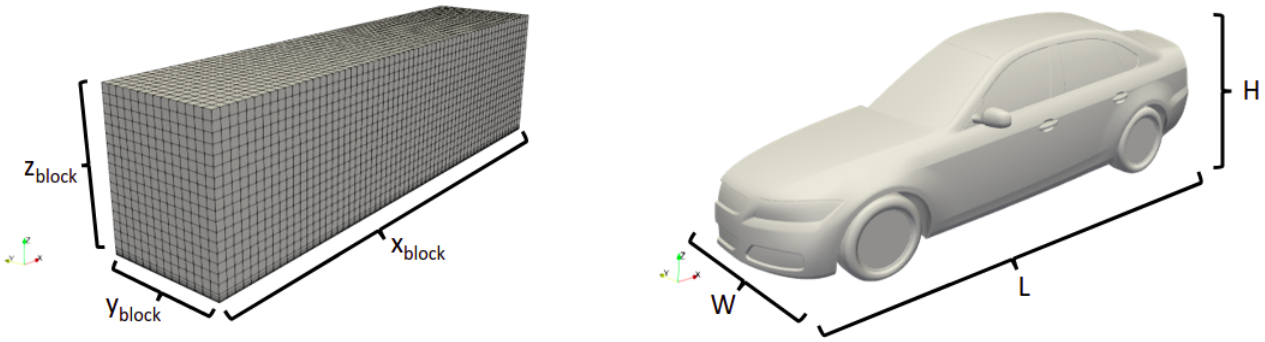


Figure 4.8: BlockMesh and car mesh

The AR in BlockMesh is defined as the ratio of the number of cells along a spacial direction and its relative length (e.g. $X_{block}$, $Y_{block}$ and $Z_{block}$ defined in Figure 4.8). Since the snappyHexMesh utility works fine for AR lower than 1, in this case it is set to 0.7.

| | Value[m] | Normalized Value[-] | Number of blocks[-] |
|---|---|---|---|
| $\mathbf{X}_{block}$ | 44 | **9.0**·$L$ | 63 |
| $\mathbf{Y}_{block}$ | 10 | **4.8**·$W$ | 14 |
| $\mathbf{Z}_{block}$ | 12 | **8.6**·$H$ | 17 |
| **H** | 1.40 | / | / |
| **L** | 4.90 | / | / |
| **W** | 2.10 | / | / |

Table 4.3: DrivAer's mesh settings

The frontal area of the notchback DrivAer is $\approx 2.36m^2$ at which correspond $1.18m^2$ for half of it, it is higher with respect to the standard $2.17m^2$ due to the vehicle scaling, so it has been re-computed for this study. The inlet area is generated such that the blockage ratio is $\approx 0.9\%$ which is an almost irrelevant factor that allows not to consider theoretical corrections on the incoming flow. The car is placed at 12 meters far from the inlet, so

there are more than 27 meters of domain downstream the car to focus on the wake's developments and perform eventually studies on it.
The time step is fixed and set to be $\Delta t = 2 \cdot 10^{-4} s$, whilst the simulated time is $T = 1.6 s$ which is 1.5 times the time the inlet flow takes to reach the outlet of the domain. However, these two quantities are going to be objects of investigations in terms of CFL conditions and numerical convergence.

### 4.3.2. Boundary layer mesh

Based on the surface level and refinement regions, the boundary layer mesh is generated accordingly, covering more or less surfaces depending on the layer extraction. It is important to highlight the boundary layer coverage for each surfaces and some of the main parameters that describe the mesh.

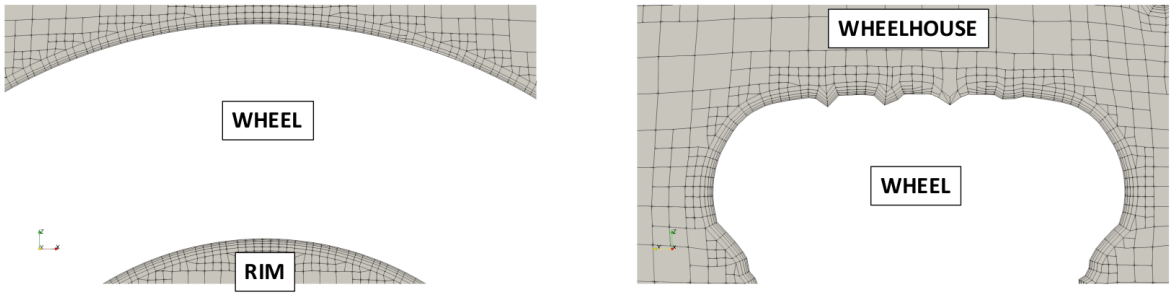


Figure 4.9: Boundary layers of the wheels

| | $\Delta s_{surface}[m]$ | $\Delta s_{initial}[m]$ | $\Delta s_{final}[m]$ | $AR_{initial}[-]$ | $AR_{final}[-]$ | $\%B.L.[-]$ |
|---|---|---|---|---|---|---|
| **Tyres** | $5.468 \cdot 10^{-3}$ | $7.116 \cdot 10^{-4}$ | $2.734 \cdot 10^{-3}$ | 0.13 | 0.50 | $\approx 89\%$ |
| **Intakes** | = | = | = | = | = | $\approx 95\%$ |
| **Lights** | = | = | = | = | = | $\approx 100\%$ |
| **Rims** | = | = | = | = | = | $\approx 100\%$ |

Table 4.4: Boundary layers of the wheels settings

The $\Delta s_{surface}$ indicates the level of refinement of the surfaces which in this case for the presented four patches is the same. Then the $\Delta s_{initial}$ and $\Delta s_{final}$ mean the thickness respectively of the first and last layers at which correspond the $AR_{initial}$ and $AR_{final}$. Finally the $\%B.L.$ is the percentage of layers extruded from the specific surfaces. The latter is an important parameter, since it could be representative of some problems during the meshing process. The lowest percentage is obtained for the tyres which are complex

geometries to be simulated and they need a high level of detail. Looking at Figure 4.9, one can notice that in the $yz - plane$(figure on the right) the last groove on the right is not completely extruded, this is due to a low level of refinement which generates a low percentage of layer addition for the groove in the immediate vicinity. Nevertheless, the percentages of the averaged layer extraction is still high and they allow to reach reasonable results. Furthermore the focus is on the flow development on the whole vehicle, not just the wheels, so these values are considered acceptable for the case in study.

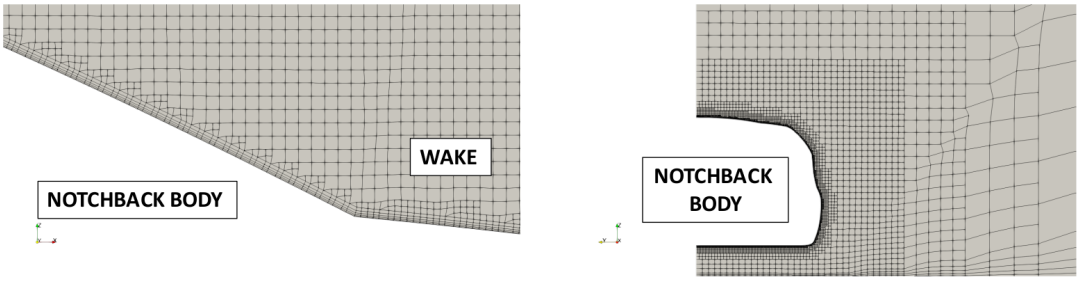


Figure 4.10: Boundary layers of the car

| | $\Delta s_{surface}[m]$ | $\Delta s_{initial}[m]$ | $\Delta s_{final}[m]$ | $AR_{initial}[-]$ | $AR_{final}[-]$ | $\%B.L.[-]$ |
|---|---|---|---|---|---|---|
| **Car body** | $5.468 \cdot 10^{-3}$ | $7.116 \cdot 10^{-4}$ | $2.734 \cdot 10^{-3}$ | 0.13 | 0.50 | $\approx 100\%$ |
| **Notchback** | = | = | = | = | = | $\approx 100\%$ |
| **Underbody** | = | = | = | = | = | $\approx 100\%$ |
| **Mirrors** | $2.734 \cdot 10^{-3}$ | $6.592 \cdot 10^{-4}$ | $1.367 \cdot 10^{-3}$ | 0.24 | 0.50 | $\approx 93\%$ |

Table 4.5: Boundary layers of the car settings

For what concerns the vehicle body, there are not critical points to mention, but the fact that the mirrors are critical geometries that need a high level of surface refinement as it can be noticed in the table. This allows to reach an acceptable value for the boundary layer extraction (93%).

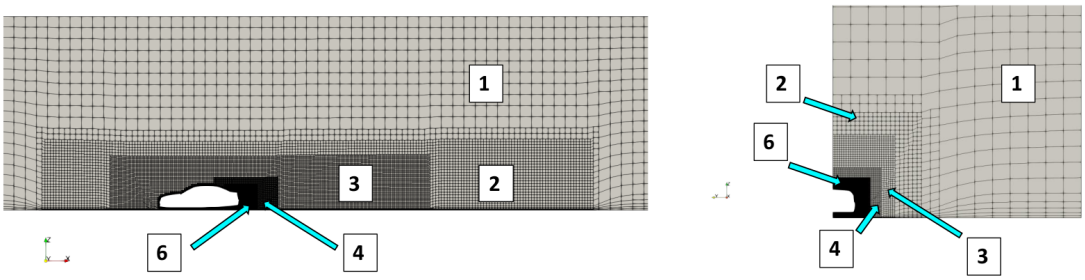


Figure 4.11: Boundary layers of the street

| **Level** | $\Delta s_{surface}[m]$ | $\Delta s_{initial}[m]$ | $\Delta s_{final}[m]$ | $AR_{initial}[-]$ | $AR_{final}[-]$ | $\%B.L.[-]$ |
|---|---|---|---|---|---|---|
| **1** | 0.35 | $4.555 \cdot 10^{-2}$ | 0.175 | 0.13 | 0.50 | $\approx 89\%$ |
| **2** | 0.175 | $2.277 \cdot 10^{-2}$ | $8.750 \cdot 10^{-2}$ | = | = | = |
| **3** | $8.750 \cdot 10^{-2}$ | $1.138 \cdot 10^{-2}$ | $4.375 \cdot 10^{-2}$ | = | = | = |
| **4** | $4.375 \cdot 10^{-2}$ | $5.692 \cdot 10^{-2}$ | $2.187 \cdot 10^{-2}$ | = | = | = |
| **6** | $1.094 \cdot 10^{-2}$ | $1.423 \cdot 10^{-3}$ | $5.469 \cdot 10^{-3}$ | = | = | = |

Table 4.6: Boundary layers of the street settings

The boundary layers are generated by exploiting the option *relativeSize* = *true* which means that the layers thickness are computed with respect to the level of refinement of a specific region. In average the boundary layers of the road is 89% which is quite an acceptable value.
The aspect ratio from the first to the last layer thickness is less of 5 times for almost all surfaces this allows to achieve a gradual transition from the most inner portion of the domain to the outer refinement zones.

### 4.3.3. Refinement regions

At this point several refinements zones are created to solve and focus on regions where flow separations are expected. Those refinement regions become coarser moving far from the vehicle and so approaching to the far-field domain where the thermodynamic conditions are similar to the free-stream ones.

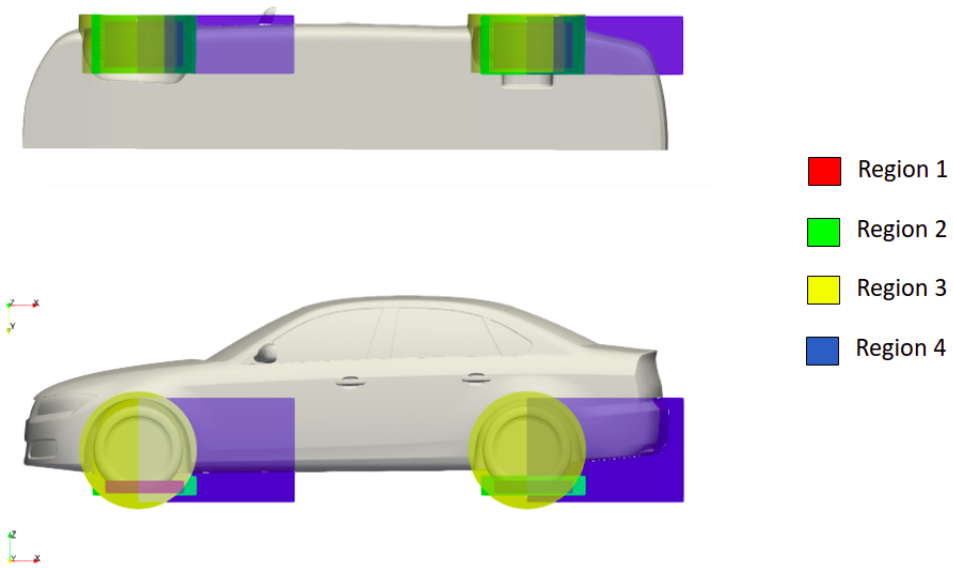


Figure 4.12: Refinement regions at the wheelhouse's location

| **Region** | **1** | **2** | **3** | **4** |
|---|---|---|---|---|
| $\mathbf{X}_{length}$ **[m]** | 0.12·L | 0.16·$L$ | 0.20·$L$ | 0.24·$L$ |
| $\mathbf{Y}_{length}$ **[m]** | 0.2·W | 0.22·$W$ | 0.22·$W$ | 0.22·$W$ |
| $\mathbf{Z}_{length}$ **[m]** | 0.06·H | 0.10·H | 0.60·H | 0.60·H |
| **Level [-]** | 7 | 6 | 5 | 5 |
| **$\Delta$s [m]** | $5.468 \cdot 10^{-3}$ | $1.093 \cdot 10^{-2}$ | $2.187 \cdot 10^{-2}$ | $2.187 \cdot 10^{-2}$ |

Table 4.7: Sizes and levels of the refinement regions at the wheelhouse's location

The highest level of refinement is at the contact patch: this is a critical region due to the high complex flows that are generated combined with tyre deformation and eventually wheel rotation. At *Region 1* the minimum cell size is achieved, i.e. $\Delta s = 5.468 \cdot 10^{-3} m$. Then a larger box in correspondence of the contact patch is created, but with a coarser level of refinement, not to have an abrupt change in the cell dimensions. Another geometry is then created which covers all the wheel and the wheelhouse regions with a lower level of refinement at which correspond a cell size of $\Delta s = 2.187 \cdot 10^{-3} m$ and, finally, the same

refinement is kept for the region downstream the wheel to capture the wake and so the vortices detached from the wheel. This kind of refinements are the same for the front and the back wheels.
Moving on the upper body, the emphasis in on what happens on the C-pillar, namely the flow generated by the notchback body, so two large refinement regions are created to focus on the rear wake of the car.


Figure 4.13: Refinement regions at the notchback body's location

| **Region** | **5** | **6** |
|---|---|---|
| $\mathbf{X}_{length}$ **[m]** | 0.41·L | 0.82·$L$ |
| $\mathbf{Y}_{length}$ **[m]** | 0.43·W | 1.0·$W$ |
| $\mathbf{Z}_{length}$ **[m]** | 1.16·H | 2.32·H |
| **Level [-]** | 6 | 4 |
| **$\Delta$s [m]** | $1.093 \cdot 10^{-3}$ | $4.375 \cdot 10^{-2}$ |

Table 4.8: Sizes and levels of the refinement regions at the notchback body's location

*Region 5* is created just for the separation region on the back of the car and the cell size is of $\Delta s = 1.093 \cdot 10^{-3} m$, whereas *Region 6* covers all the notchback body and so the C-pillar of the DrivAer, but with a coarser grid, in fact $\Delta s = 4.375 \cdot 10^{-2} m$ helping the grid transition towards the farfield mesh.
For what concerns the whole car body, the boundary layer mesh is not enough to generated a smooth transition to the far field domain, so additional layers are needed.

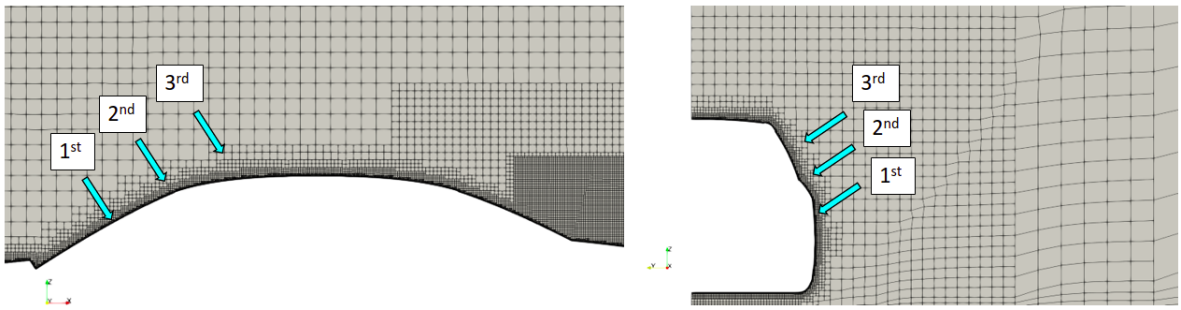


Figure 4.14: Refinement regions of car surface

| **Layer** | $\mathbf{1}^{st}$ | $\mathbf{2}^{nd}$ | $\mathbf{3}^{rd}$ |
|---|---|---|---|
| **Thickness [m]** | 0.05 | 0.10 | 0.15 |
| **Level [-]** | 6 | 5 | 4 |
| **$\Delta$s [m]** | $1.093 \cdot 10^{-2}$ | $2.187 \cdot 10^{-2}$ | $4.375 \cdot 10^{-2}$ |

Table 4.9: Sizes and levels of the refinement regions on the car surface

The layers are added on the overall vehicle's body and in Figure 4.14 it is possible to clearly notice them. In particular three layers are created: the first one has the finest grid which try to matches with the last boundary layer thickness or at least it tries to match the order of magnitude ($10^{-3}$), then the level of refinement decreases up to the level 4 at which corresponds a grid size of $\Delta s = 4.375 \cdot 10^{-2} m$.
The farfield mesh is created with the following specifications.


Figure 4.15: Refinement regions of the open-road

| **Region** | **7** | **8** | **9** |
|---|---|---|---|
| $\mathbf{X}_{length}$ **[m]** | 9.4·L | $7.0 \cdot L$ | $4.1 \cdot L$ |
| $\mathbf{Y}_{length}$ **[m]** | 4.8·W | $1.7 \cdot W$ | $1.2 \cdot W$ |
| $\mathbf{Z}_{length}$ **[m]** | 8.6·H | 3.6·H | 2.9·H |
| **Level [-]** | 1 | 2 | 3 |
| $\Delta$**s [m]** | 0.35 | 0.175 | $8.750 \cdot 10^{-2}$ |

Table 4.10: Sizes and levels of the refinement regions of the open-road

The farfield mesh is for obvious reasons the coarsest in the overall computational domain, however three different refinement regions are created to avoid abrupt changes of the grid which may cause problem during the solving process. Furthermore these regions affect the boundary layer mesh at the bottom of the domain, since the *relativeSize* option is set to *true*, this means that the layer addition is dependent on the level of refinement at that specific location and so it depends on the grid size. On the upper portion of the domain, no boundary layer mesh is created to simulate the case of a car in the open road domain at a constant velocity.

### 4.3.4. Grid resolution

Besides the model validation, this work wants to prove the independence of the of the grid from the results. To this end, a minimum of three meshes must be generated and the differences among each other are going to be presented during this section.

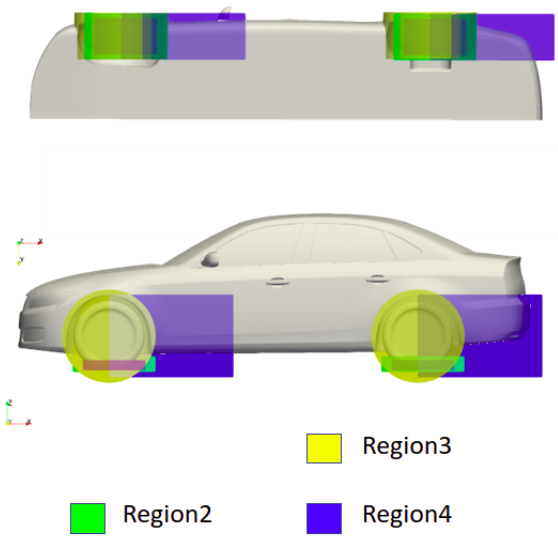


| Coarse Mesh | | |
|---|---|---|
| **Region** | **2** | **3-4** |
| **Level [-]** | 5 | 4 |

| Medium Mesh | | |
|---|---|---|
| **Region** | **2** | **3-4** |
| **Level [-]** | **6** | 4 |

| Fine Mesh | | |
|---|---|---|
| **Region** | **2** | **3-4** |
| **Level [-]** | 6 | **5** |

Table 4.11: Wheel refinements

The level of the outer region of the contact patch, i.e. *Region 2*, is increased passing from the coarse to the medium mesh. In the medium mesh there is not a gradual refinement from the contact patch to the wheelhouse and then for the wake, so this could generated problem during the solving process. This region will be objective of intensive analysis during the post-processing phase. The fine mesh re-establishes a gradual and higher refinement passing from contact patch to the wake of the wheel. The refinements for the regions in the vicinity of the wheels not involve the inner portion of the contact patch for which the level of definition is kept at the maximum since it is the most critical zone.

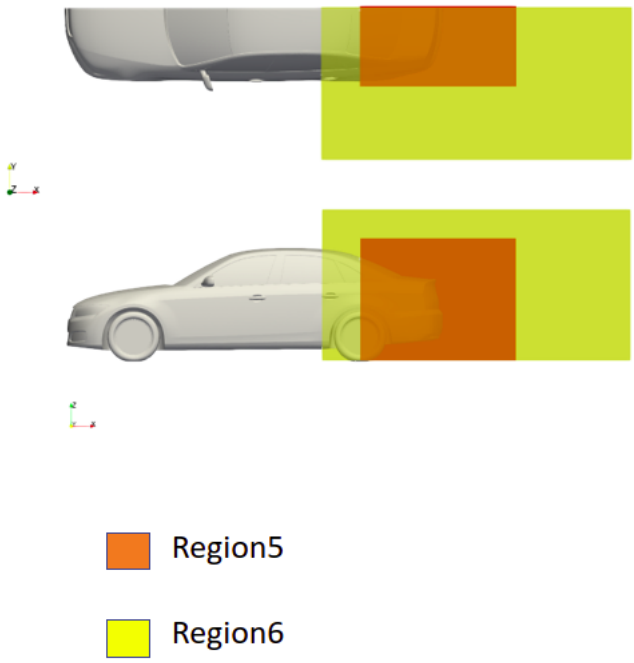


| Coarse Mesh | | |
|---|---|---|
| **Region** | **5** | **6** |
| **Level [-]** | 4 | 3 |

| Medium Mesh | | |
|---|---|---|
| **Region** | **5** | **6** |
| **Level [-]** | **5** | **4** |

| Fine Mesh | | |
|---|---|---|
| **Region** | **5** | **6** |
| **Level [-]** | **6** | 4 |

Table 4.12: Car's wake refinements

Some of the most interesting turbulent phenomena are captured by *Region 5* which is a box with a level of refinement that increase of 1 passing from the coarse to the fine mesh. This box along with the *Region 6* are large regions that are heavier from a computational point of view: in this sense, increasing the level with the fine mesh means to increase a lot the number of cells of the overall grid. The *Region 6* covers fully the C-pillar and also the most external part of the car's wake and it allows a gradual refinement from the wake to the outside.

| Coarse Mesh | | |
|---|---|---|
| **Region** | **8** | **9** |
| **Level [-]** | 1 | 2 |

| Medium Mesh | | |
|---|---|---|
| **Region** | **8** | **9** |
| **Level [-]** | **2** | **3** |

| Fine Mesh | | |
|---|---|---|
| **Region** | **8** | **9** |
| **Level [-]** | 2 | 3 |

Table 4.13: Open-road refinements

For what concerns the farfield domain, the level of refinement of the *Region 8-9* has been increased of 1 passing from the coarse to the medium/fine mesh.

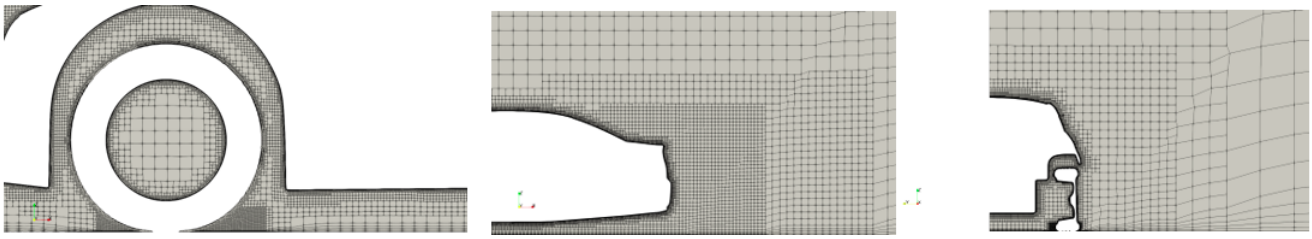

Figure 4.16: Coarse Mesh

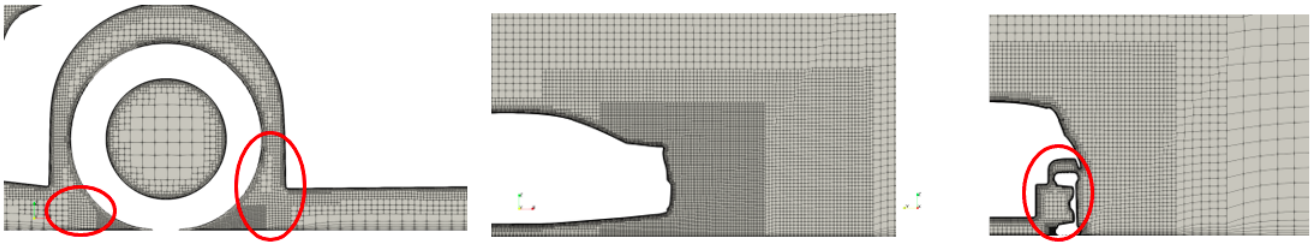

Figure 4.17: Medium Mesh

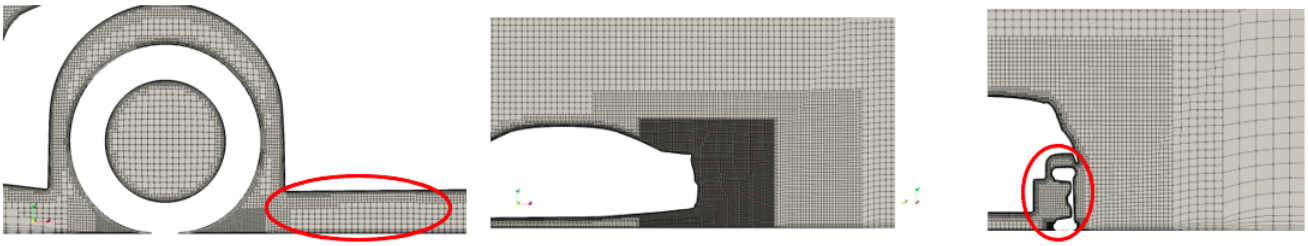

Figure 4.18: Fine Mesh

Figures 4.16, 4.17 and 4.18 summarize what described so far. The number of cells from the coarse to the medium and fine mesh are respectively $\approx 4.54 \cdot 10^6$, $\approx 5.32 \cdot 10^6$ and $\approx 8.12 \cdot 10^6$ cells. The red circles highlight the main differences which were mentioned before with the table and what is involved the wheel's wake, whilst the differences in the car's wake mesh are much more clear passing from the first mesh to the other ones.

### 4.3.5. Numerical schemes

A second-order implicit *backward* scheme is used for discretizing the time-dependent terms. For the gradients of the pressure and velocities the second-order *Gauss linear* is used, as well as for the divergence schemes, but for the the so-called convection term, i.e. $div(\phi, U)$, where a *linearUpwind* is used. This is done to have more stability from a numerical point of view since it becomes as a first order scheme in regions of high gradients, e.g. at the contact patch and on the upper car body where the flow is significantly accelerated. As interpolation schemes the default *linear* scheme is set to interpolate value from cell centers to face centers. For the Laplacian terms *Gauss linear corrected* scheme is used. The specific divergence schemes for all the convection terms are second order accurate.

## 4.4. Results

Before going through a detailed analysis of the simulations, the convergence of the aerodynamics force is proposed.

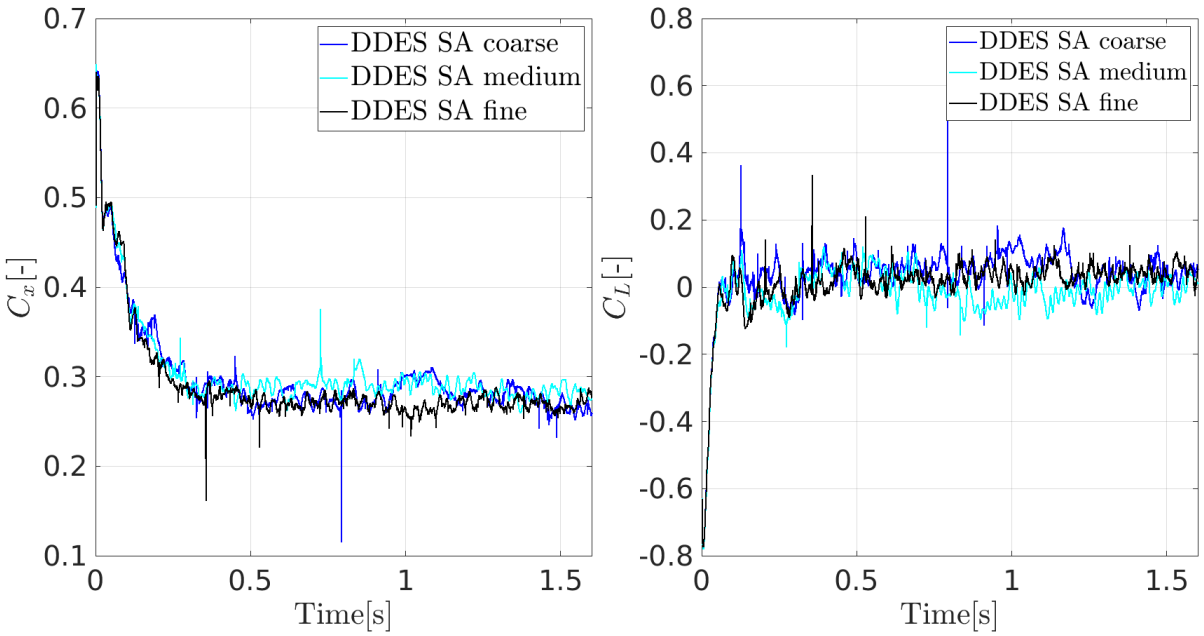


Figure 4.19: Time histories of drag(on the left) and lift(on the right) coefficients

In Figure 4.19, the trends of the overall drag and lift acting on the whole car are shown, for simplicity just of the $DDES_{SA}$ model.
First thing to be noticed is that the oscillations tend to reduce as the mesh becomes finer: the coarse mesh (blue curve) reaches much pronounced peaks of minima and maxima, these peaks are less evident with the medium mesh, even if some oscillations are still evident in terms of average value, whilst with the fine mesh these problems seem to be solved. A good averaged time window is consider after 1.4s of the simulated time up to the end of the simulations (1.6s) where the fluctuations are significantly decreased for all the meshes. In this sense, it is possible to end up saying that the chosen simulation time is enough to reach convergence in the aerodynamic quantities of interest, however to confirm this trend more simulated time should be required and this was not done in this study due to computational limits.

### 4.4.1. Aerodynamic loads acting on the whole vehicle

The results are now compared with the experiments and they are analyzed to see where the differences between each mesh and turbulence models are.

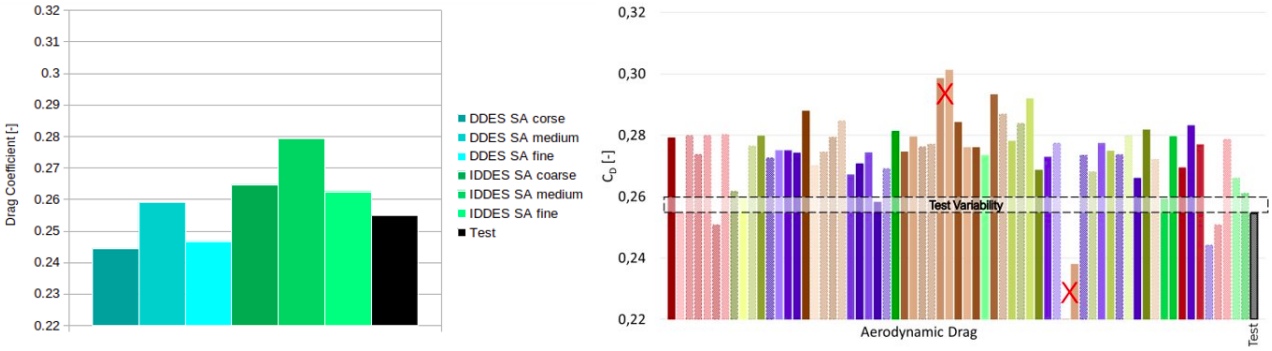


Figure 4.20: Drag Coefficients of this study(on the left) and of this Workshop[3](on the right)

Recalling that the experimental $C_D$ is 0.255, all the value of the forces along the x-direction give an error always below 10%, in fact just with the $IDDES_{SA}{}^{medium}$ is achieved a maximum error of 9.8%. In general, the results of this study are in line with both experiments and what presented during the Workshop [3]: in particular, it is possible to notice that $DDES_{SA}$ models underestimate the experiments, whilst the $IDDES_{SA}$ overestimate them.

As the mesh becomes finer, the errors tends to reduce, in fact, both models have the minima errors for the finest mesh. However, the medium mesh overestimates the forces, not confirming completely the trend identified by the coarse and fine meshes. One reason could lie on the fact that there is a large change of the cells between the outer region of the contact patch and the mesh of the wheelhouse and of the wake, this could generate problem in solving the flow at the contact patch and in the wheelhouse of the front wheel that are the most critical regions to be solved by the turbulence model.

Further investigations are going to be presented to defend these results in the next pages. In general, it is possible to end up with a series of results that lie all in the *Test Variability Region* that was identified during the workshop[3].

For what concerns the lift coefficient, an important and preliminary consideration to be made is that this is a quantity that is more sensitive to all the changes in the simulations setting: from turbulence models, to meshes and time step. Also during the workshop[3], large errors were identified with respect to the tests, especially for what concerns the front part of the vehicle.

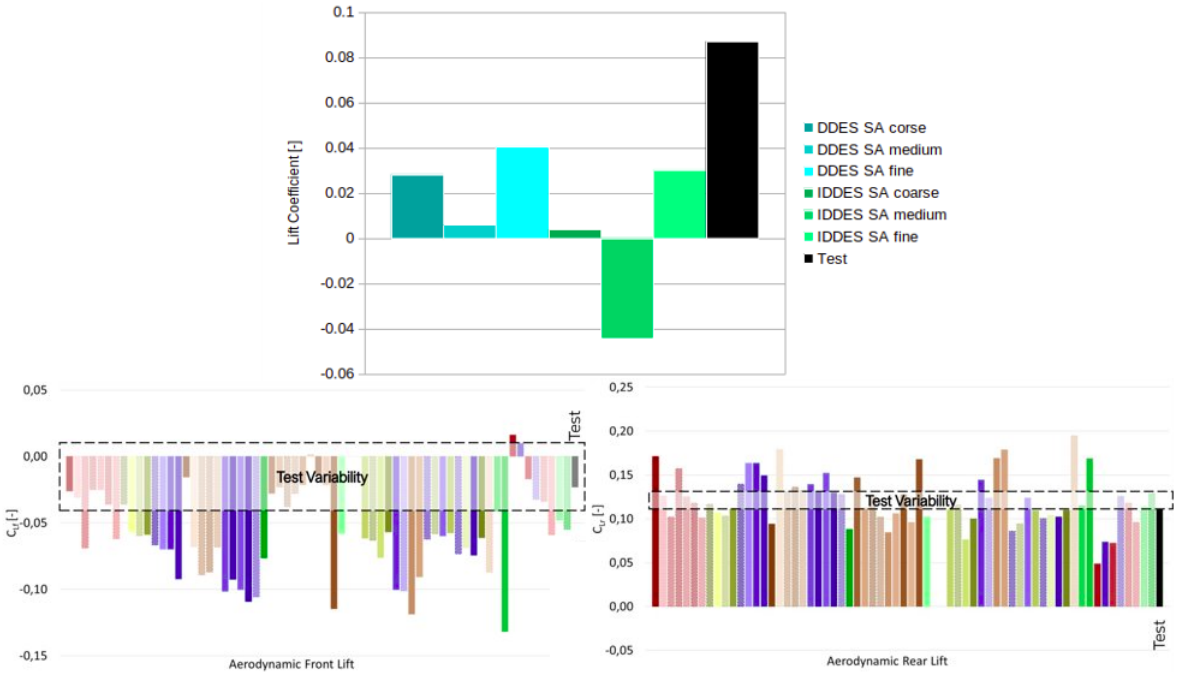


Figure 4.21: Lift Coefficients of this study(on the top) and of the Workshop[3](on the bottom)

The trend identified by those simulations is very close to the one presented during the workshop[3]: in fact, all the estimated lift coefficients are below the experimental test and with the medium mesh there are errors even larger, since a negative lift contribution is generated for the $IDDES_{SA}{}^{medium}$. During the previous section was already shown that lift forces oscillates more in time than drag forces. These oscillations translate also in large differences with respect to the tests. These errors becomes lower with the fine mesh for both turbulence model, even if the gap with the respect to the experiments is high; these differences were evident also during the Workshop[3].

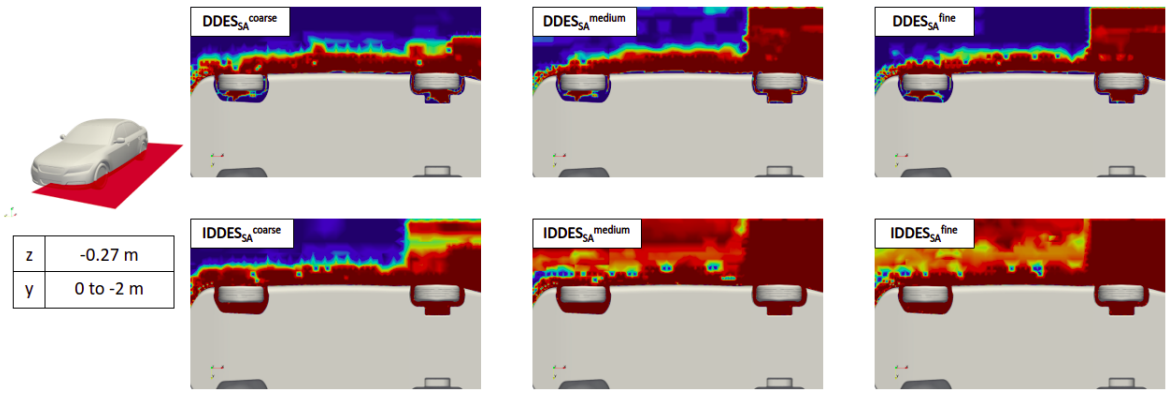


Figure 4.22: DES model regions of all the simulations

To spot the main difference in solving the flow of all the simulations, a plane with a normal

parallel to the z-axis and at a location z=0.27m is presented. With the finer meshes, the LES content is solved more in the wake of the vehicle, but in general a very approximated and average flow is solved for the front wheelhouse: in fact, this region has been always critical from a computational point of view and it is well known also in literature that here the major discrepancies between models and experiments are highlighted. Not the same can be said for the rear wheel, where RAS are used at the walls and LES in the wake, as it should be. All these considerations are valid for the DDES, whilst things change completely with the IDDES. The main difference and problems are in correspondence of the wheels where LES are activated also closer to the walls. This could lead to an overestimate of the forces acting on the car, moreover as the mesh becomes finer LES are activated also on the lateral windows which can be due to an early separation of the model itself.

### 4.4.2. Pressure distributions at various plane locations

The separation is going to be studied in detail, but before going through it, it is interesting to analyze the flowfield in terms of total pressure coefficient which gives informations about the regions where the flow is accelerated and doing so it is possible to make comparisons with experimental average planes of the car's and wheel's wakes.

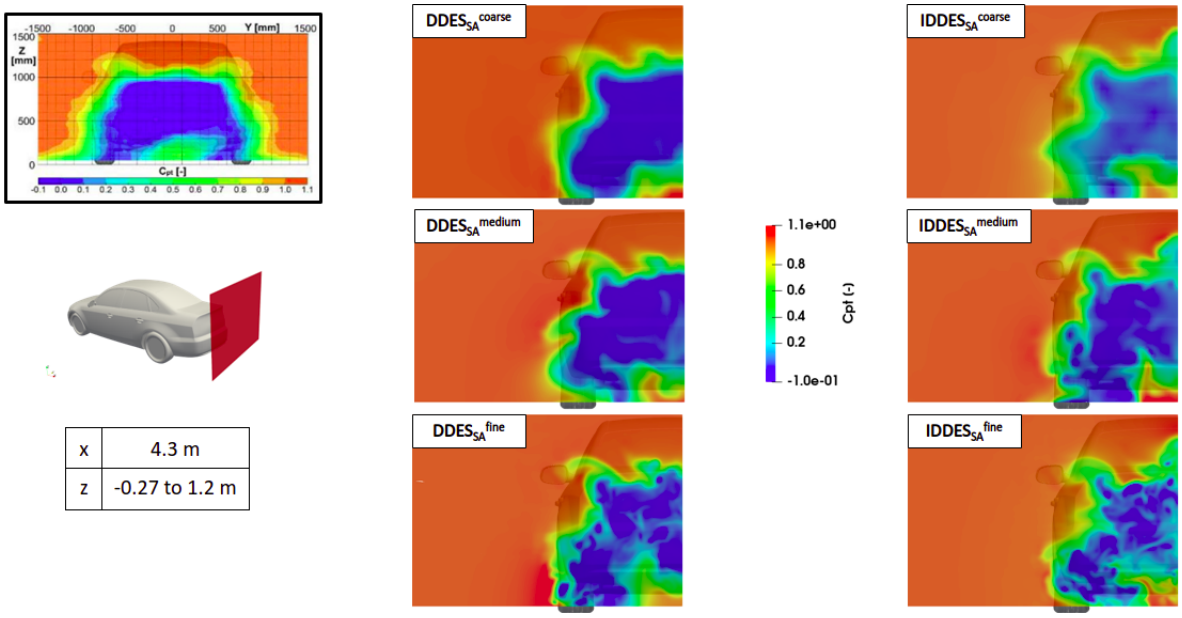


Figure 4.23: Total pressure coefficients of all the simulations at the wake's location

On the top-left of the Figure 4.23, it is proposed the visualization of the measurements taken in the Pirinfarina Wind Tunnel by means of a 14-hole probe that moving on the red plane identifies an averaged flow-field downstream the vehicle. This measure is not so

efficient and effective as a PIV could be, also in terms of required time for data acquisition, however it allows to show some insights of the flow and it is used as a reference for the comparison of such study. On the right of the figure there are two columns which are representative of the data coming from the CFD simulations where the plane is taken at the same distance from the car as proposed in the experiments.
The proposed visualization of the total pressure coefficients are averaged on the same time window, however just with the coarse mesh the "average" behaviour is more evident, especially in the inner portion of the wake: in fact, more homogeneous regions should be identified due to the averaging operation, but this is not clear as the mesh becomes finer, this can be due to the small time window used. The most important difference between the two proposed models relies on the upper portion of the wake where a low-pressure region is identified that can be recognizable into a vortex. This region seems to be even better captured as the mesh becomes finer and it is not present in the experiments, so it needs to be investigated more deeply. The $DDES_{SA}$ model in this sense is still closer to the experiments since it does not capture this region and the pressure distribution is similar to the tests, even if small fluctuation of low and high pressure zone are identified in the wake for reasons already mentioned. Finally, for whats concerns the underbody location, a *not* reliable comparison can be made with respect to the reference plane since the geometries are different.

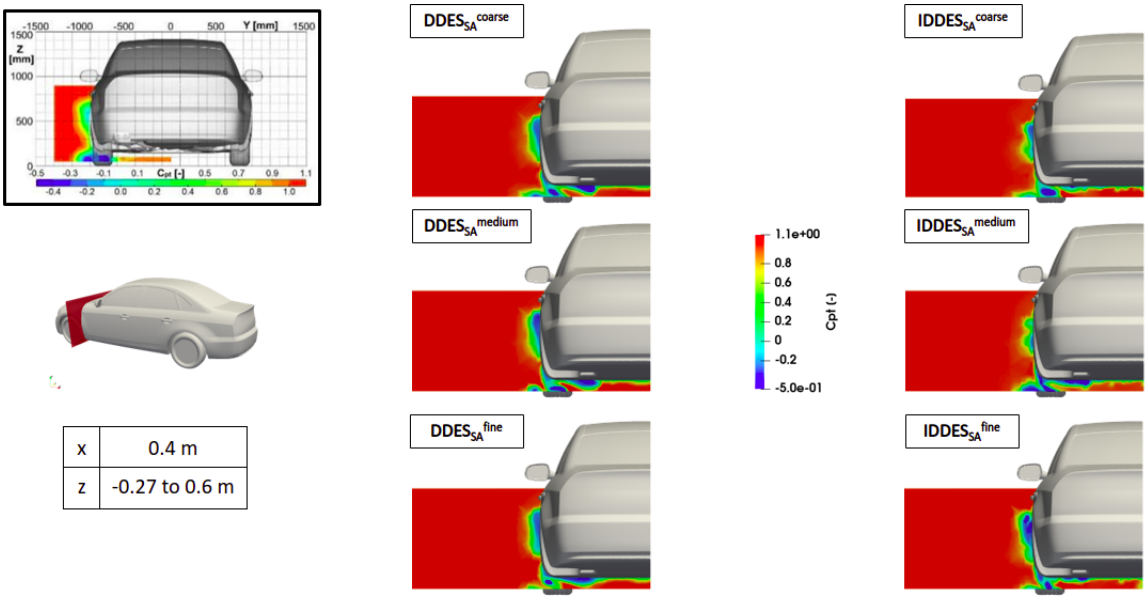


Figure 4.24: Total pressure coefficients of all the simulations at the wheel's location

On the top-left of the figure 4.24, it is still shown the visualization of the test to be compared with. The used plane allows to focus on the fluid dynamic phenomena that

occur on the wheel and the wheelhouse: the aim is at least to identify some of the vortices described at the beginning of this work which are mainly responsible of the drag force generated by the wheel and they involves mainly the vortices that detach from the wheelhouse and the contact patch towards the outside of the vehicle, but also the beginning of the horseshoe vortex which is generated at the contact patch.
The $DDES_{SA}$ model captures for all the meshes the vortex detaching from the wheelhouse and the low pressure region is similar to the test even if less developed, this region is better captured with the fine mesh since the resolution of the mesh at the wheel's wake location improves, increasing also the low-pressure are in the vicinity of the wheel. On the other hand, the $IDDES_{SA}$ turbulence model is not able to capture fully this behaviour, especially with the coarse and medium mesh which experience very little low pressure regions on the outer portion of the wheel, this can be due to a combination of an early separation of the model and a low resolution of the mesh. Things improves with the fine mesh, even if the core part of the low-pressure region at the wheelhouse location has lower value than test and the other model. In general, the $IDDES_{SA}$ experiences both in the car's and wheel's wakes more fluctuations than the the $DDES_{SA}$, so, besides the causes already mentioned, further visualisations about the flow development are proposed in the next section.

### 4.4.3. Flow development

Everything shown so far, from DES regions to pressure distributions can be somehow summarized in the flow development on the car. To this end, the Q-criterion is exploited. Data are presented for simplicity only for the fine mesh of both turbulence models.
For turbulent shear flows, the so-called *Coherent structures*(CS) are representative of spatially coherent and temporally evolving flow vortical structures. To identify vortical structures that are dynamically significant, it is necessary to recall the definition of a vortex. Nowadays there is not a unique definition, but in general they can be associated to either low-pressure regions, closed or spiralling streamlines and pathlines or isovorticity surfaces. At this point the analysis shifts to the identification of the location of vortex cores. To end up with a generic definition, Jeon and Hussain [27] proposed a definition that combines the vorticity magnitude with the strain rate magnitude, so it involves the second invariant of the velocity, Q, from which this method is called *Q-criterion.*
Q describes the unbalance between vorticity magnitude and the strain rate and according to this criterion a vortex is identified for positive values of Q, or in a more generic form where there are two real negative eigenvalues of the symmetric tensor $S^2+\Omega^2$, with S and $\Omega$ respectively the symmetric and skew-symmetric component of $\nabla\mathbf{u}$.

For a value of Q=5000 the most important flow structures are shown in such study. As already said, the simulations have been performed for just half of the car, whilst in Figure 4.25 the whole vehicle is shown, this is done just for visualization porpoise and by exploiting the *reflect* filter available in Paraview.

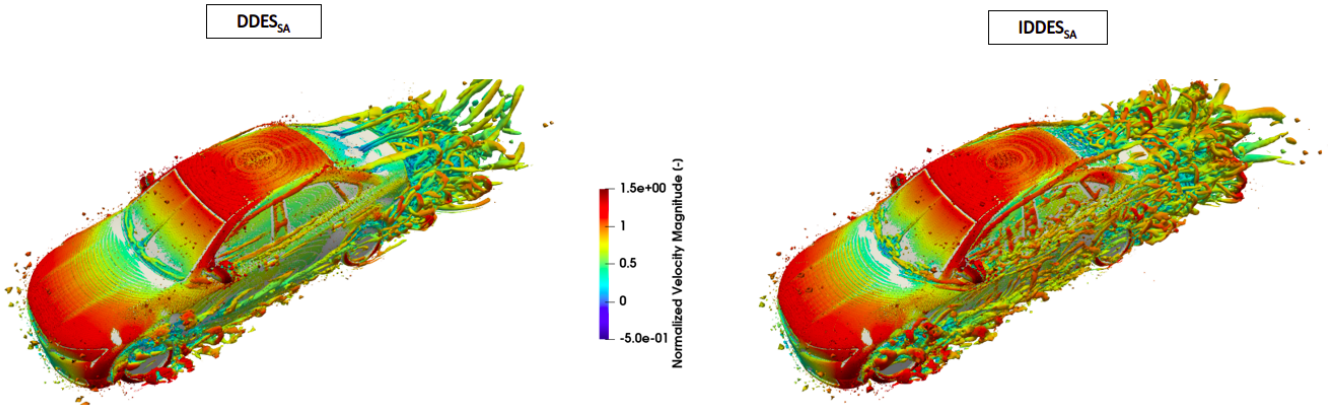


Figure 4.25: Flow visualization: Q-criterion (Q=5000)

A general and, at the same time, important consideration is that $IDDES_{SA}$ predicts a premature flow separation on almost all the surfaces of interest with respect to $DDES_{SA}$. Starting from the wheelhouse, it is possible to notice that the $DDES_{SA}$ model shows vortices that are detaching both from the upper body of the wheelhouse and from the wheel towards the outside that is a peculiar characteristic of the flow regime in case of stationary wheels, whilst a very high number of vortex structures are identified for the $IDDES_{SA}$, beside those already described.
The same goes for the flow downstream the mirrors along with the side windows, here the flow is much more separated with respected to the tests. The most important consideration concerns the C-pillar: the flow for the $DDES_{SA}$ keeps to be attached for a while and then it separates by generating large flow structures on the rear of the car, whereas in $IDDES_{SA}$ the flow separates in the immediate vicinity of the beginning of the C-pillar, leading to the major difference which is a vortex on the upper portion of the wake. This vortex is the one represented before by a non-physical low pressure region and it was clear for all the meshes. Furthermore, in the wake still small structures are more evident, as it was for the mirrors. The flow velocity is increased on the upper portion of the vehicle, leading to the separation on the back and, similarly, flow accelerations are detected on the side of the vehicle especially for the $IDDES_{SA}$. For those reasons, to make a more complete analysis, it is interesting to see how the skin-friction coefficient is distributed along the car, highlighting the regions of separations. This could allow to understand clearly why the forces are over- or under- estimated with respect to the experiments.

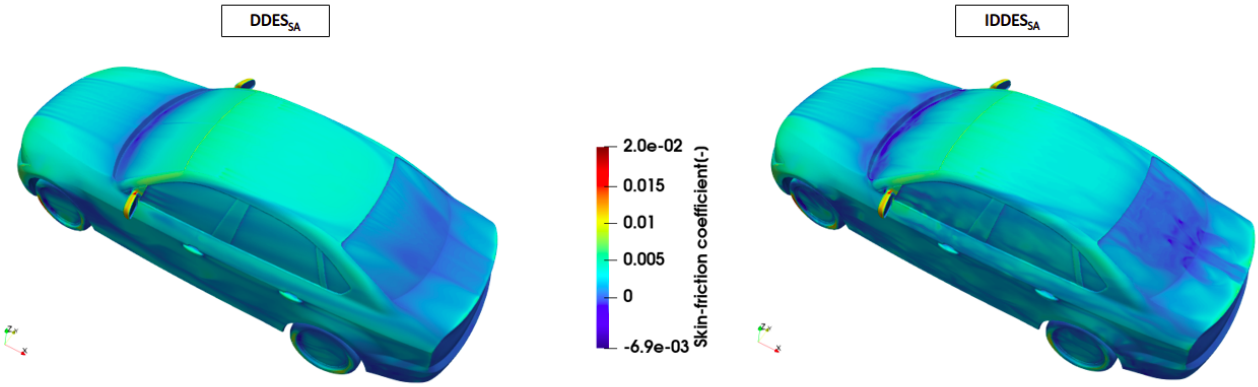


Figure 4.26: Skin-friction coefficient distributions: streamwise component

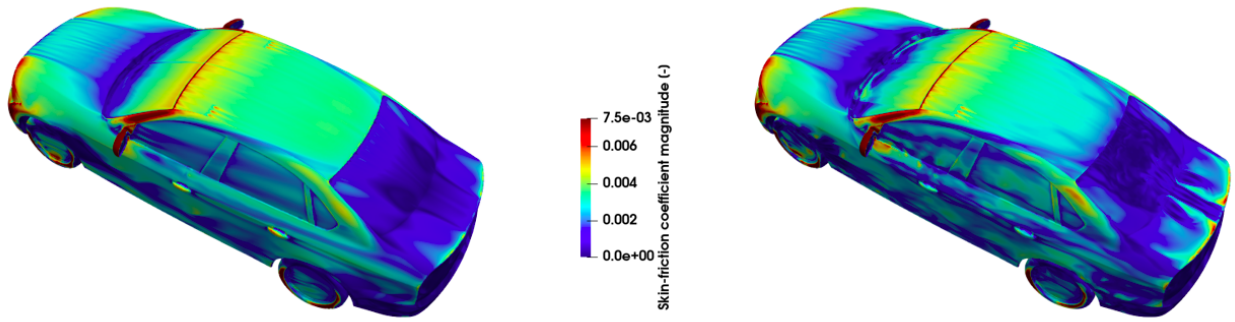


Figure 4.27: Skin-friction coefficient magnitude distributions

In Figure 4.26 it is shown the streamwise component of the skin-friction coefficient to highlight the regions where the flow separates: it is evident that this is underestimated for the case of the $IDDES_{SA}$ especially on the notchback body where the flow is highly turbulent e separation occurs massively with respect to the $DDES_{SA}$. Moreover, plotting also the magnitude of this coefficient it is possible to visualize better the regions where it is underestimated: in fact, looking at the figure 4.27 one can notice that the main differences are on the C-pillar and on the side windows where it fluctuates a lot, as well as on the rear rim. These considerations can be at the basis on the differences between the two models in terms of aerodynamic forces.

### 4.4.4. Detected vortices downstream the car

To have a look more in detail to the genesis of the vortices that are detaching from the notchback body, the velocity profiles are shown at two different locations, one at the lower section of the notchback body, i.e. $R_3$, and the other one in the wake of the car, i.e. $V_3$.

Doing so, it is possible to have eventually a more consistent model validation, but at the same time some insights of the flowfield are going to be discovered.

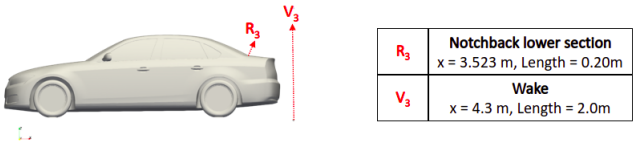


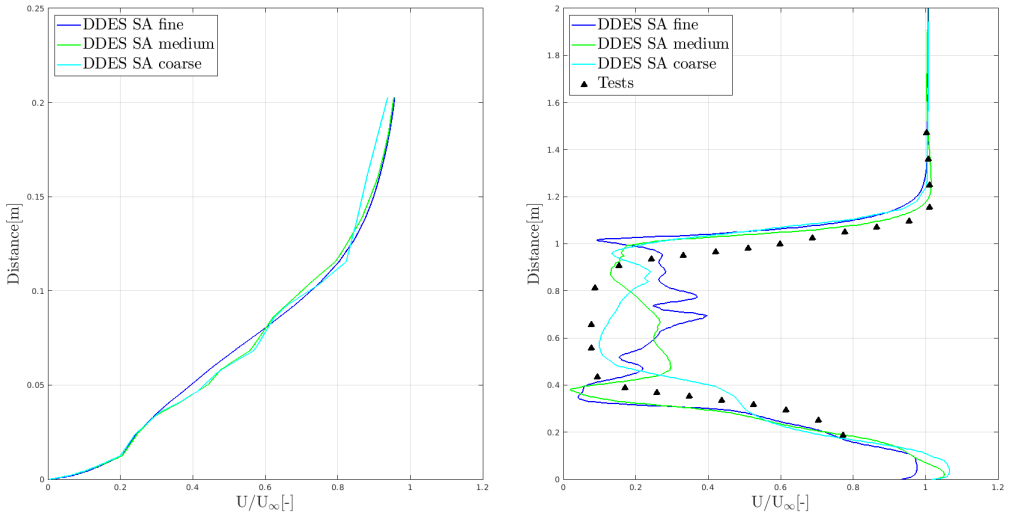


Figure 4.28: Velocity profiles at $R_3$(on the left) and $V_3$(on the right) of the $DDES_{SA}$

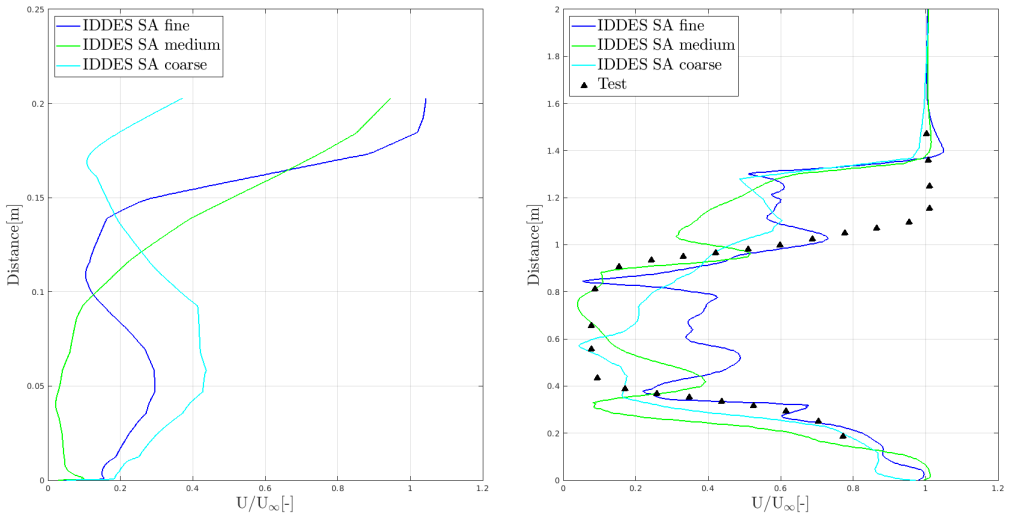


Figure 4.29: Velocity profiles at $R_3$(on the left) and $V_3$(on the right) of the $IDDES_{SA}$

These figure propose the average velocity profiles normalized with respect to the free

stream condition. It is worth to say in advance that eventually fluctuations are going to be present even if the mean profiles are considered, this is still due to the combination of small time window and relative high time step used.
For the $DDES_{SA}$, there are not problems worth to be mentioned yet, in fact the profiles at the location $R_3$ are almost the same, just the coarse mesh it is a bit slower with respect to the other meshes to reach the free stream velocity, whilst for the plane $V_3$ there is in average a good agreement with experimental data with more fluctuations inside the wake. For whats concerns the other model, differences are much more evident already at the plane $R_3$ where the coarse mesh is completely out of the profile identified by the previous model and it is different with respect to the other meshes. As the mesh becomes finer the recirculating regions are evident, here with high probability is where the nonphysical vortex identified by the $IDDES_{SA}$ model, is generated. Looking at the profiles at the plane $V_3$ in the figure 4.29, all the meshes fluctuating a lot more with respect to the experimental value, also in the wake of the car, but most important an accelerated flow region is clearly identified in the upper part of the wake.

## 4.5. Final remarks

$DDES_{SA}$ resulted to be the most appropriate model to simulate the flow around the DrivAer in terms of aerodynamic loads, pressure and velocity distributions.
From a numerical point of view, there are not problems to be pointed out, in fact the residuals of pressure and velocities decreased of sufficient orders of magnitude and the main quantities of interest, i.e. the drag and the downforce, reached convergence after 1.4s of the simulated time.
A generic behaviour that was identified in all the meshes is that the $IDDES_{SA}$ model switched too prematurely to LES, leading to an nonphysical separation and differences flow developments on the rear of the car. This, in turn, generates an overestimate of the aerodynamic coefficients with respect to the test. However, the errors tends to decrease for the fine mesh at least in terms of drag, whilst the lift is a quantity a lot more sensitive to the mesh and model changes. This peculiarity was noticed also during the workshop [3] where discrepancies were more evident on the front of the car, especially in the front wheelhouse where the flow is very difficult to be approximated. Here, the $DDES_{SA}$ model uses mainly a RAS behaviour, whilst the $IDDES_{SA}$ uses LES: the latter switches too often to LES, sometime even more close to the wall and this could be for sure a source of error.
Some test have been carried out for the $IDDES_{\kappa-\omega SST}$ model, but simulations have never reached convergence, however some interesting points are worth to be pointed out: this model, even with the cylinder test case, results to have high mesh requirements and so to be more expensive from a computational point of view. Furthermore, it is highly sensitive to the inlet boundary conditions for the turbulent kinetic energy and the turbulent dissipation rate and by using the recommended values for OpenFoam the simulations crashed early. By triggering this parameters, the simulations turned out to be more stable from a numerical point of view, even if the convergence was not reached. For further studies it could be interesting to run simulations with this and other new turbulence models and compare data with those proposed in this work. It could be required to launch some RAS simulation to have initial guesses that are more in agreement with the final results, but also to have a more stable solving process. Finally, the $IDDES_{SA}$ could be somehow improved by triggering some model constants among which the constant $C_{d1}$ which is responsible of the switch from RAS to LES mode, trying to delay the separation as much as possible in order not to have a nonphysical flow development.
It has been interesting to study how these models works and how changes in the mesh could affect the results, but at the same time manage a large amount of simulations and data with limited computational power and laptot limits have been challenging. For those

reasons, the next step of this work is to try to decrease the required computational power.

# 5 | Sensitivity analysis to the C.F.L. condition

## 5.1. Summary

During this chapter, a way to decrease the simulated time is investigated. This can be done by increasing the time step for which a dimensionless representation is given by the Courant number. The higher the Courant number, the lower the simulated time, however this has a strong impact also on the solving process, particularly the numerical stability is affected.
The results are analyzed from pressure and velocities fields to the Courant number distributions. Finally, some considerations are made also for the residuals and possible improvements are discussed.
This kind of investigation has been chosen to be done downstream all the simulations carried on so far, to test just the best turbulence model which in this case is the $DDES_{SA}$.

## 5.2. Case study

There are different ways to reduce significantly the simulated time among which:

- using a coarse mesh;
- decreasing the simulated time T;
- increasing the time step $\Delta t$;

Making the mesh coarser would have a strong impact on the quality of the results and it is already investigated that the coarse and medium mesh have some limitations with respect to the finest mesh, so this way is not going to be used.
The second way that is proposed is to the decrease the simulation time which was previously of 1.6s, however it has been already shown that forces start to convergence after about 1.4s and the time average windows is limited to 0.2s; moreover increasing the time step would mean to have a smaller amount of data which could have an impact on the average operations.
The third way is to increase the time step, this could have an impact on the solving process for sure, so it needs to be analyzed, but the impact on the quality of results could be less drastic with respect to the previous two ways.

### 5.2.1. Literature Review

Recently a similar work has been carried out by Ekman[5]. During this paper, a modern turbulence model has been tested, i.e. SBES("Stress-Blended Eddy Simulations"), proving that it fits with the DrivAer simulations. He performed a comparison between this model and the $DDES_{\kappa-\omega SST}$ and the $IDDES_{\kappa-\omega SST}$ and he highligthed the differences which rely mainly on the LES capabilities of each model.
During the final part of his work, he proposed a way to decrease the simulated time by increasing the time step. He used a very low time step to tests the model, namely $1 \cdot 10^{-6}$s, but this was done because a much finer mesh was exploited and especially because in testing new models the numerical requirements are higher for stability reasons. He showed results for a mesh which was capable to simulate a wind tunnel configuration at different yaw angles and the results are compared with very similar test carried on by Wieser [26].

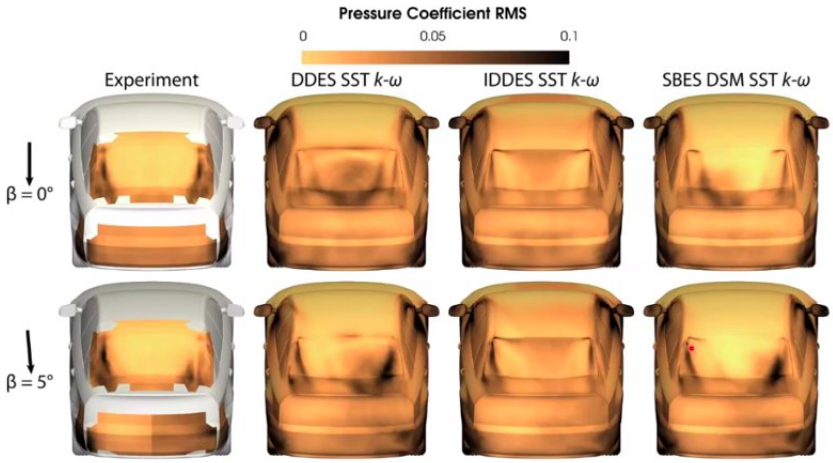


Figure 5.1: Surface pressure fluctuations at different yaw angles [5]

However, during the last part of the workshop, he proposed to go over the CFL stability condition which impose a Courant number lower or equal to one everywhere: by increasing the time step $\Delta t$ from 10 to 100 times, he ended up with interesting conclusions regarding pressure and forces fluctuations, beside the saved computational power.
The aim of this chapter is to emulate what has been done by Ekman, but investigating a different turbulence model, i.e. $DDES_{SA}$, new time steps and test case in terms of mesh. Comparisons cannot be performed with those CFD data, since he studied a different test case where the DrivAer placed on a splitting table to reproduce the experiments[26] and to perform also the analysis at different yaw angles.

## 5.3. Methodology

The same test case which was presented in the previous chapter is now used for a different purpose, so the mesh used is the finest with same geometry and Reynolds, as well as the number of correctors, tolerances and numerical schemes. What changes is the time step for which a dimensionless flow unit is also considered:

$$\Delta t^* = \frac{L}{\Delta t \cdot U_\infty}[-]$$

.

| **Increment[-]** | $\Delta t$**[s]** | $\Delta t^*$**[-]** |
|---|---|---|
| **x 1.00** | $2 \cdot 10^{-4}$ | 629.98 |
| **x 1.25** | $2.5 \cdot 10^{-4}$ | 503.99 |
| **x 1.50** | $3 \cdot 10^{-4}$ | 419.99 |

Table 5.1: Time steps settings

Three different time steps are used and they are obtained taking the original one and multiplying it by an increment factor. The dimensionless time step $\Delta t^*$ is normalized respect to the car geometry and the free-stream velocity, so it gives a more complete description of what is changing. However, to have the a more clear overview about each simulations the Courant number needs to be taken into account and this is going to be shown in the next sections. The time step of the simulations was already high, namely, $2 \cdot 10^{-4}$s, so the increasing factor could not be of the orders presented by Ekman, since the Courant number could be too high.

## 5.4. Results

Changing the time affects mainly the convergence and the way equations are solved, so as first results it is important to show the drag and lift time histories and spot eventually differences with respect to the original test case.

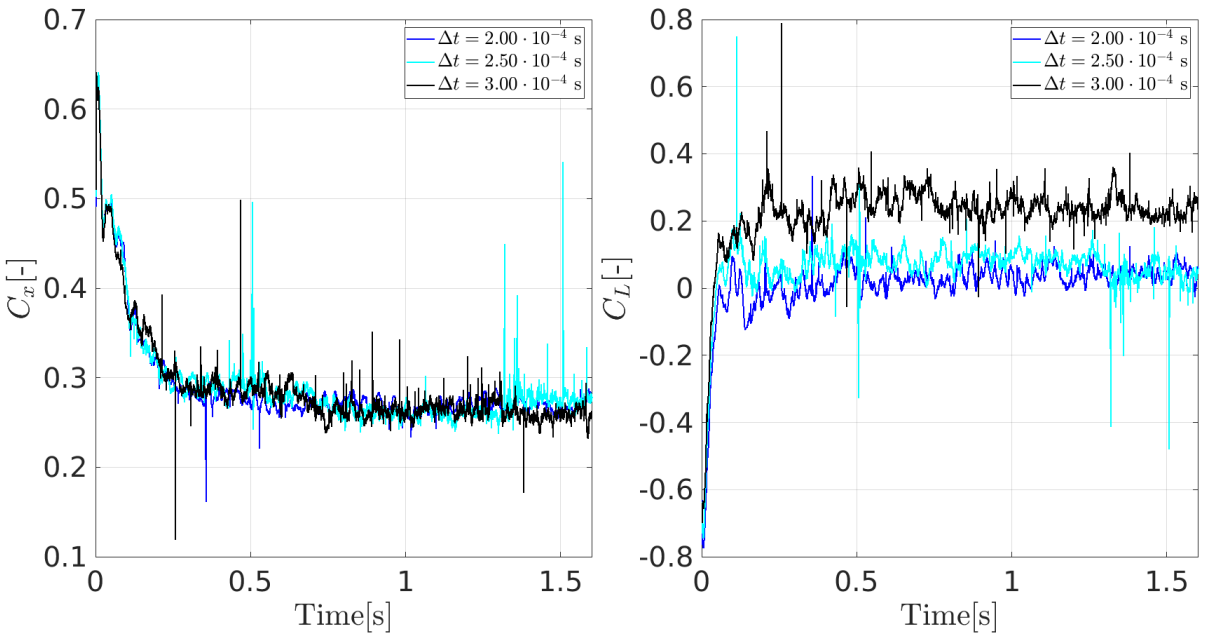


Figure 5.2: Time histories of drag(on the left) and lift(on the right) coefficients

As the time steps increases the oscillations tend to increase as well and the mean value is affected: the drag seems to be less sensitive to this change, even if some oscillations are detected for the second time step in the last part of the simulations, whilst the lift coefficient is much more affected. On the right of the figure 5.2, the averaged values of the lift coefficients for all the time steps change, but larger and critical differences are evident with the largest time step, i.e. $\Delta t = 3.00 \cdot 10^{-4} s$, that seems to be out of the value identified before. More investigations from a numerical point of view are then needed, so the maximum Courant number is analyzed.

| **Increment[-]** | $\Delta t$**[s]** | **CFL**$_{max}$ |
|---|---|---|
| **x 1.00** | $2 \cdot 10^{-4}$ | 43.21 |
| **x 1.25** | $2.5 \cdot 10^{-4}$ | 62.61 |
| **x 1.50** | $3 \cdot 10^{-4}$ | 70.58 |

Table 5.2: Maximum Courant number for the different time steps

The Courant obviously increase with the time step, but passing from the second to the third time step and there is lower increment among the maxima CFL.

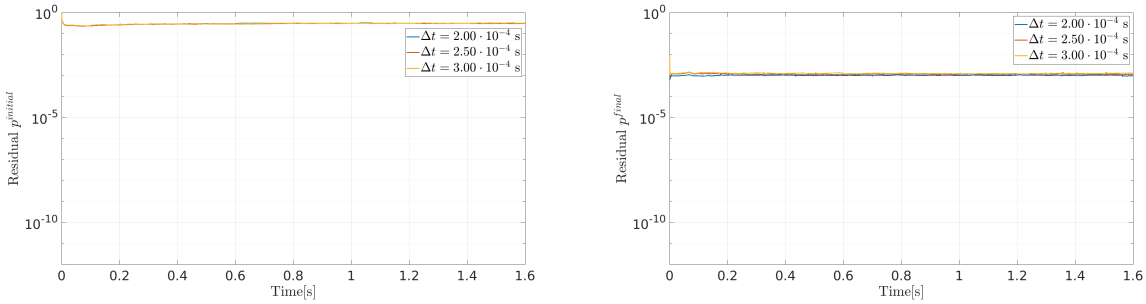


Figure 5.3: Residuals of pressure vs. Time for different time steps

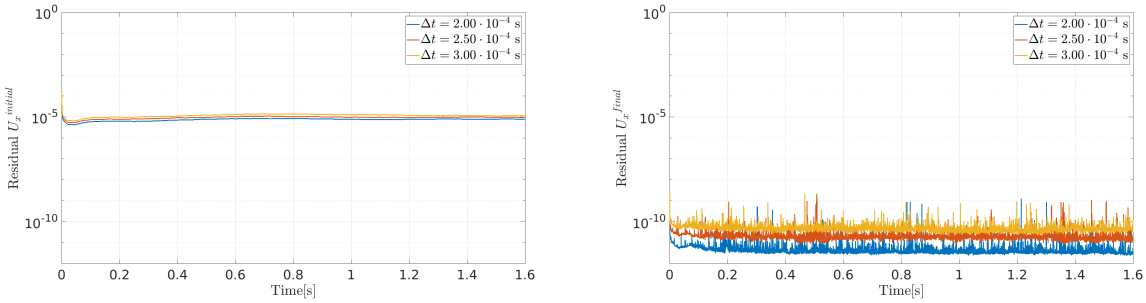


Figure 5.4: Residuals of $u_x$ vs. Time for different time steps

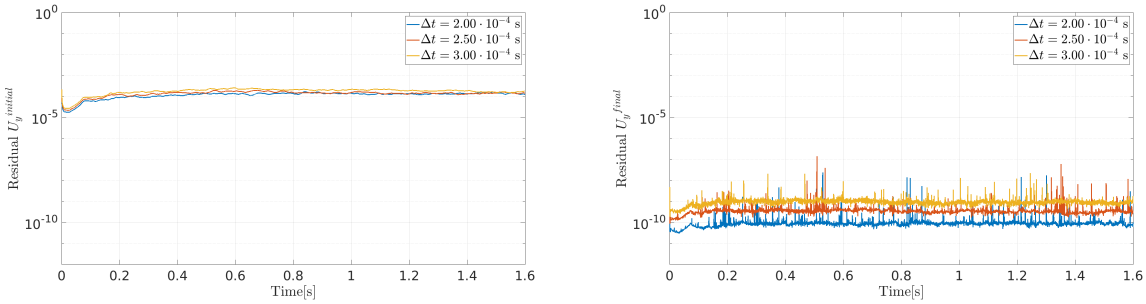


Figure 5.5: Residuals of $u_y$ vs. Time for different time steps

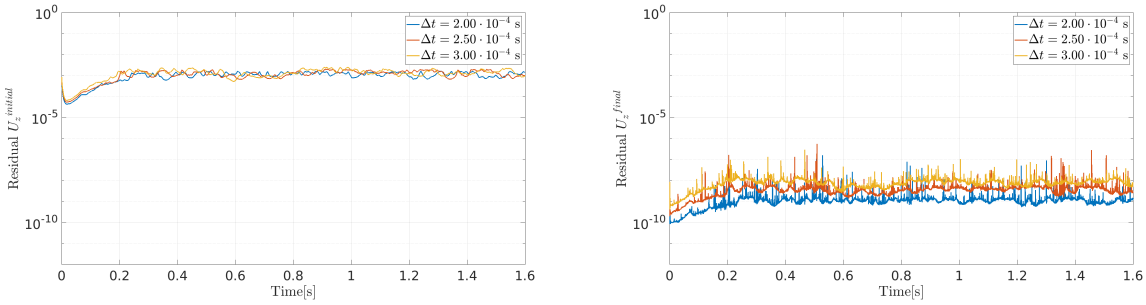


Figure 5.6: Residuals of $u_z$ vs. Time for different time steps

However, to have a more exhaustive and complete analysis of the whole simulations the

residuals have been studied: from the Figure 5.3, the initial residuals are decreasing slowly, but it is worth to recall that this is relative to the first iteration, in fact considering two outer correctors the second residual goes from $10^{-2}$ to $10^{-4}$, nevertheless this behaviour becomes worst and worst as the time step increases. Looking at the residuals of he velocity (Figures 5.4, 5.5 and 5.6), especially the final residual change of almost one order of magnitude among the three simulations, but the solving process is still quite good since the residuals go down from $10^{-10}$ to $10^{-12}$.
Finally, the most critical points concern the lift oscillations and mean value and the residuals of the pressure, so at least one more corrector for the pressure equation and more simulated time should be required to confirms the trends identified so far.

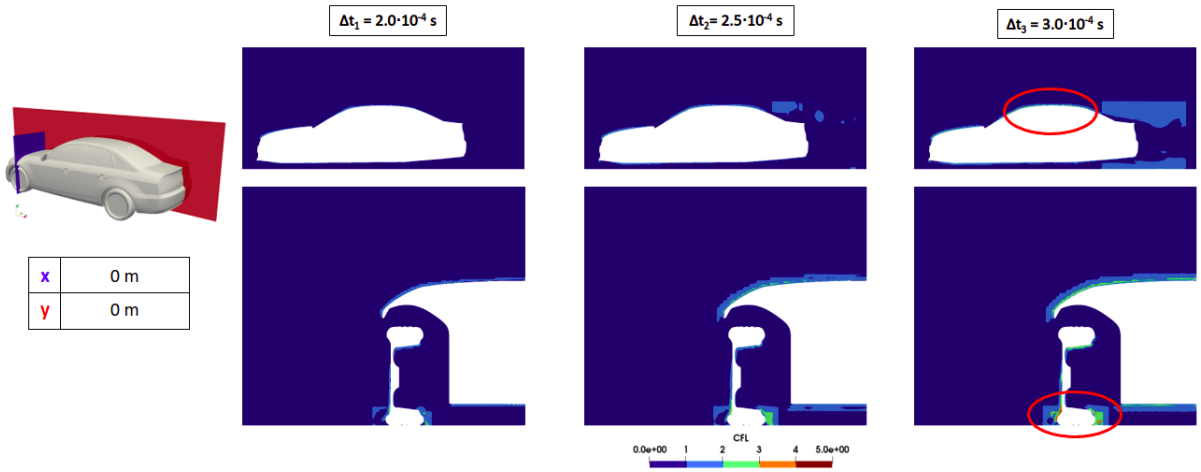


Figure 5.7: Courant number distributions on two different cutting planes

By visualizing the Courant number distribution, it is possible to end up that the critical regions are those highlighted with red circles in Figure 5.7 where the flow is significantly accelerated, in particular at the contact patch where strong viscous effects are present and the Courant increases a lot: as expected, as the time step increases the Courant does as well since it is direct proportional to it. In those picture it is not present the maximum value recorded during each simulation, because it is difficult to to find the plane(s) that intersect exactly the point(s) where the velocity is considerably higher.

### 5.4.1. Aerodynamic forces at various time steps

After this introduction about the convergence and the stability of the simulations, the averaged values are considered for the model validation.

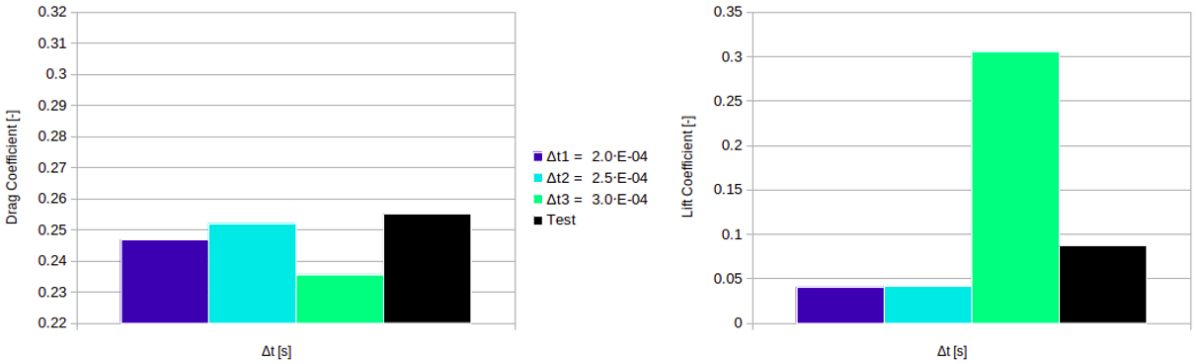


Figure 5.8: Drag(on the left) and lift(on the right) coefficients for the three time steps

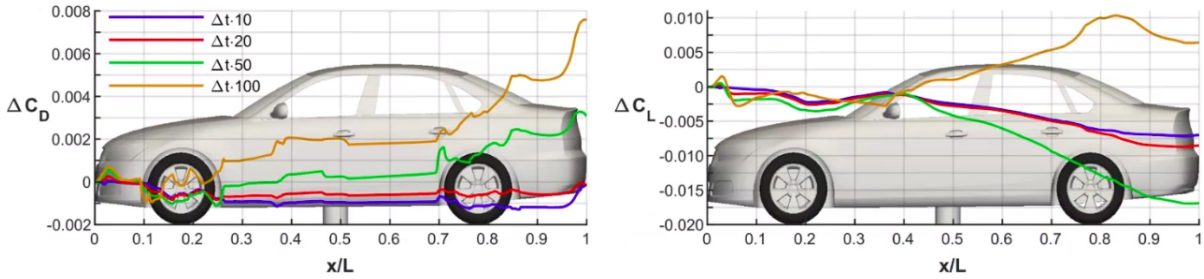


Figure 5.9: Variations of drag and lift along the car at different time steps by Ekman[5]

As expected the drag coefficient value is less sensitive to time step changes, even if with the coarser time step larger errors are identified. In general those values are close to the experiments, so not specific problems need to be highlighted.
On the other hand, even if the lift coefficients are very similar between the first two time steps, the third time step is out of the expected values. Ekman found that increasing of a factor of 10 the time step, the results were not affected too much, but approaching to the time step used in such study differences are more evident. Large differences were detected particularly on the back of the car as shown in Figure 5.9, so the back of the DrivAer is a region that has been investigated more in detail to spot eventually the problems that lead to this over estimations of the forces acting on the vehicle. It is worth to say that the increment factor is also relative to first time step used: if the smaller time step is already high, the increment factor are going to be relaxed accordingly.

### 5.4.2. Total pressure and skin-friction visualizations

Recalling the plane in the wake of the car which has been used before for comparison between meshes and turbulence models, the total pressure coefficient visualizations are proposed.

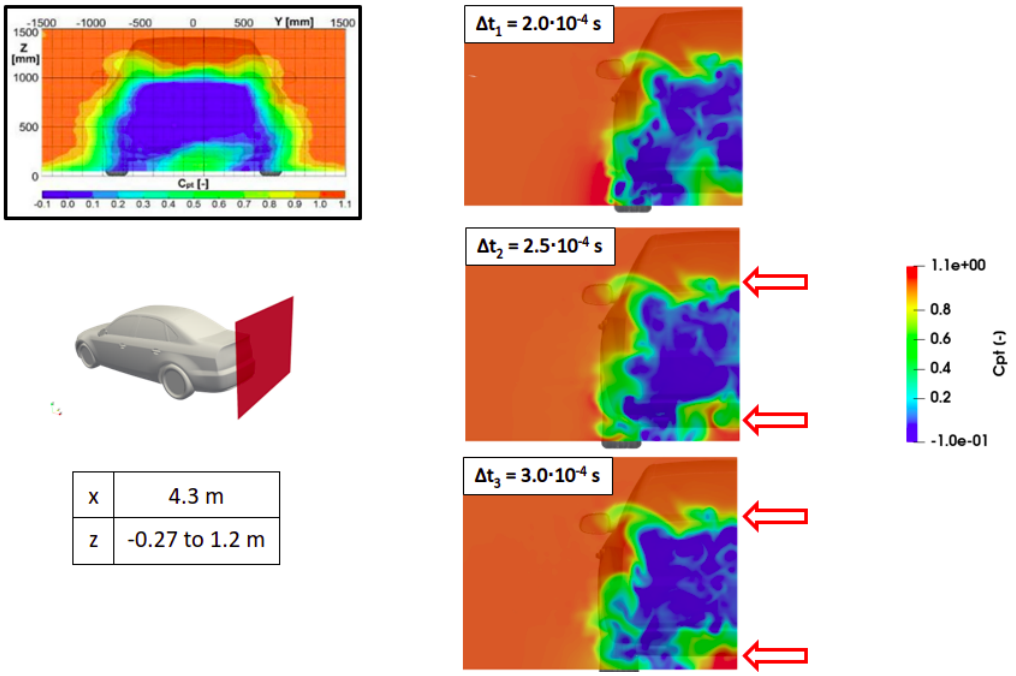


Figure 5.10: Total pressure coefficient in the wake of the car at the different time steps

Some difference among the simulations are spotted by means of the red-countered arrows. The main differences are on the underbody region, where a high pressure regions is found: the values increase with the time step, leading to a large error at the back of the car and so of the aerodynamic loads, as it was found by Ekman. Similarly differences are detected at the rear wheel location, so at the external portion of the wake, where the total pressure is underestimated with respect to the original case. However, even if the experimental visualizations are proposed on the top left of the figure, it is not worth to make comparisons since the underbody geometries are different.
On the upper portion of the body, a smaller low-pressure region is identified and it seems to increase its size with the time step. This region is nonphysical, but the difference with respect to the test can be due to the small time windows used for the average which becomes smaller with the time step.

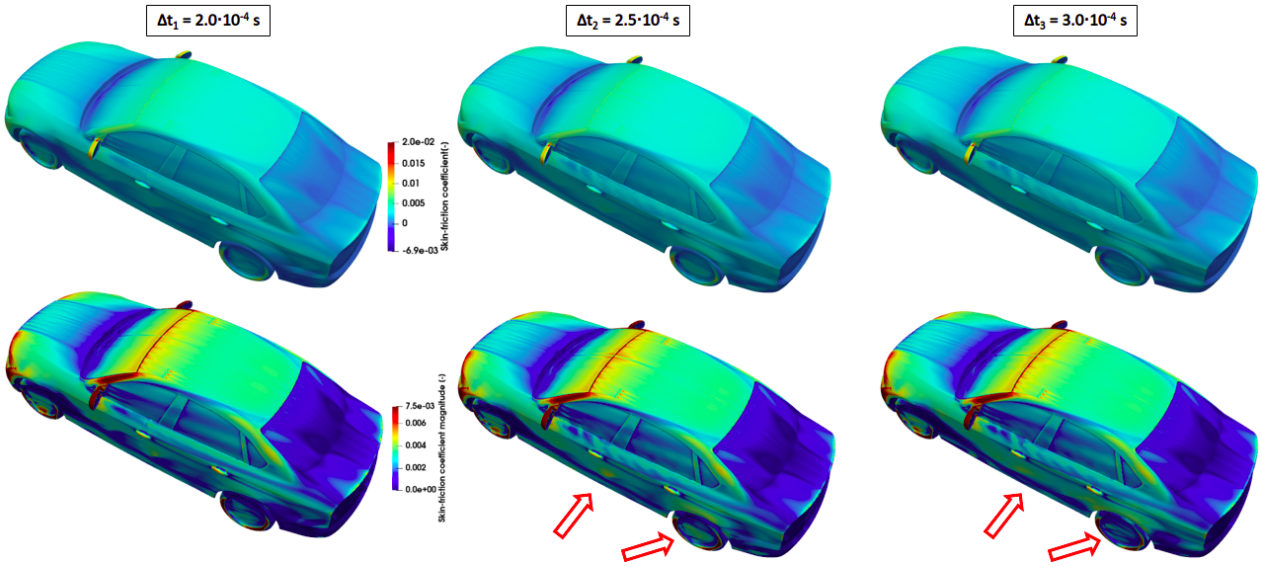


Figure 5.11: Skin-friction coefficient at the different time steps: streamwise component(on the top) and magnitude(on the bottom)

The skin-friction coefficient is plotted first for its x-component since it gives more informations about the separated flow regions, however differences are difficult to be spotted if looking at just one component of the vector: from the top of the Figure 5.11 fluctuations are found on the side windows and on on the rear rim where the skin-friction is underestimated. Looking at the magnitude of this vector, differences between the simulations are more evident in those regions.
The combination between the pressure distribution on the rear of the car and the underestimation of the skin-friction on the side of the vehicle leads to large differences on the forces and so on the aerodynamic coefficients.

### 5.4.3. Saved computational power

To find the best time step to be used for such turbulence model and test case, the computational time has been multiplied with the used number of cores.

$$Computational\ power[h \cdot cores] = ClockTime[h] \cdot NumberOfCores[cores]$$

The computational power is considered along with the errors computed with respect to the experiments and, since the drag coefficient is less sensitive to all the changes of a simulation, it has been considered for such purpose.

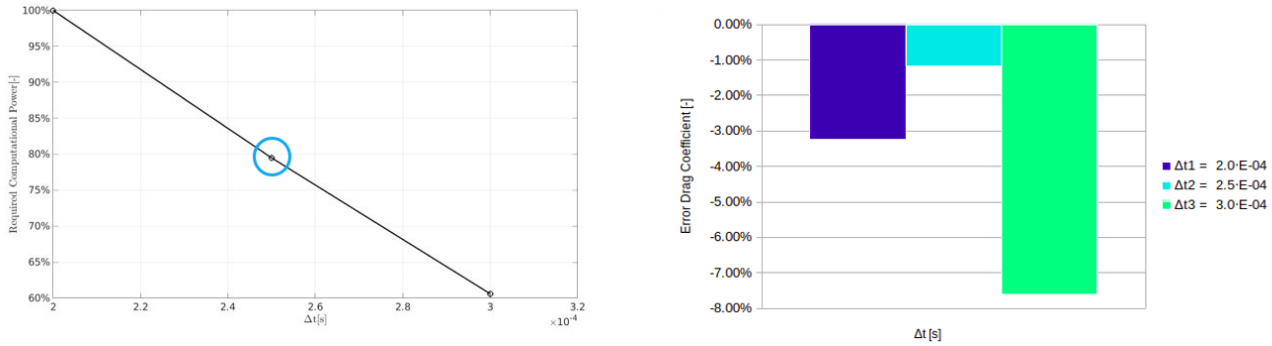


Figure 5.12: Computational power vs. time step size(on the left) and drag coefficient errors at various time steps(on the right)

All the errors of the drag coefficient are below 10%, specifically the error becomes high for the third time step, this confirms what already seen for the aerodynamic forces and visualizations, whilst the error is minimum for the second time step, i.e. $\Delta t = 2.50 \cdot 10^{-4} s$. On the other hand, looking at the left part of the Figure 5.12, the computational power is shown: the 100% of it is relative to the first time step, then increasing the time step there is a almost linear decreasing for the three meshes. Finally, even if the oscillations are higher and more simulation time should be required, the mean value is such that it is worth to use the second time step, saving more than 20% of the computational effort.

## 5.5. Final remarks

This last analysis allows to make important considerations that could reduce the required computational power by keeping a good agreement with results at the expenses of the numerical fluctuations. The pressure equation is mainly affected by those changes and one or two additional correctors should be required to decrease more the order of magnitude of the residuals.

Furthermore, to confirm the convergence of the forces more simulation time is necessary for higher time steps since forces, in particular lift, is affected by larger oscillations which, in turn, impact on the mean values. It was found by Ekman that variations of the aerodynamic coefficients were more visible in the rear of the car[5] and lift increased significantly for larger time steps, as it has been noticed for such study.

Differences rely first on the way the equation are solved and so on the pressure fields where high total pressure regions are identified at the underbody location. Significant variations are also detected on the wall-shear stress distributions specifically on the side of the vehicle where relative dimensionless coefficient is underestimated, as well as on the region between the C-pillar and the rear lights.

As a consequence and outlook for future works, it could be interesting to monitor more deeply the numerical stability of the simulations and see if there are any changes, besides those mentioned before, that can be made to lower down even more the computational efforts.

## 5.6. Final conclusions and outlook

This thesis works has been an interesting and challenging work given the high number of simulations and big amount of data to be post-processed.

Starting from the study of the literature, it allowed to spot what can be added to the current state of art. The study of the flow around a cylinder at very high Reynolds number has not been widely studied probably due to wind tunnel limitations and just three papers[22][19][23] resulted to be in line with the numerical simulations that have been performed. During the model validation, it has been noticed that due to the mesh resolution, $\kappa-\epsilon$ and $\kappa-\omega$ SST models fail to predict the flow around the cylinder. Errors in the flowfield, particularly for what concerns the $\nu_t$ distributions have been found: this leads to large variations with respect to the experiments and for the hybrid RANS-LES methods, the blending function is even incorrectly activated. Most of the flowfield is solved by means of a RAS and just about the 12% of the flow is solved by LES, this can be due to wrong eddy viscosity values from which the switch from RAS to LES is dependent. The Spalart–Allmaras model resulted to be more in agreement with the evolution of the pressure distributions along the cylinder both for RANS and DES, particularly for the latter smaller errors have been found in terms of drag coefficients and separation angles. Improvements of this work could be to test other turbulence models, for instance SBES as Ekman did for the DrivAer[5], and compare the results with those presented in this thesis.

Passing to the DrivAer's simulations, the first challenge has been to create an appropriate mesh: although the geometry was simplified for computational limits, so different from the one used by Hupertz et al.[2] for the suspensions, engine bay and detailed underbody, it was interesting to set three different meshes for a real and more complex geometry. The results of the simulations for both $DDES_{SA}$ and $IDDES_{SA}$ are in agreement with the test: $DDES_{SA}$ is closer to the experimental values at least in terms of drag, whilst $IDDES_{SA}$ overestimates them a little bit. Lift has been a quantity much more sensitive to the meshes and time step changes and this goes in agreement to what found during the CFD workshop[3] where large differences were found especially in the front wheelhouse where turbulence modeling most of the time fails in simulating the flow. The results have been tested to be grid-independent also in terms of pressure distributions at two different planes placed in the wake of the car and of the wheel. The main differences between $DDES_{SA}$ and $IDDES_{SA}$ are detected in the flow separation: $IDDES_{SA}$ prematurely separates on the C-pillar, as well as on the mirrors and wheels. This behaviour is further

confirmed by the skin-friction distribution which has a large zone of negative values on the back of the car. Possible future works could be to delay this behaviour by increasing the $C_{dt1}$ model constant. Furthermore, it could be interesting to test also here other turbulence models to compare the results with: for instance it would result useful to run preliminary RAS to have better guesses for model initializations.

The sensitivity analysis performed on the Courant number allowed to understand that a greater time step could be used for this simulation and going too much over the CFL condition would result in having stability and convergence problems. Possible improvements for future works could be to increase the number of correctors and outer correctors as the time steps increases to avoid eventually numerical problems and to lower down the order of magnitudes of pressure and velocity residuals.

# Bibliography


[1] Thomas Schuetz. *Aerodynamics of Road Vehicles, Fifth Edition*. SAE International, 2016.

[2] Lothar Krueger Kevin Howard Burkhard Hupertz Karel Chalupa and Hans-Dieter Glueck. In: (2021).

[3] abkahraman CFD online. *AutoCFD2 - Case 2 Results Overview*. URL: `https://autocfd.eng.ox.ac.uk/`.

[4] Neil Ashton and Alistair Revell. In: (2015).

[5] Petter Ekman. "Accuracy and Speed for Scale-Resolving Simulations of the DrivAer Reference Model". In: *WCX SAE World Congress Experience* ().

[6] A. Saddington R. Knowles and K. Knowles. "On the Near Wake of Rotating, 40%-Scale Champ Car Wheels". In: *Proceedings of the 2002 SAE Motorsports Engineering Conference and Exhibition* (2002), pp. 3–4.

[7] A. Cogotti. "Aerodynamic Characteristics of Car Wheels." In: *Intl J. of Vehicle Design, Technological Advances in Vehicle Design Series, SP3, Impact of Aerodynamics on Vehicle Design* (1982), pp. 173–196.

[8] H. Berneburg E. Merker. "On the Simulation of Road Driving of a Passenger Car in a Wind Tunnel Using a Moving Belt and Rotating Wheels." In: *Int. Conf. Innovation and Reliability, Florence* (1992), pp. 8–10.

[9] Hornung H. Perry A.E. "Some Aspects of Three-Dimensional Separation, Part II: Vortex Skeletons." In: *Zeitschrift für Flugwissenschaften und Weltraumforschung* (1984).

[10] Lajos Regert. "Description of flow field in the wheelhouses of cars." In: *International Journal of Heat and Fluid Flow 28 (2007) 616–629* (2007).

[11] S. Deck P. Spalart. "A new version of detached-eddy simulation, resistant to ambiguous grid densities". In: *BG Teubner Stuttgart* (1972).

[12] S. Rezaeiravesh et al. T. Mukha. *A Library for Wall-Modelled Large-Eddy Simulation Based on OpenFOAM Technology*. URL: `https://arxiv.org/abs/1807.11786`.

[13] abkahraman CFD online. *the difference between DES and WMLES?* URL: https://www.cfd-online.com/Forums/main/90494-difference-between-des-wmles.html.

[14] Gritskevich et al. Mikhail S. "Development of DDES and IDDES Formulations for the k- Shear Stress Transport Model". In: *Springer Science+Business Media B.V* (2011).

[15] W. Liou et al. T. Shih. "A New $\kappa$-$\epsilon$ Eddy Viscosity Model for High Reynolds Number Turbulent Flows - Model Development and Validation". In: *Computers and Fluids* (1994).

[16] CFD Online. *SST k-omega model.* URL: https://www.cfd-online.com/Wiki/SST_k-omega_model.

[17] Y. Egorov F. Menter. "The Scale-Adaptive Simulation Method for Unsteady Turbulent Flow Predictions. Part 1: Theory and Model Description." In: *Springer Science+Business Media B.V.* (2010).

[18] CINECA. *GALILEO100.* URL: https://www.hpc.cineca.it/hardware/galileo100.

[19] G. N. Malcolm W. D. James S. W. Paris. "Study of viscous cross flow effects on circular cylinders at high Reynolds numbers". In: (1980).

[20] *Flow regimes of the cyliner at various Reynolds number.* URL: http://www.wolfdynamics.com/wiki/tut_2D_cylinder.pdf.

[21] D. J. Tritton. *Physical Fluid Dynamics, 2nd ed.* Oxford University Press, 1988.

[22] Achenbach. "Distribution of local pressure and skin friction around a circular cylinder in cross-flow up to Re = $5 \cdot 10^6$". In: (1968).

[23] Gunter Schewe. "On the force fluctuations acting on a circular cylinder in crossflow from subcritical up to transcritical Reynolds numbers". In: (1983).

[24] Hermann Schlichting. "Boundary-Layer Theory". In: (1979).

[25] *y+ calculator.* URL: https://www.pointwise.com/yplus/index.html.

[26] Stefan Müller Christoph Strangfeld Christian Nayeri Dirk Wieser Hanns-Joachim Schmidt and Christian Paschereit. In: (2014).

[27] Fazle Hussain Jinhee Jeong. "On the identification of a vortex". In: *J. Fluid Mech.* (1994).

# Ringraziamenti

Innanzitutto, ci tenevo a ringraziare il mio relatore, il Professore Paolo Schito e il mio correlatore, Francesco Fabio Semeraro, per avermi accompagnato durante questo progetto. E' stato il percorso più formativo ed interessante che abbia mai fatto e Vi ringrazio per tutte le conoscenze teoriche e tecniche che mi avete trasmesso.

Ringrazio la mia famiglia che mi ha supportato durante tutto il percorso universitario, in particolare, ringrazio i miei fratelli, Ilaria e Daniele, due pilastri fondamentali della mia vita.

Ad Ilaria, una delle poche persone ad avermi fisicamente e psicologicamente aiutato durante i momenti più duri: grazie per tutte le volte che mi hai detto di venire a Torino quando sapevi che non stavo bene, per tutte le volte che mi dicevi di venire a mangiare da te che avevi fatto anche il dolce, per le volte che dormivo da te e mi facevi trovare il cornetto pronto la mattina e per tutte le altre volte in cui mi hai dimostrato di preoccuparti per me. Sei un pezzo fondamentale della mia vita e il tempo potrà solamente rafforzare il legame già forte che c'è tra di noi.

A Daniele, o meglio Danuccio, il fratello più piccolo che mi ha dimostrato una maturità e una sensibilità che va ben oltre la sua età. L'ironia con cui prendi la vita, mi ha aiutato in tanti momenti ed è sempre stato un motivo per alleggerire i periodi più complessi. Spero di essere per te sempre un supporto costante, come tu lo sei per me.

Ai miei genitori, che anche nei momenti in cui avevo perso le speranze, mi avete dato prova che credevate comunque in me, anche se non me l'avete mai detto!

A Luigi, ormai un fratello maggiore che insieme ad Ilaria mi hanno supportato sempre. La felicità che porti quando stiamo insieme è incommensurabile. Ne abbiamo passate tante e saranno tanti altri i momenti di condivisione e felicità che ci aspettano.

A Francesco ed, insieme a lui, un ringraziamento particolare e molto sentito ai suoi Genitori. Il mio percorso non avrebbe avuto questo epilogo senza di voi. Ogni parola sarebbe riduttiva per esprimere quanto ve ne sono grato. Non vi ringrazierò mai abbastanza per quello che avete fatto.

A Zia Antonella, una tra le persone più sincere che io conosca. Sei stata l'unica che ha avuto sempre il pensiero di venirmi a salutare anche solo dal balcone e farmi fare due risate. Questi sono i piccoli gesti che contano di più nella vita.

A Mattia, che mi ha fatto appassionare al mondo della Formula 1. Probabilmente non starei qui a parlare di Aerodinamica, se tu non mi avessi trasmesso così tanto!

A Rosario, Marta, Francesco, Carmen e Roberto, gli amici di una vita. Anche se le strade un giorno si divideranno, credo che l'amicizia che ci lega non finirà mai e ci sarà sempre l'occasione di rivederci, magari davanti ad un risotto cucinato da una Chef di fiducia.

A Domenico, per le pizze a mare su una panchina e per quelle teglie di pizza che non ci siamo mai riusciti a finire in due, per tutti i tornei non vinti e tanti altri momenti che saranno sempre un modo per ridere e abbuffarci insieme.

Al Big Bang, una tra le cose più belle a cui abbia mai aderito. Ormai sono passati 10 anni, mi vengono i brividi solo a pensarci. La forza di gruppo è una caratteristica che ci contraddistingue e che mi ha accompagnato per gran parte della mia vita. Tante sono le sfide che ancora ci aspettano!

A tutti i colleghi che ho conosciuto durante questi 6 anni, in particolare Pedro, Elisa e Philipp, un trio fantastico che mi ha fatto affrontare la vita universitaria con la giusta dose di spensieratezza, nonché per il supporto accademico e psicologico durante le sessioni più difficili. Ci sono ancora delle promesse da saldare!

Infine grazie a tutti gli amici e i parenti che hanno supportato le mie scelte dall'inizio alla fine. Ognuno nel suo piccolo è stato di fondamentale aiuto per il conseguimento di questo obiettivo.

Sono passati più di 6 anni dal mio primo trasferimento a Milano e oggi mi trovo qui a festeggiare l'ultimo tassello di questo percorso universitario. Non ci credo ancora. Se ripenso a tutte le difficoltà di questi anni, non mi capacito di come io sia arrivato fino a qui.

A tutti i trasferimenti affrontati da solo: ricordo ancora quando da Torino dovevo trasferirmi nella mia ultima casa a Milano e sono partito con due valige enormi e appena sceso dal tram ha iniziato a diluviare fortissimo e mi sono bagnato tutto fino ad arrivare a casa. In quel momento (e in tanti altri) ho pensato, "Perchè il destino mi va sempre contro?".

A quando agli esami pensavo se fossi riuscito o meno ad arrivare alla fine del mese. Quante volte. Troppe volte.

Ai momenti in cui la mia testa non voleva collaborare.

A tutte le persone che mi hanno ostacolato, mi chiedo cosa dovrei dirvi ora? Grazie perchè senza di voi non sarei qui? No, piuttosto mi chiedo, ora che non mi avete fermato, a cosa vi ha portato quello che avete fatto? Forse non c'è una risposta a tutte le domande e forse è meglio così.
Tante volte mi sono chiesto perché certe cose succedono e perché proprio a me. Poi ho capito che ci saranno sempre queste difficoltà in forma più o meno ridotta. In queste situazioni decidi se fermarti o correre più forte di prima. Decidi se continuare a lamentarti o ritrovare la strada. Ho capito cosa contava realmente. Aldilà di tutto questo dolore, effettivamente ci sono gioie per cui ne vale la pena andare avanti. Mi sono alzato le maniche e mi sono letteralmente spaccato i gomiti per raggiungere il mio obiettivo.
Una persona saggia mi disse una volta: "Mò si fa sul serio, la torta si cucina negli ultimi minuti". Questo sarà un motto che mi accompagnerà sempre. Non mi accontenterò mai finchè non avrò dato tutto quello che è nelle mie corde, fino alla fine.

Ringrazio me stesso per tutte le fatiche, i sacrifici, i dolori, le ansie, le lacrime, infine le gioie e le vittorie raggiunte.
Un piccolo, personale ed importante traguardo.
Che questo possa essere l'inizio di qualcosa di più grande.

*Per aspera ad astra.*

*22/07/2022,*
*Giovanni Renda, Dottore Magistrale in Ingegneria Aeronautica.*